



MEMS BASED DOPPLER VELOCITY MEASUREMENT SYSTEM

A dissertation submitted by

Minchul Shin

IN PARTIAL FULFILLMENT OF THE REQUIREMENTS FOR THE DEGREE
OF DOCTOR OF PHILOSOPHY IN MECHANICAL ENGINEERING

TUFTS UNIVERSITY
MEDFORD, MA 02155

AUGUST, 2012

Advisor: Robert D. White, Ph.D.

©2012 Minchul Shin
All Rights Reserved

Abstract

The design, fabrication, modeling and characterization of a capacitive micromachined ultrasonic transducer (cMUT) based in-air Doppler velocity measurement system using a 1 cm^2 planar array are described. Continuous wave operation in a narrowband was chosen in order to maximize range, as it allows for better rejection of broadband noise. The sensor array has a 160-185 kHz resonant frequency to achieve a 10 degree beamwidth. A model for the cMUT and the acoustic system which includes electrical, mechanical, and acoustic components is provided. Furthermore, characterization of the cMUT sensor with a variety of testing procedures is provided. Laser Doppler vibrometry (LDV), beampattern, reflection, and velocity testing characterize the performance of the sensors. The sensor is capable of measuring the velocity of a moving specular reflector with a resolution of 5 cm/s, an update rate of 0.016 second, and a range of 1.5 m.

Acknowledgement

I am sincerely thankful for the advice, support, and general understanding I received from Dr. Robert White. I would also like to thank the members of my committee, Dr. Jason Rife, Dr. Jeff Hopwood, Dr. Paul DeBitetto, and Peter Sherman for their combined efforts to help me complete this research. These people guided me through territory which was initially unfamiliar to me. They were primarily responsible for making this work a most enriching educational experience.

I would also like to thank my friends, Joshua Krause, Susan Liu, Zhengxin Zhao, Christopher Doody, Cinzia Metallo, Sam McNaughton, Eon-Seok Gil, and Choongbae Park, for all of their words of encouragement and advice as well as their companionship.

I also thank my family for all of their support and generosity over the last four years. Without their overall understanding, my dream of going to graduate school in Mechanical Engineering could not have been achieved. Finally, I would like to thank my families: Sun Jung Lee, Yerin, and Yejune for all their support, understanding, and patience while I was completing my degree.

Contents

| | | |
|----------|--|-----------|
| 1 | Introduction | 1 |
| | 1.1 Motivation..... | 1 |
| | 1.2 Contribution..... | 3 |
| 2 | Background..... | 5 |
| | 2.1 Ultrasound..... | 5 |
| | 2.1.1 Acoustic Rangefinder for Robotics..... | 8 |
| | 2.2 Doppler Effect..... | 10 |
| | 2.2.1 Applications..... | 12 |
| | 2.3 Capacitive Micromachined Ultrasonic Transducer (cMUT)..... | 12 |
| | 2.3.1 Physical Principle and History..... | 12 |
| | 2.3.2 Advantages..... | 14 |
| | 2.3.3 Recent Developments of cMUTs..... | 14 |
| | 2.3.3.1 FEM Simulations..... | 14 |
| | 2.3.3.2 Equivalent Circuit Modeling..... | 18 |
| | 2.3.3.3 Experimental Investigation..... | 22 |
| | 2.4 MEMS-Based Rangefinder..... | 27 |
| 3 | Design..... | 32 |
| | 3.1 PolyMUMPs® chip..... | 32 |

| | | |
|----------|--|------------|
| 3.1.1 | Structure..... | 32 |
| 3.1.2 | Fabrication..... | 33 |
| 3.2 | Nickel-on-glass chip..... | 38 |
| 3.2.1 | Structure..... | 38 |
| 3.2.2 | Fabrication..... | 40 |
| 4 | Modeling and Electronics Design..... | 47 |
| 4.1 | Sensor Design..... | 47 |
| 4.1.1 | Lumped Element Modeling (LEM)..... | 47 |
| 4.2 | Electronics Design..... | 60 |
| 4.2.1 | Receiver Electronics with PolyMUMPs® Chip..... | 60 |
| 4.2.2 | Transmitter Electronics with Nickel-on-glass Chip..... | 65 |
| 4.2.3 | Receiver Electronics with Nickel-on-glass Chip..... | 67 |
| 5 | Experimental Result..... | 72 |
| 5.1 | PolyMUMPs® Chip..... | 72 |
| 5.2 | Nickel-on-glass Chip..... | 86 |
| 6 | Conclusion and Future Work..... | 100 |
| 6.1 | Conclusion..... | 100 |
| 6.2 | Future Work..... | 104 |
| A | Fabrication Runsheet of Nickel-on-glass Chip..... | 104 |
| B | MATLAB® Script..... | 108 |
| B.1 | Modeling of Single Transducer of Nickel-on-glass Chip..... | 108 |
| B.2 | Beampattern Modeling of Sensor Arrays in Nickel-on-glass Chip..... | 114 |
| B.3 | Noise Model of the Electronics of Nickel-on-glass Chip..... | 119 |

| | | |
|----------|---|------------|
| | B.4 Snapdown Modeling of Single Transducer of Nickel-on-glass Chip..... | 121 |
| | B.5 Spetrum Analysis with Velocity Data..... | 123 |
| C | CAD Drawings..... | 126 |
| | C.1 PolyMUMPs® Chip..... | 126 |
| | C.2 Nickel-on-glass Chip..... | 129 |
| | C.3 Shadow Mask Design..... | 130 |

List of Figures

| | |
|---|----|
| Figure 1: Frequency (wavelength in air) range of ultrasound | 5 |
| Figure 2: Flow measurement by ultrasound [30]. | 6 |
| Figure 3: The IVUS images of blood flow in the rabbit's aorta (a) in stent and (b) out of stent [31] | 7 |
| Figure 4: Schematic of the therapeutic ultrasound for a deep skin [32]. | 8 |
| Figure 5: Devantech® SRF 04 system [34] | 9 |
| Figure 6: Change of frequency by a moving source..... | 11 |
| Figure 7: Schematic of cMUT..... | 13 |
| Figure 8: LDV measurement and FEM simulation for membrane displacement [18]. | 15 |
| Figure 9: (a) A model geometry and (b) bandwidth result [40] | 16 |
| Figure 10: Effect of electrode on (a) inner radius and (b) outer radius. | 17 |
| Figure 11: (a) Comparison between the conventional mode operation and (b) the collapse mode of operation [42]...... | 17 |
| Figure 12: (a) Lumped element model, and (b) the comparison between experiment and simulation in air [28] | 19 |
| Figure 13: (a) Equivalent model, and (b) electrical impedance of air cMUT [43]..... | 19 |
| Figure 14: (a) Lumped element model, and (b) comparison between experiment and simulation [44] ... | 20 |
| Figure 15: (a) cMUT sensor, (b) comparison between experiment and simulation, and (c) lumped element model [17]..... | 21 |
| Figure 16: (a) An AFM view of a single membrane structure and (b) bandwidth of a cMUT element in water [16]..... | 22 |
| Figure 17: (a) cMUTs with analogue electronics and (b) CMOS-ASIC implementation of 16 charge amplifier array [46] | 23 |

| | |
|--|----|
| Figure 18: (a) cMUT array and (b) 2D image of brass rod and fishing line [29]..... | 24 |
| Figure 19: (a) cMUT array with flexible circuit and (b) in-vivo images of the carotid artery and thyroid gland by PZT array and cMUT [47]. | 25 |
| Figure 20: (a) IC and (b) 2D image of nylon wire phantom [48]..... | 26 |
| Figure 21: (a) cMUT device, (b) experimental set-up, (c) 3D photoacoustic (hot-metal color scale) image overlaid on a pulse-echo image (gray-scale) of fishing line, and (d) chicken breast [49] | 27 |
| Figure 22: MEMS-based range finder. (a) Package with CMOS and transducer, and (b) range test result [50]. | 28 |
| Figure 23: (a) pMUT-based range finder with distance > 1 m, and (b) Signal-to-Noise ratio vs distance [51]. | 29 |
| Figure 24: (a) pMUT array with transmitters and receivers, and (b) the result of the angle measurement [10]. | 30 |
| Figure 25: (a) Sensor array, and (b) the result of the distance measurement [52]..... | 30 |
| Figure 26: Schematic of a single element (top view). | 33 |
| Figure 27: Schematic illustrates the fabrication process using the MEMSCAP PolyMUMPs® process... | 34 |
| Figure 28: Schematic of one element in the cMUT sensor array showing the cross-sectional diagram after Au deposition. | 37 |
| Figure 29: Photograph of a single element (left) and the cMUT arrays in an 8×8 pattern (right)..... | 37 |
| Figure 30: Schematic of a single element (top view). | 39 |
| Figure 31: The fabrication process using the nickel plating and the copper plating. | 40 |
| Figure 32: Cr/Au interconnect and bottom electrodes after the liftoff. | 41 |
| Figure 33: Copper sacrificial layer and Cr/Au interconnection after the copper plating. | 41 |
| Figure 34: Nickel structure layer with vent holes after the nickel plating. | 42 |
| Figure 35: Nickel structure after the release with the acetic acid, hydrogen peroxide, and water etch. | 43 |
| Figure 36: Photograph of nickel cMUT array after packaging (left) and the cMUT arrays in zoom-in (right). | 43 |
| Figure 37: SEM of the nickel cMUT array after the release. | 44 |
| Figure 38: SEM of a vent hole after the release. | 44 |
| Figure 39: single degree of freedom (single mode) simplification of the diaphragm behavior using LEM48 | |

| | |
|--|----|
| Figure 40: Coupled mechanical-electrical lumped element model. | 50 |
| Figure 41: Comparison of finite-element and analytical approximation to the environmental loading presented in nondimensional form. | 51 |
| Figure 42: A simplified sensor model and electronics model of the receiver. | 61 |
| Figure 43: Comparison between impedance model and experimental result. (a-b) PolyMUMPs® results and (c-d) nickel-on-glass chips. | 62 |
| Figure 44: The receiver electronics including a voltage reference, a charge amplifier and voltage amplifiers. | 63 |
| Figure 45: Transfer function of the receiver electronics from experiment. | 65 |
| Figure 46: Predicted snapdown voltage comparison between (a) the PolyMUMPs® chip and (b) the nickel-on-glass chip. | 66 |
| Figure 47: Bridge circuit with the cMUT chip. Modified from [62] | 67 |
| Figure 48: A simplified sensor model and electronics model of the receiver. | 67 |
| Figure 49: The receiver electronics for the nickel-on-glass chip. | 69 |
| Figure 50: Predicted noise density of the receiver electronics with the nickel-on-glass chip. | 70 |
| Figure 51: Comparison of noise density between the noise model and the experiment | 71 |
| Figure 52: Experimental set-up with LDV and the chip. | 73 |
| Figure 53: Automatic frequency sweep scanning using a LabVIEW program. | 74 |
| Figure 54: Experimental set-up diagram with LDV and the chip. | 74 |
| Figure 55: Frequency sweep scanning result for all 64 elements. | 75 |
| Figure 56: Predicted center point motion frequency response for a single element and the experimental result. | 76 |
| Figure 57: Acoustic transmit test set-up using cMUT Array (80 kHz). | 77 |
| Figure 58: Acoustic transmit test result with beampattern. Beampattern is in units of dBSPL. | 78 |
| Figure 59: Acoustic transmit & receive test set-up using cMUT Array (185 kHz). | 79 |
| Figure 60: Beampattern of acoustic transmit & receive test with cMUT array. | 80 |
| Figure 61: Reflection test set-up using cMUT array. | 81 |
| Figure 62: The change of the dynamic signal when D increases. (a) D=10.2 cm, (b) D=30.5 cm | 81 |

| | |
|--|-----|
| Figure 63: Range test result. The sensor signal is in dBV_{rms} in a 0.24 Hz band (4.2 second averaging time). | 82 |
| Figure 64: Experimental set-up for the velocity test. | 83 |
| Figure 65: Schematic of a set-up for the velocity test. | 84 |
| Figure 66: Spectrogram after the velocity test and an experimental concept. | 85 |
| Figure 67: Spectrograms of the shifted frequency during different velocity tests. | 86 |
| Figure 68: Predicted voltage-capacitance model and the experimental result. | 87 |
| Figure 69: Automatic frequency sweep scanning using a LabVIEW program. | 88 |
| Figure 70: Frequency sweep scanning result for all 168 elements. (a) The odd row and (b) the even row. | 89 |
| Figure 71: Predicted center point motion frequency response for a single element and the experimental result. | 90 |
| Figure 72: Acoustic transmit & receive test using cMUT Array (180 kHz) and beampattern. | 91 |
| Figure 73: cMUT mounting package shielded with EMI protection. | 92 |
| Figure 74: Schematic of range test set-up using cMUT array. | 93 |
| Figure 75: Range test set-up using cMUT array. | 94 |
| Figure 76: Range test result using cMUT array with three reflection materials such as aluminum, plywood, and acrylic. | 94 |
| Figure 77: Schematic of a set-up for velocity test. | 95 |
| Figure 78: A set-up for velocity test. | 95 |
| Figure 79: Spectrograms of the sled velocity moving toward the sensor at 0.4 m/s. | 96 |
| Figure 80: Spectrogram of the sled velocity moving toward the sensor at 0.6 m/s. | 97 |
| Figure 81: Spectrogram of the sled velocity moving toward the sensors at 0.1 m/s. | 98 |
| Figure 82: Spectrograms of the sled velocity moving away from the sensors at 0.3 m/s. | 99 |
| Figure 83: Design masks for the whole array of PolyMUMPs® chip. | 127 |
| Figure 84: Design masks for a single transducer of PolyMUMPs® chip. | 128 |
| Figure 85: Design masks for the whole array of nickel-on-glass chip. | 129 |

| | |
|--|-----|
| Figure 86: Design masks for a single transducer of nickel-on-glass chip..... | 129 |
| Figure 87: Shadow mask design for PolyMUMPs® chip..... | 130 |

List of Tables

| | |
|---|-----|
| Table 1: Comparison between this work and other ultrasonic range finders. | 10 |
| Table 2: Comparison between this work and other MEMS-based rangefinders. | 31 |
| Table 3: Geometric properties of the PolyMUMPs® cMUT sensor | 36 |
| Table 4: Material properties of a diaphragm..... | 36 |
| Table 5: Geometric properties of the nickel-on-glass cMUT sensor | 45 |
| Table 6: Material properties of a diaphragm..... | 45 |
| Table 7: Conjugate power variables in Mechanical and Acoustical Domain. | 48 |
| Table 8: Lumped elements in mechanical and acoustical domain. | 49 |
| Table 9: Relationship between conjugate power variables in each domain..... | 49 |
| Table 10: Relationship between geometric properties and device performances | 60 |
| Table 11: Electronics component of the PolyMUMPs® chip..... | 64 |
| Table 12: Electronics component of the nickel-on-glass chip. | 68 |
| Table 13: Performance comparison between a PolyMUMPs® chip and a nickel-on-glass chip. | 102 |

Chapter 1

Introduction

The goal of this dissertation is to produce and demonstrate a 1 cm \times 1 cm acoustic Doppler velocity measurement system building off of existing MEMS capacitive micromachined ultrasound transducer (cMUT) array technology. This chapter shows motivations of the sensor development and contributions.

1.1 Motivation

Rangefinders are used in a variety of applications, such as mobile robot positioning, personal navigation systems, micro air vehicle navigation, obstacle detection, and map building [1-6]. A number of approaches exist.

Among suitable techniques, RADAR-based Doppler velocity or distance measurement systems in the 10 GHz to 100 GHz band are often used. These systems have RF wavelengths on the order of 3-30 millimeters, slightly longer than the 1.5 mm acoustic wavelength of the 180 kHz ultrasonic system described here. RADAR systems include continuous wave (CW) systems for velocity measurement, and frequency modulated (FM/CW) systems for distance measurement. However, RADAR based systems require high power consumption. In addition, RADAR systems at 10 GHz must have an array 10 times the size of the acoustic array described

here in order to achieve the same beamwidth. Operating at 10 – 100 GHz presents a different set of signal processing challenges.

In addition to the RADAR based system, laser rangefinders are also used in navigation applications. Laser rangefinders can detect the range of a target accurately over a long range and can provide high angular resolution, but have disadvantages: high cost, high power consumption, and low sensitivity to ambient illumination [7, 8]. Another approach in map building for mobile robots is infrared rangefinder sensors. These devices can provide advantages including low-cost and low power consumption. However, the infrared rangefinder has problems including nonlinearity and random errors during the data read [8, 9]. On the other hand, ultrasonic sensors have advantages: their low cost, small size, low power consumption, and simple signal processing [10]. Various ultrasonic measurement systems are available commercially. However, a portable commercial acoustic Doppler system for velocity measurement in air is not reported commercially or in the academic literature. Furthermore, the majority of commercial acoustic Doppler velocity systems are targeted at flow measurement applications rather than velocity-for-navigation applications.

By using a MEMS based transducer system (pMUT or cMUT), the size and cost of the system can be reduced. However, in the fabrication of the pMUTs, deposition of high quality piezoelectric thin films with well controlled properties is challenging. Significant effort and cost is associated with producing high quality piezoelectric films. The cMUTs do not require any complex material deposition steps.

This dissertation outlines the methods for creating a solution to a smaller, potentially cheaper, and low power MEMS ultrasonic array for the velocity measurement in air using cMUT technology.

1.2 Contribution

As a first contribution, this research work represents the first description in the literature of cMUT based in air Doppler ultrasound. A novel cMUT transducer chip, the associated electronics, and a full system in operation are completely demonstrated for the first time and their capabilities explored. Limited work has been done on MEMS transducer systems for in-air acoustic ranging and Doppler velocity measurement. In 2011, Przybyla, *et al.* described a MEMS based piezoelectric acoustic rangefinder in air. This work differs significantly from the current work in that a thin film aluminum nitride membrane was employed in a pulse-echo ranging configuration [11]. Aluminum nitride thin films can be difficult to deposit with high quality. In the current work, a capacitive micromachined ultrasound transducer (cMUT) array is used in a continuous wave mode for velocity measurement. The array described here has some similarities to other cMUT devices, which were first described by Haller and Khuri-Yakub in 1994 [12-14], and have since been developed by a number of authors [15-19]. However, the majority of cMUT work has been directed toward biomedical ultrasound or submerged ultrasound.

Furthermore, this research work contributes to cMUT modeling using the lumped element model (LEM) [17] of a single element transducer. Many investigators used LEM for an explanation of the behavior of the device. However, their LEM does not include an

environmental loading model, diaphragm mechanics, and electromechanical coupling specifically. First of all, in the LEM, the environmental mass loading can be explained using the acoustic radiation impedance of the pulsating membrane radiating into an infinite half-space. An approximate approach for the radiation impedance of an axisymmetric bending plate is provided. With the environmental loading model, the current LEM can be used over a wider frequency range than the previous LEMs. Furthermore, the diaphragm mechanics including the effective mass and the stiffness are shown. This allows for efficient computation of complex cross-sectional geometries [17]. This approach can be also used for biomedical cMUT modeling [16].

A third contribution is the development of a 3 layer nickel-on-glass MEMS fabrication process. This process has many similarities to LIGA and LIGA-like processing [20-23] but is considerably simpler to implement. The process is an important addition to the capabilities of the Tufts fab, and is expected to provide a baseline fabrication process for the production of a range of low stray capacitance sensors. The process has since been applied to other sensor designs including shear sensors and microphone arrays.

A final contribution is the experimental characterizations including laser Doppler velocimetry (LDV), beampattern measurement with model prediction, range testing, and velocity testing using Doppler shift with in-air Doppler ultrasound. The LDV measurement and beampattern measurement validate the effective LEM, comparing experimental data with prediction. In addition, the range test and the velocity test show the performance of the devices.

Chapter 2

Background

This chapter discusses the background for the cMUT rangefinder, specifically ultrasound, Doppler effect, cMUT fundamentals, and other rangefinders. Literature reviews show advantages of the device and disadvantages comparing other devices with the current device.

2.1. Ultrasound

Ultrasound is defined as a sound pressure wave with a frequency greater than the upper limit of human hearing (20 kHz). Frequency (wavelength in air) range of the ultrasound is defined in Figure 1.

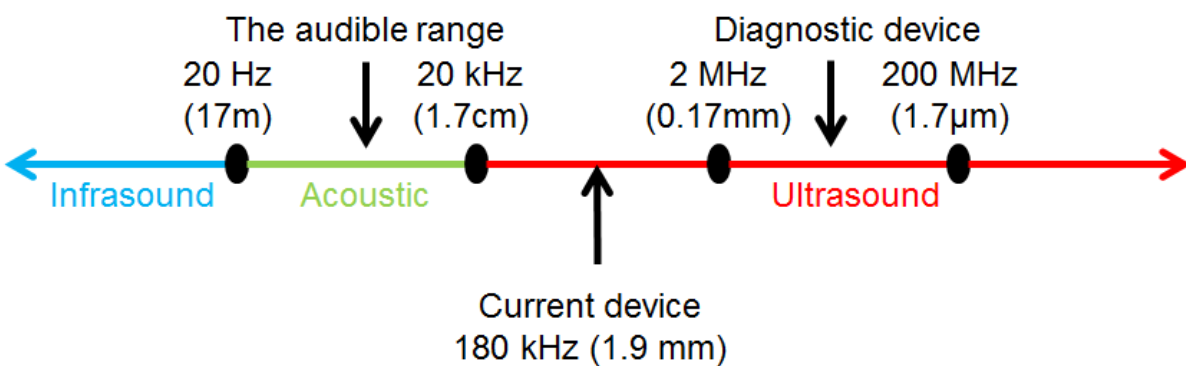


Figure 1: Frequency (wavelength in air) range of ultrasound

In a variety of fields, ultrasound is very useful. Among those applications, ultrasound is used for detection of an inner material. Ultrasound penetrates a medium and measures the reflection from a target. Each target's material properties and medium structure provide different reflection information. A commonly known application is to generate images of fetuses in the human womb. Furthermore, intravascular ultrasound (IVUS) can be performed with angiography in order to more precisely measure the degree of stenosis and provide the velocity of a blood flow. A variety of medical diagnostic ultrasound technologies exist for imaging various parts of the anatomy. All commercial medical diagnostic ultrasound uses piezoelectric or piezocomposite transducers, although a number of researchers in recent years have been promoting cMUTs as an alternative technology [17, 24-29].

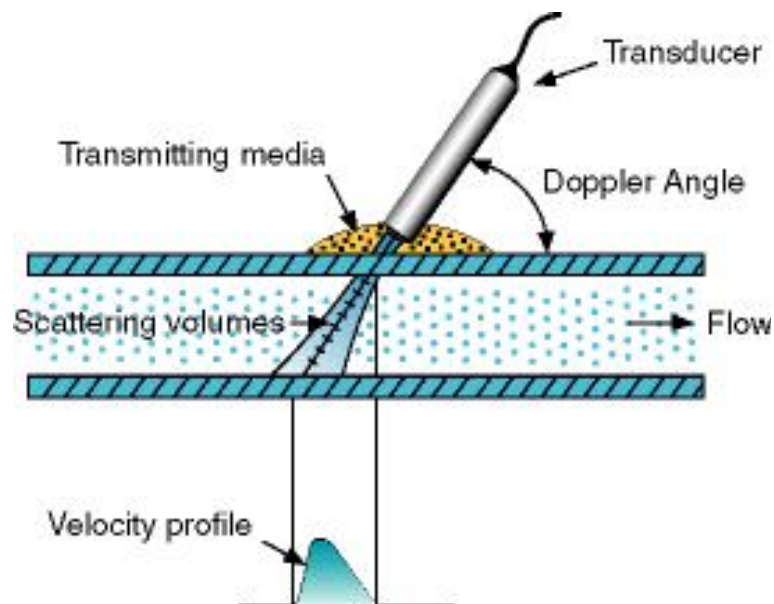


Figure 2: Flow measurement by ultrasound [30].

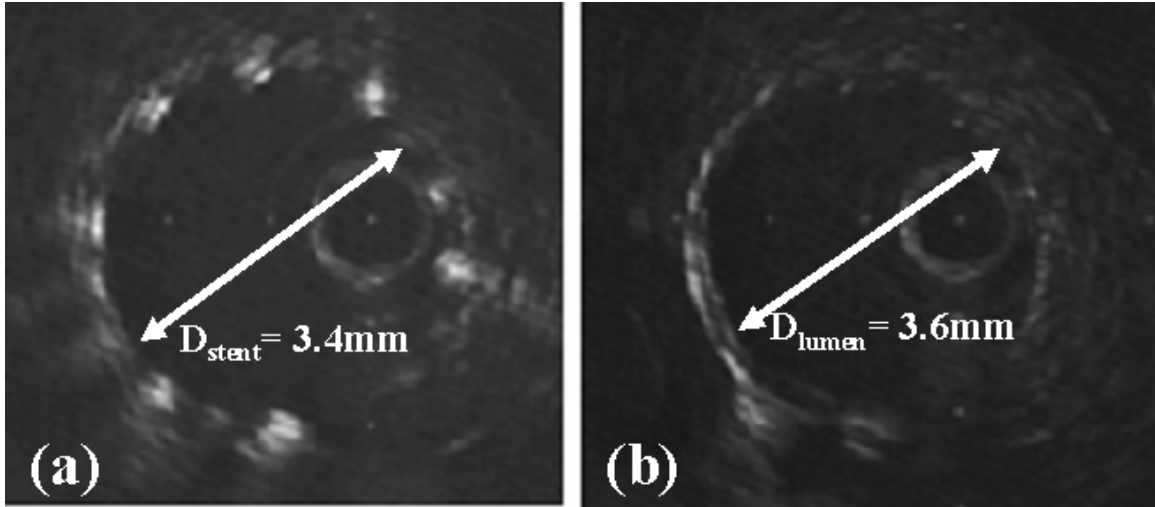


Figure 3: The IVUS images of blood flow in the rabbit's aorta (a) in stent and (b) out of stent [31]

Another application is rangefinding for maritime and naval applications known as SONAR (sound navigation and ranging). SONAR utilizes a time-of-flight (ToF) method. A transmitter sends an ultrasonic wave in the specific medium. The wave moves until it contacts a target. The wave is reflected from the target and reaches the transmitter. The time that the wave travels for, provides the distance between the transmitter and the target.

Ultrasound is used for therapeutic purposes including tissue heating for recovery from tissue injuries during sports, lithotripsy for the destruction of kidney stones, and drug delivery. An unreachable soft tissue, 2-5 cm beneath a skin, is stimulated by the therapeutic ultrasound alternating compression and rarefaction between 0.8 and 2 MHz (Figure 4).

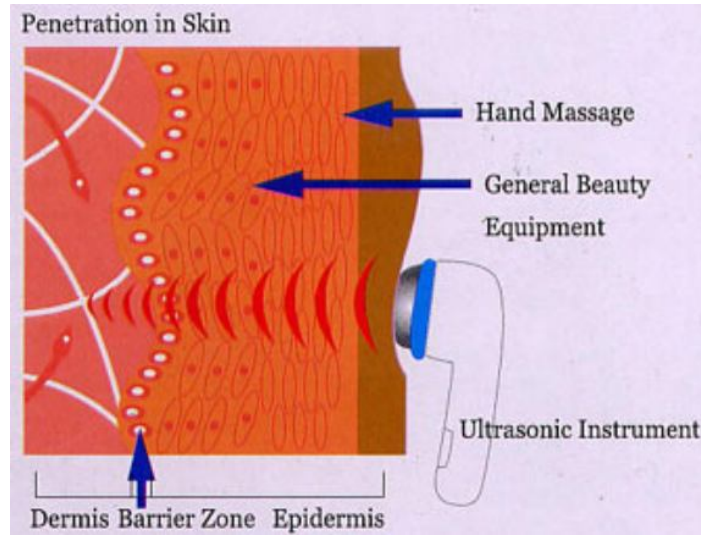


Figure 4: Schematic of the therapeutic ultrasound for a deep skin [32].

Another use is detection of internal flaws in a material and characterization of a material. Analyzing information of a reflected ultrasound wave provides information on imperfection including cracks.

2.1.1 Acoustic Rangefinder for Robotics

Biber *et al.* [33] introduces the Polaroid ranging module using a ToF method. A capacitive transducer with a thin metal membrane as a transreceiver is embedded. The Polaroid system transmits 1-millimeter acoustic wave. Four frequencies (60, 56, 52.5, and 49.41 kHz) are used to increase the probability of signal detection.

Another commercial rangefinder is the SRF series ultrasonic sensor (Devantech, Norfolk, England), which overcomes the bulky size of the Polaroid ranging system (Figure 5). This device (SRF04, size (4.3 cm × 2 cm × 1.7 cm)) uses an echo pulse with short trigger (10 μS). The maximum range of this device is 3 m at 40 kHz.

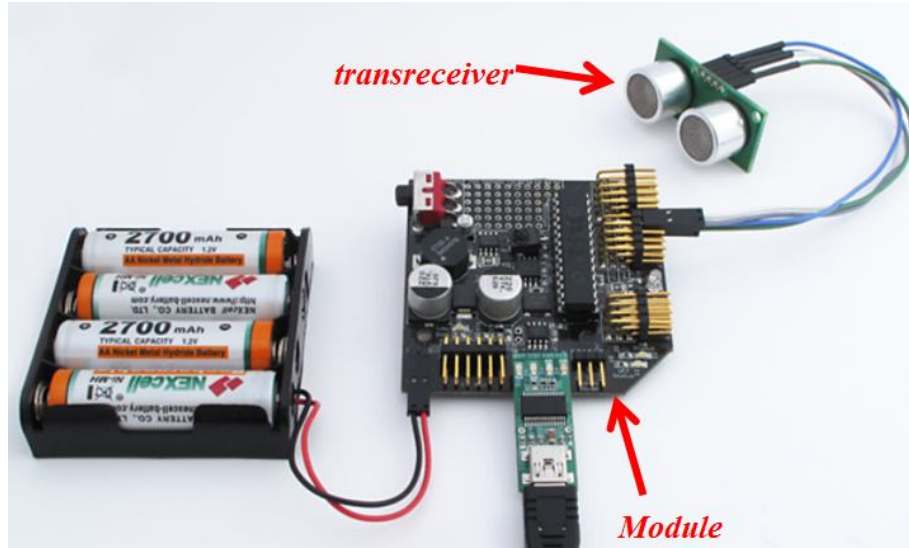


Figure 5: Devantech® SRF 04 system [34]

Webster [35] introduced a pulsed ultrasonic rangefinder using binary-frequency shift-keyed (BFSK) signal as a transmission. The author used phase digitizing for estimation of the time delay. BFSK (37.7 and 40 kHz) was used to increase phase linearity. The device has a maximum range of 5m and an accuracy of 0.02 %.

Note that a major difference between these commercial systems and the current work is the operation frequency. By operating at a much higher frequency, a more directional sensor is realized while maintain a small size. In addition, by operating at higher frequency, larger absolute frequency shifts occur at lower velocities, resulting in a considerable improvement (linear in frequency) for velocity resolution.

| | Frequency (kHz) | Technology | Range (m) | Drive Voltage (V) | Resolution |
|--------------------------|--------------------|---------------|-----------|---------------------------------|------------|
| Biber <i>et al.</i> [33] | 49-60 | Electrostatic | 10m | V_{bias} : 4.7-6.8 | 1% |
| SRF04 [34] | 40 | - | 3m | V_{bias} : 5 | - |
| Webster [35] | 37-40 | Bulk | 5m | - | 0.01 mm |
| This work | 180 | cMUT | 1.5 | V_{pp} : 140, V_{bias} : 10 | 1 cm/s |

Table 1: Comparison between this work and other ultrasonic range finders.

2.2. Doppler Effect

Doppler effect (or Doppler shift), is defined as the phenomena when frequency of a wave changes and an observer moves relative to its source. When the wave travels in a medium, the velocity of the observer and of the source is determined, considering motion of the medium in which waves travel. The Doppler effect can be easily found. When a police car sounding a siren comes toward an observer, the observed frequency is higher than the transmitted. At the instant that the police car passes the observer, the observed frequency is same as the transmitted. When the siren fades away in the distance, the observed frequency is lower than the transmitted one [36].

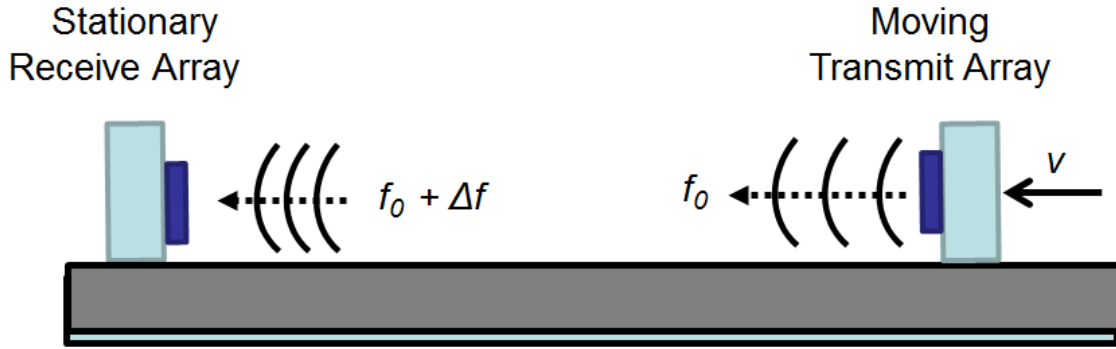


Figure 6: Change of frequency by a moving source

When the velocity of waves (≈ 343 m/s) in the medium is much faster than the velocity of the source and of the receiver relative to the medium, the equation between receiver-observed frequency f and transmitter-emitted frequency f_0 is given by

$$\frac{f - f_0}{f_0} = \frac{v_s}{C} \quad (2.1)$$

Where, v_s is the velocity of the moving target,

C is the speed of sound.

If the source and transmitter both move with respect to a stationary reflector and stationary medium, then

$$\frac{f - f_0}{f_0} = \frac{2v_s}{C} \quad (2.2)$$

2.2.1. Application

The most important application is Doppler RADAR. The Doppler RADAR is used for the measurement of a target velocity using Doppler shift. A microwave is used for the Doppler RADAR and the velocity is determined by analyzing the Doppler shift. Early versions of the Doppler RADAR were continuous wave (CW) and frequency modulated CW (FMCW). Recently, pulse-Doppler RADAR (PD) and Doppler processors for coherent pulse RADARs were developed. The use of both Doppler processing and pulse RADARs detects velocity of a target more accurately [36]. In addition, Doppler effects are present in reflections from moving blood in diagnostic medical ultrasound, and are commonly used to overlay blood velocity information on ultrasound images [31].

2.3 Capacitive Micromachined Ultrasonic Transducers (cMUTs)

2.3.1 Physical principle and history

Recently, capacitive micromachined ultrasonic transducers (cMUTs) were developed as an alternative technology for ultrasonic measurement. A cMUT sensor is an ultrasonic probe using the vibration of numerous film membranes, typically micromachined on a silicon wafer. Capacitive transducers were first developed in the 1950's [37]. With the advent of MEMS technology, this sensor was miniaturized in the early 1990's [38]. Much of the work came from Khuri-Yakub's group at Stanford University.

A cMUT sensor consists of a bottom electrode covered by a thin membrane. There is an air gap between these two films and the capacitor is developed. A voltage is applied between both electrodes and the membrane is pulled down to the bottom electrode by electrostatic forces. The membrane moves until the electrostatic force has equilibrium with internal force of the membrane. AC signals cause vibrations of the thin diaphragm and generate ultrasonic waves. Furthermore, the receiver can detect an ultrasonic wave using the change of capacitance when displacement of the membrane is caused by the pressure of an arriving ultrasonic wave. A simplified schematic of a cMUT is shown in Figure 7.

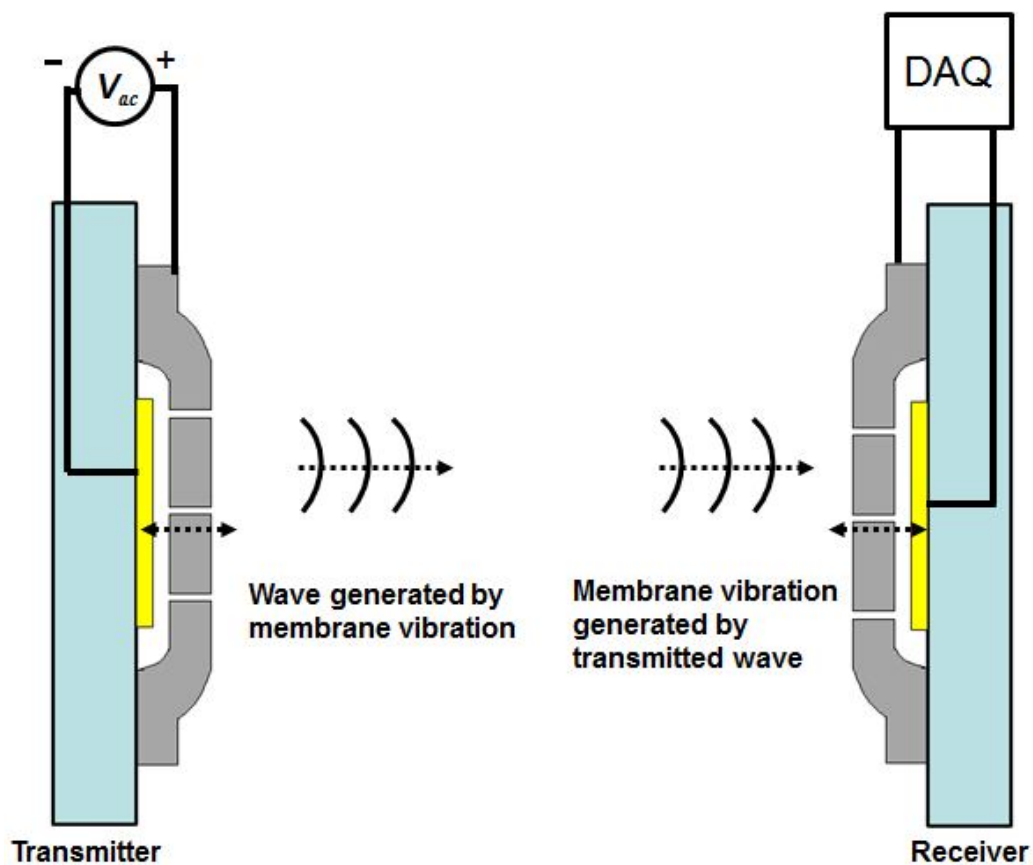


Figure 7: Schematic of cMUT

2.3.2 Advantages

One of main advantages that cMUT has, is that no piezoelectric thin films are used. Deposition of high quality piezoelectric thin films with well controlled properties is challenging. Significant effort and cost is associated with producing high quality piezoelectric films. cMUTs do not require any complex material deposition steps. This may also improve compatibility of the cMUT process with electronics fabricated in a standard CMOS process.

In general, MEMS technologies [either pMUT (piezoelectric micromachined ultrasonic transducer) or cMUT based] are well suited to batch fabrication and integration with electronics, resulting in the potential for low cost sensors in volume production.

2.3.3. Recent Developments of cMUTs

2.3.3.1 FEM simulations

Eccart *et al.* [18] developed transducers embedded into a standard BiCMOS. The thickness of the polysilicon membrane is 400 nm and the oxide sacrificial layer is 600 nm thick. 30 X 30 hexagonal phased arrays were built with CMOS. A DC bias of 21 V and an AC voltage of 1V excited the cMUT sensor in water and oil. They compared an experimental membrane behavior with ANSYS® simulation, providing good match between them. Figure 8 shows their result.

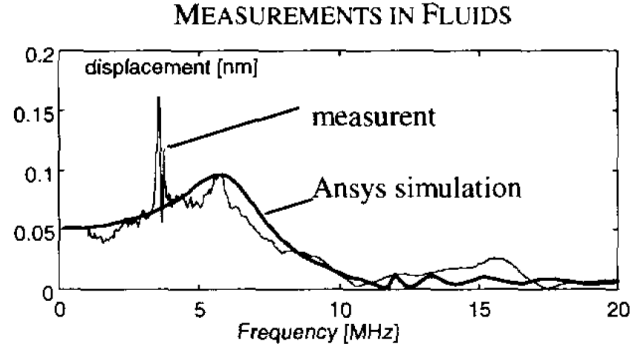


Figure 8: LDV measurement and FEM simulation for membrane displacement [18].

Bozkurt *et al.* [39] shows a modeling for the substrate loss effect of cMUTs. Their modeled sensor has 1 μm thick membrane, 1 μm thick air gap, 500 μm thick substrate, and 45 μm long radiuses (1-3.5 MHz). For measurement of the power loss, two kinds of Lamb waves were used (antisymmetric and symmetric). In the result of analysis, they proved that the antisymmetric mode is a dominant source of the loss at lower frequencies and delivers about 90 % of the total radiation power showing agreement between experiments and the modeling. Furthermore they showed that at high frequencies, symmetric is a primary source of the loss.

Bozkurt *et al.* [40] investigated optimization of electrode patterning for maximization of device performance using FEM analysis. A circular membrane model with a centered circular electrode was used. In the analysis, an electrode radius ranging 40 to 50 % of the membrane radius maximizes its performance. They found that a long radius of the membrane increases bandwidth of the sensor (Figure 9 (b)). Figure 9 (a) shows a model geometry and bandwidth result.

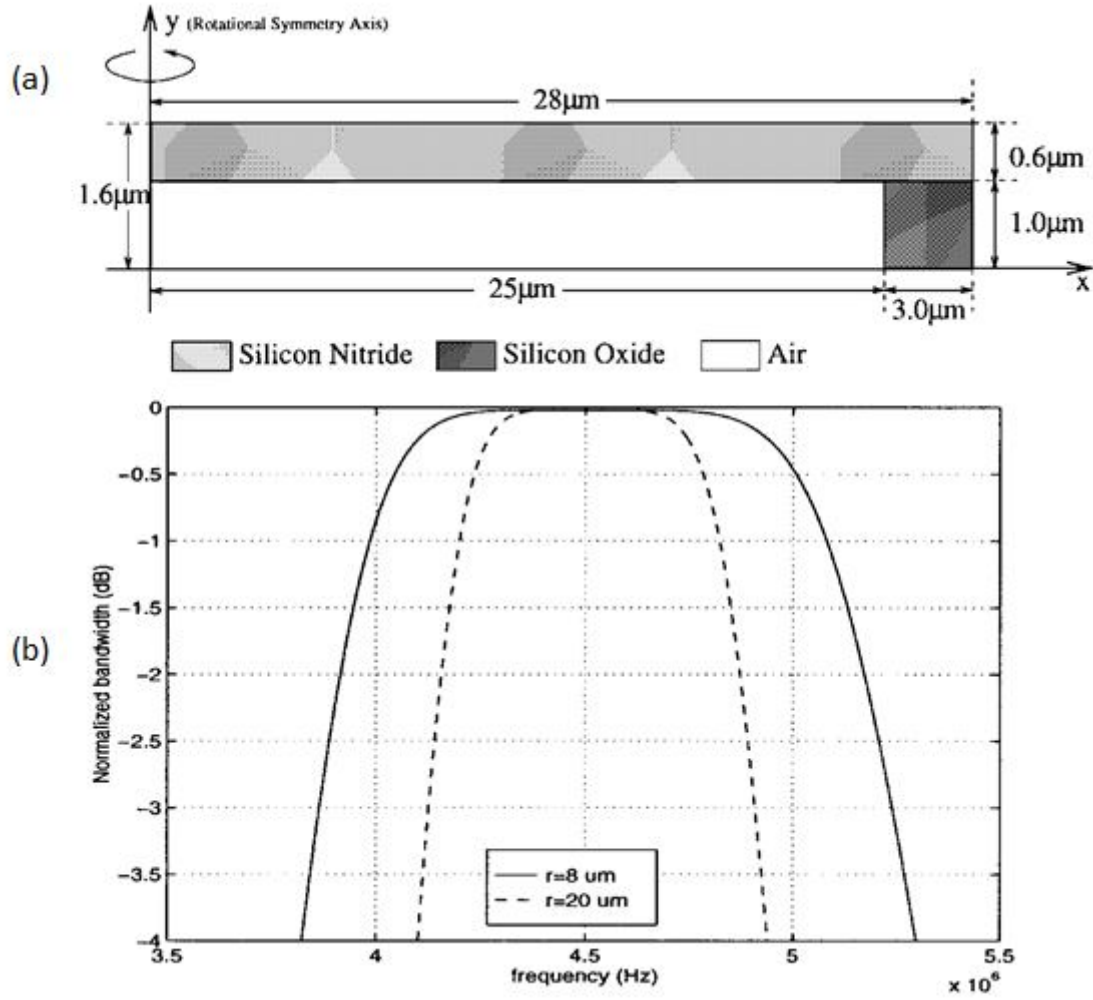


Figure 9: (a) A model geometry and (b) bandwidth result [40]

Bayram *et al.* [41] investigates the relationship between the parameters of the metal electrode and the collapse voltage. Decreasing the bottom electrode radius increases the collapse voltage (Figure 10). The material of the electrode is irrelevant with the collapse voltage if electrode thickness is small.

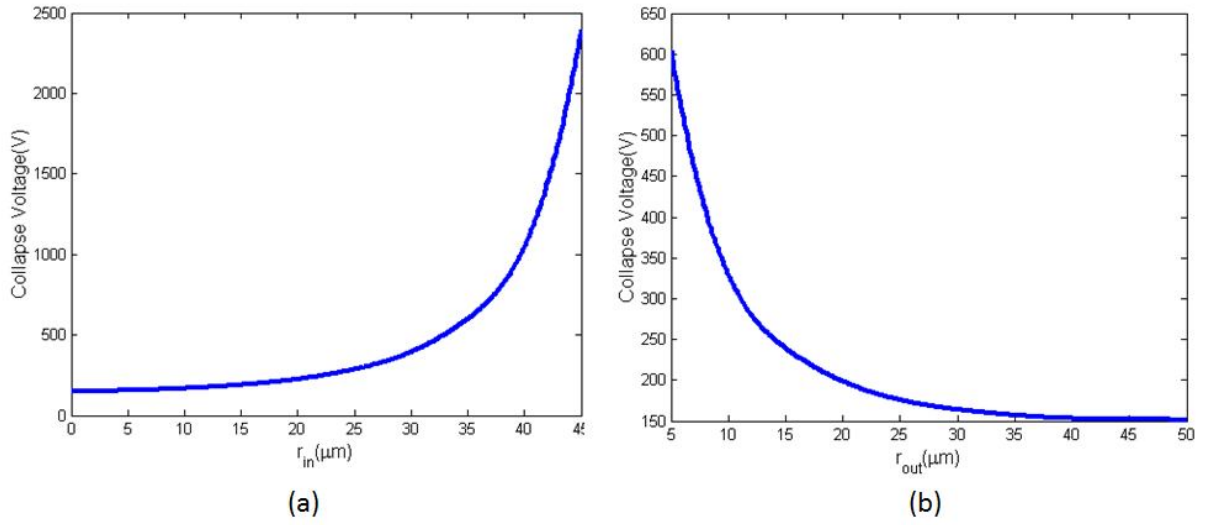


Figure 10: Effect of electrode on (a) inner radius and (b) outer radius.

Bayram *et al.* [42] investigates the collapse mode behavior of hexagonal cMUT sensors. They modeled the condition that a membrane of the sensor touches a substrate. They compared a general mode behavior with the collapse mode behavior (Figure 11).

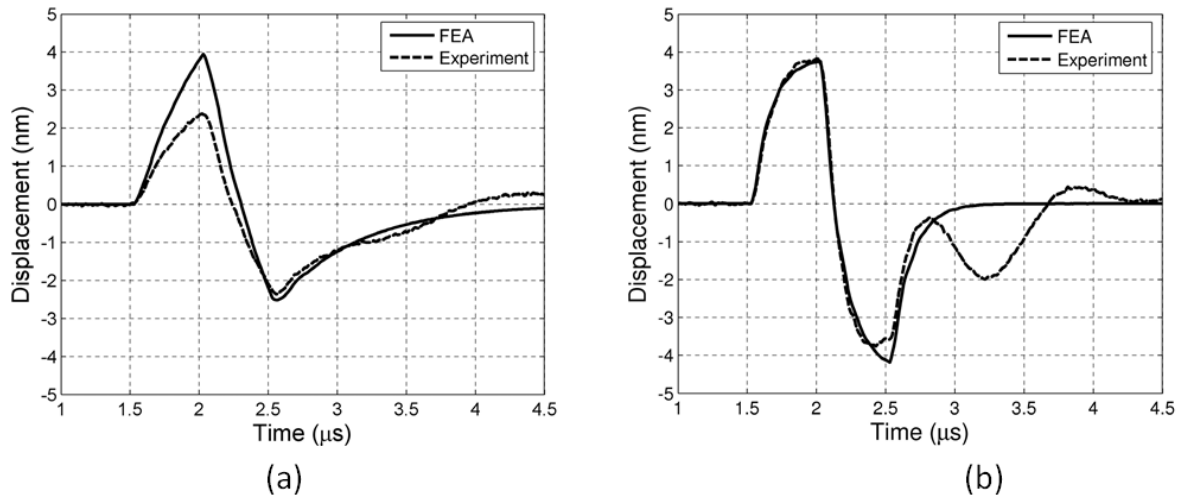


Figure 11: (a) Comparison between the conventional mode operation and (b) the collapse mode of operation [42].

2.3.3.2 Equivalent Circuit Modeling

cMUT modeling using the equivalent circuit is useful with small signal condition for linear operation. Recently many investigators used this method for an analysis of sensor behavior. Ladabaum *et al.* [28] developed a hexagonal cMUT with 300 nm thick metalized silicon nitride membranes for both air and water media. The sensor was driven at 2.3 MHz (resonant frequency), a bias voltage of 30V, and an AC voltage of 16V in air transmission. The received signal has a 30 dB signal-to-noise ratio. The distance between transmitters is 1 cm. The transducer dynamic range is approximately 110 dB. Furthermore, they developed an equivalent circuit model (plate-in-tension model). Using this model, a relationship between force and velocity is solved using a mechanical and electrical impedance model (Figure 12 (b)). Then they showed a good match between the experimental data and the simulation based on the equivalent circuit model (Figure 12 (a)).

Caronti *et al.* [43] introduced the improved equivalent model including the consideration of the interaction between a membrane and air cushion (Figure 13 (a)). They provide two models (membrane-on-air cushion model and plate-on-air cushion model) with bending stiffness and the cavity effect. They proved the importance of the air cushion, showing that there is a discrepancy of 22 % between a general plate model and the membrane-on-air cushion model.

Ahrens *et al.* [44] fabricated cMUTs with variable gap heights (50 nm and 2 μ m). They also developed an equivalent circuit model in terms of Bessel function (Figure 14 (a)). They compared experiment data with the model in terms of impedance. DC bias voltage is between 15V and 18V, AC voltage is 1V, frequency sweeps from 1 to 4.5 MHz. They have a good match between experiment and simulation (Figure 14 (b)).

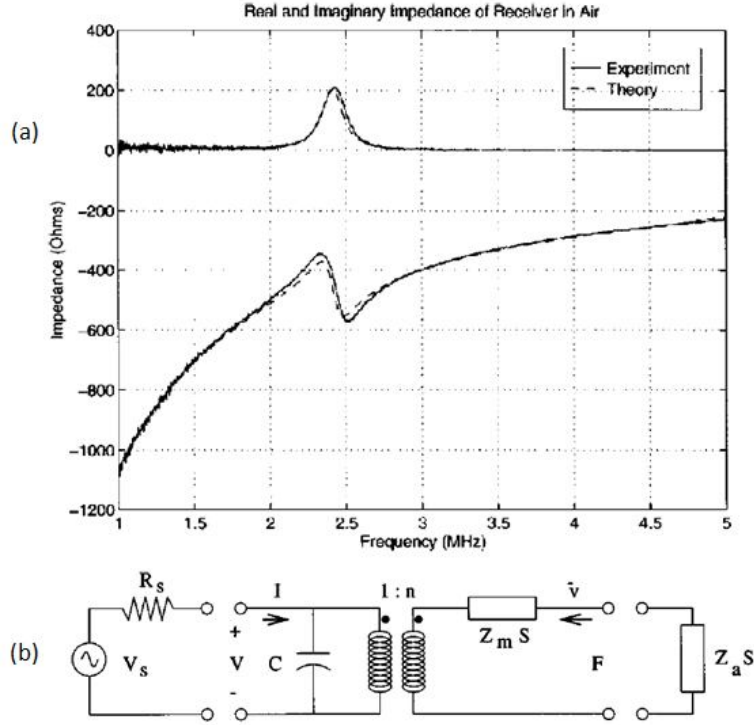


Figure 12: (a) Lumped element model, and (b) the comparison between experiment and simulation in air [28]

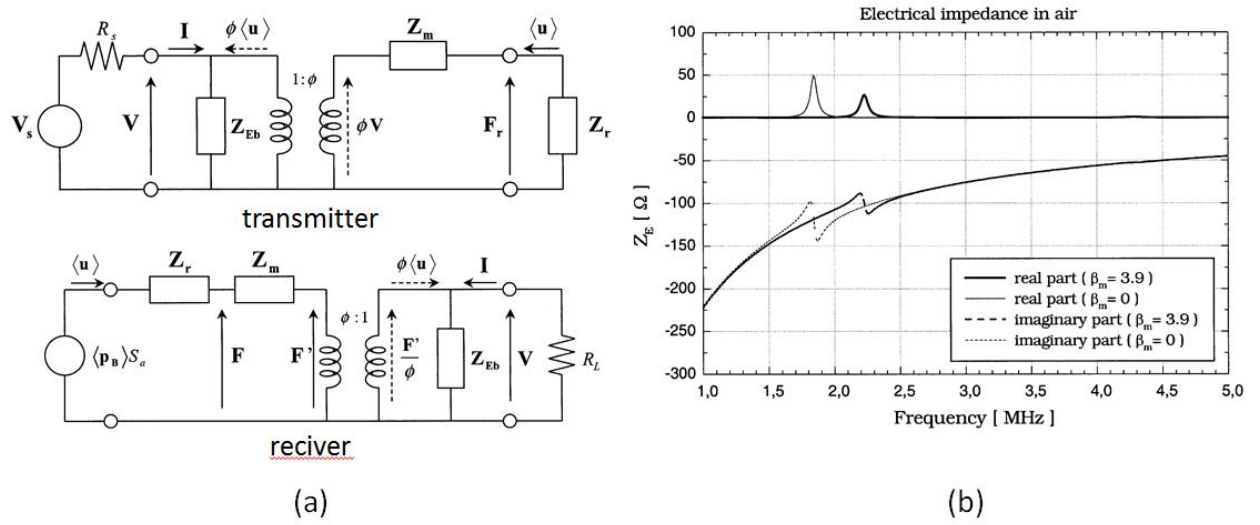


Figure 13: (a) Equivalent model, and (b) electrical impedance of air cMUT [43]

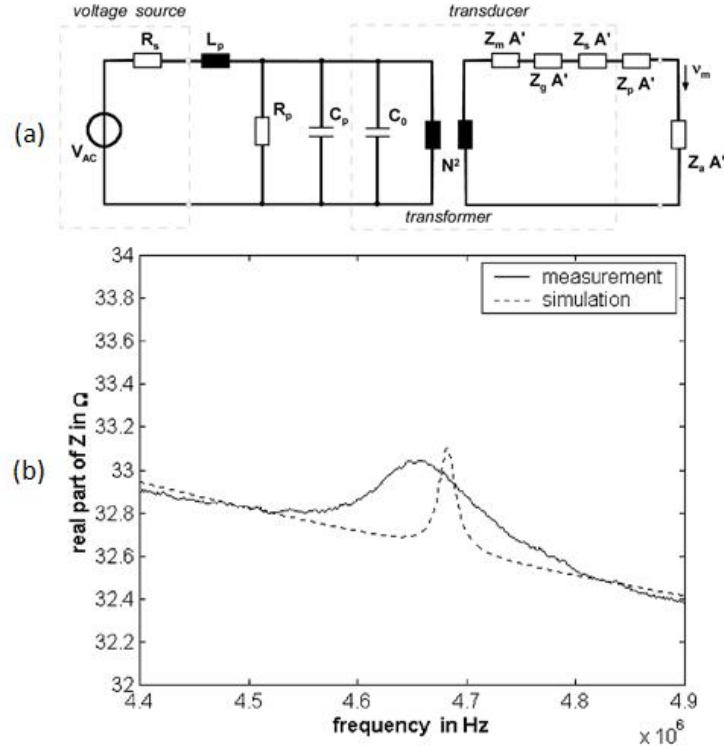
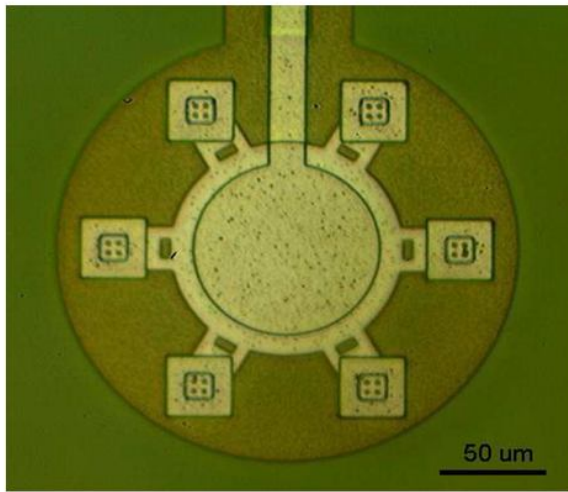
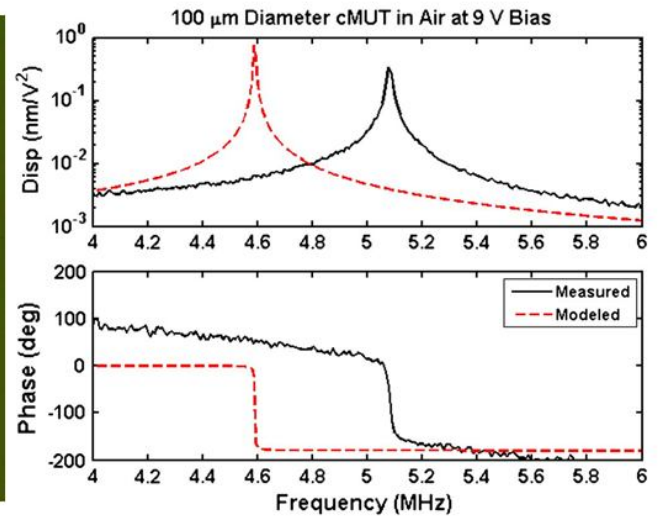


Figure 14: (a) Lumped element model, and (b) comparison between experiment and simulation [44]

Doody *et al.* [17] developed a CMOS combined cMUT technology (Figure 15 (a)). They presented a lumped element modeling for the design of this device. The device have a resonant frequency of 3.5 MHz, Q value of 2-3, pressure amplitudes of 181–184 dB re $1 \mu\text{Pa}_{\text{rms}}$ at 15 mm from the transducer on axis. The lumped element modeling includes the electrostatic coupling with electrostatic spring compliance and environmental air loading using finite element modeling (Figure 15 (c)). They compared this modeling result with experimental results using a laser Doppler velocimetry (LDV), along with water-tank measurements and in-air measurements (Figure 15 (b)).



(a)



(b)

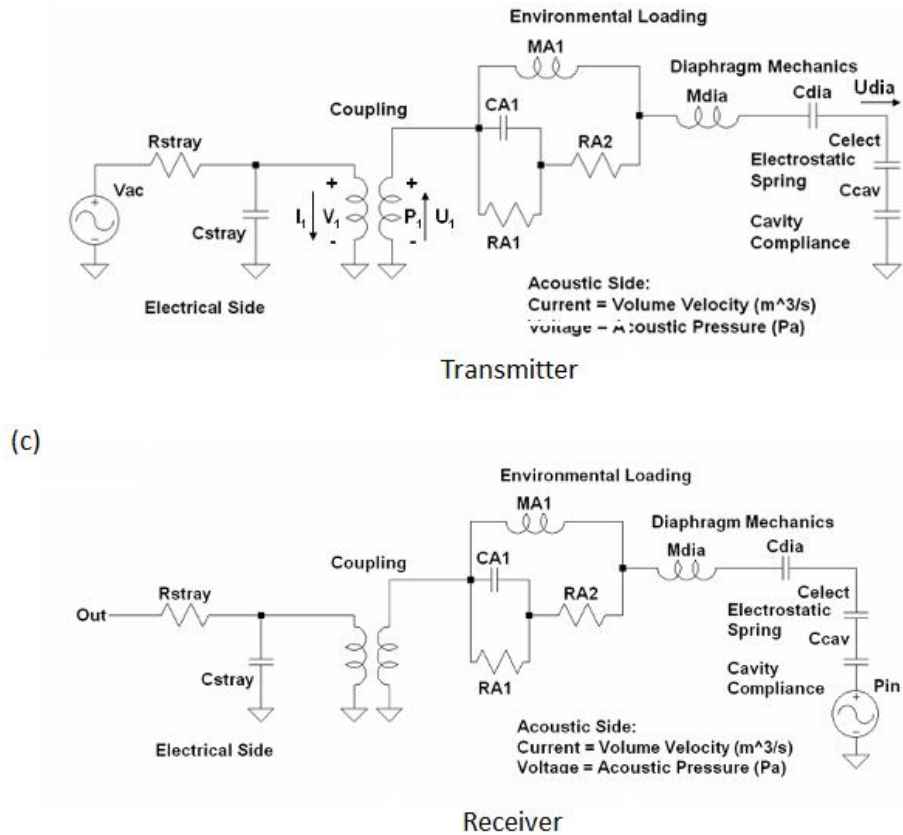


Figure 15: (a) cMUT sensor, (b) comparison between experiment and simulation, and (c) lumped element model [17]

2.3.3.3. Experimental Investigation

Caliano *et al.* [16] developed a 64-element cMUT probe. The sensor has a 400 nm thick sacrificial layer, and a SiNi membrane with 50 μm radius. This sensor can be used as a dual mode (linear array at 7 MHz and phased array at 3.5 MHz) because of a large bandwidth (>110 %). They used a connection-comb to promote connection with a commercial echographic system.

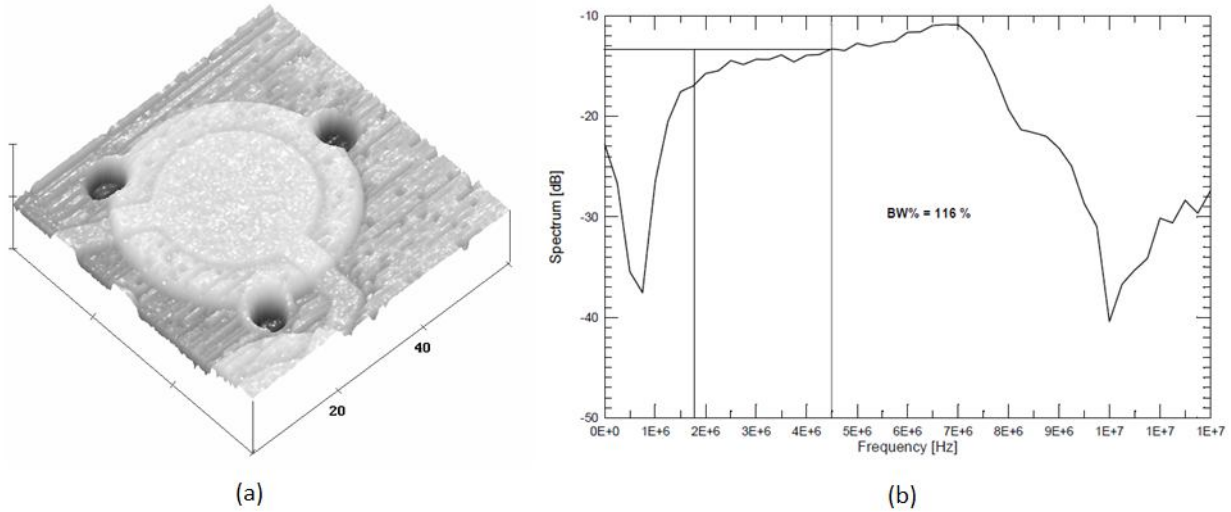


Figure 16: (a) An AFM view of a single membrane structure and (b) bandwidth of a cMUT element in water [16].

Jin *et al.* [45] developed 275 X 5600 μm 1-D cMUT arrays to solve the acoustical cross talk issues. Displacement sensitivity of the sensors is 0.28 fm/(Hz^{0.5}) and output pressure at 3 MHz with a DC bias of 35 V is 5 kPa/V . Fractional bandwidth is above 100% at 3 MHz. Stoneley wave was generated at the silicon substrate-fluid interface and Lamb wave in the silicon wafer.

Noble *et al.* [46] developed a “post-processing” cMUT sensor fully embedded with signal processing CMOS-ASIC electronics using low temperature PECVD silicon nitride deposition. The sensor has 1.3 MHz center frequency and 100% bandwidth. A charge amplifier was designed with 6.5 MHz bandwidth and noise floor is $10 \text{ nV}/(\text{Hz}^{0.5})$. Figure 17. shows a cMUT with an analogue circuit.

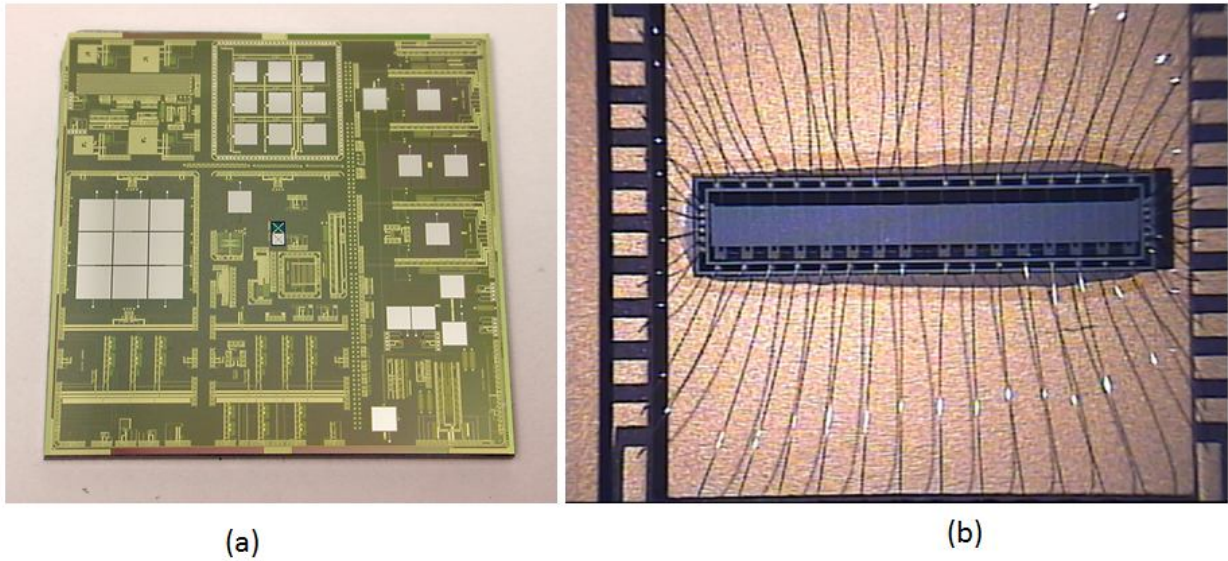


Figure 17: (a) cMUTs with analogue electronics and (b) CMOS-ASIC implementation of 16 charge amplifier array [46]

Lemmerhirt *et al.* [29] *et al* also developed CMOS based cMUT array. The 32 X 32 array was built with CMOS process for 3D image acquisition (Figure 18 (a)). Each element has $100 \mu\text{m}$ diameter membrane with $60 \mu\text{m}$ diameter top electrode and $0.6 \mu\text{m}$ gap. The center frequency of each element is 1.8 MHz. The array has a 2 mV/kPa sensitivity with 100V DC bias. Fishing lines and brass rods were used for 3D imaging (Figure 18 (b)).

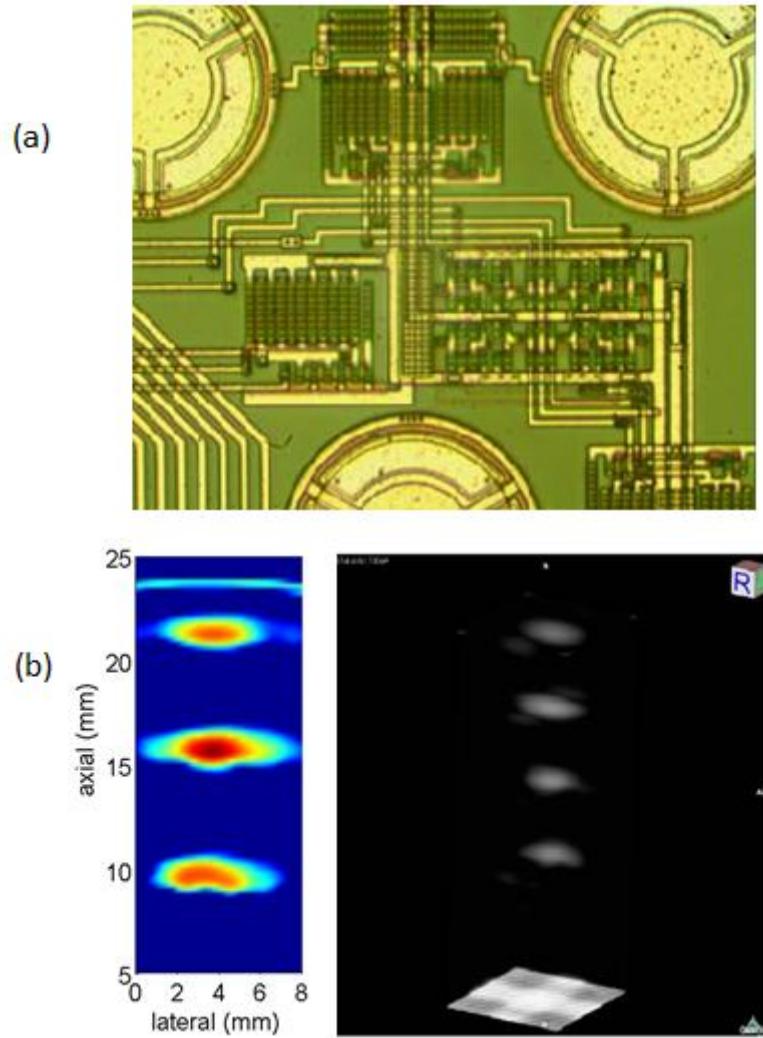


Figure 18: (a) cMUT array and (b) 2D image of brass rod and fishing line [29]

Mills and Smith [47] applied cMUT array technology to medical imaging. They provide in-vivo imaging of a carotid artery with cMUT sensors. They compared cMUT images with piezoelectric sensor images. The PZT array (GE LOGIQ 9) image shows 10 dB higher sensitivity than cMUT image, but the cMUT array shows higher bandwidth (110%) than the piezoelectric sensor (70-80%) (Figure 19 (b)). The cMUT sensors show good axial resolution.

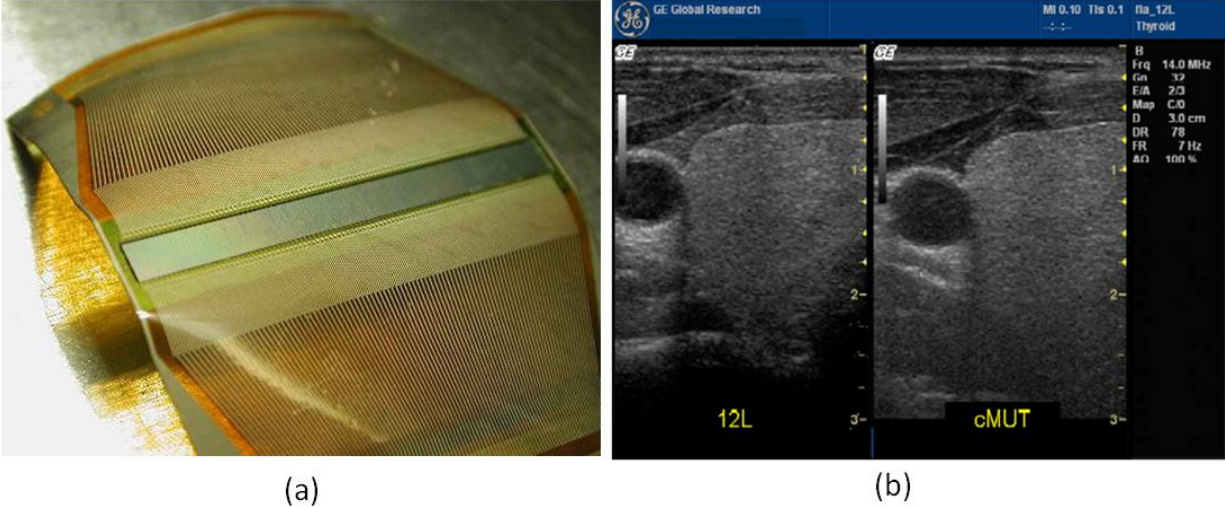


Figure 19: (a) cMUT array with flexile circuit and (b) in-vivo images of the carotid artery and thyroid gland by PZT array and cMUT [47].

Wygant *et al.* [48] developed an integration circuit for 3D imaging. IC and 16 X 16 cMUT sensors are imbedded on a chip. In a receiver, 32 elements along the array diagonals were used in the chip and other elements operate as a transmitter. They used flip-flop wire bonding for simple connection between cMUT and IC (Figure 20 (a)). IC with a shift register and a comparator was fabricated using BiCMOS process. FPGA was used for data acquisition and IC communication. They provide IC performance without connection with cMUT. Furthermore, they acquired 2D images using an integrated cMUT sensor (Figure 20 (b)).

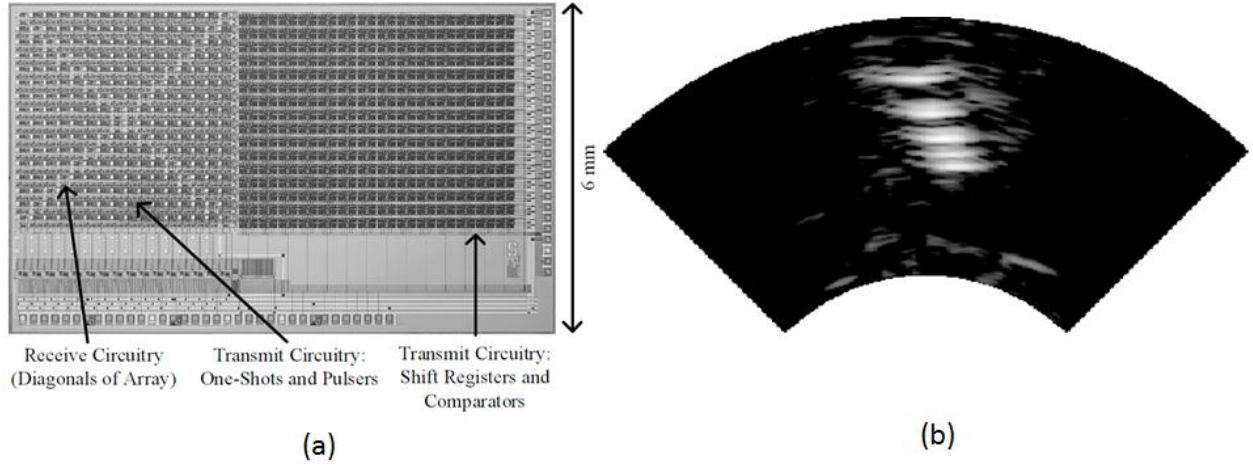


Figure 20: (a) IC and (b) 2D image of nylon wire phantom [48]

Vaithilingam *et al.* [49] showed 3D photoacoustic imaging (PAI) using 2D cMUT array technology and integrated electronics (Figure 21 (a)). PAI can provide the contrast information of optical imaging and the spatial resolution of acoustic imaging simultaneously. A fishing line phantom was used for measurement of resolution (Figure 21 (c)) and chicken breast tissue was also used for 3D image rendering (Figure 21 (d)).

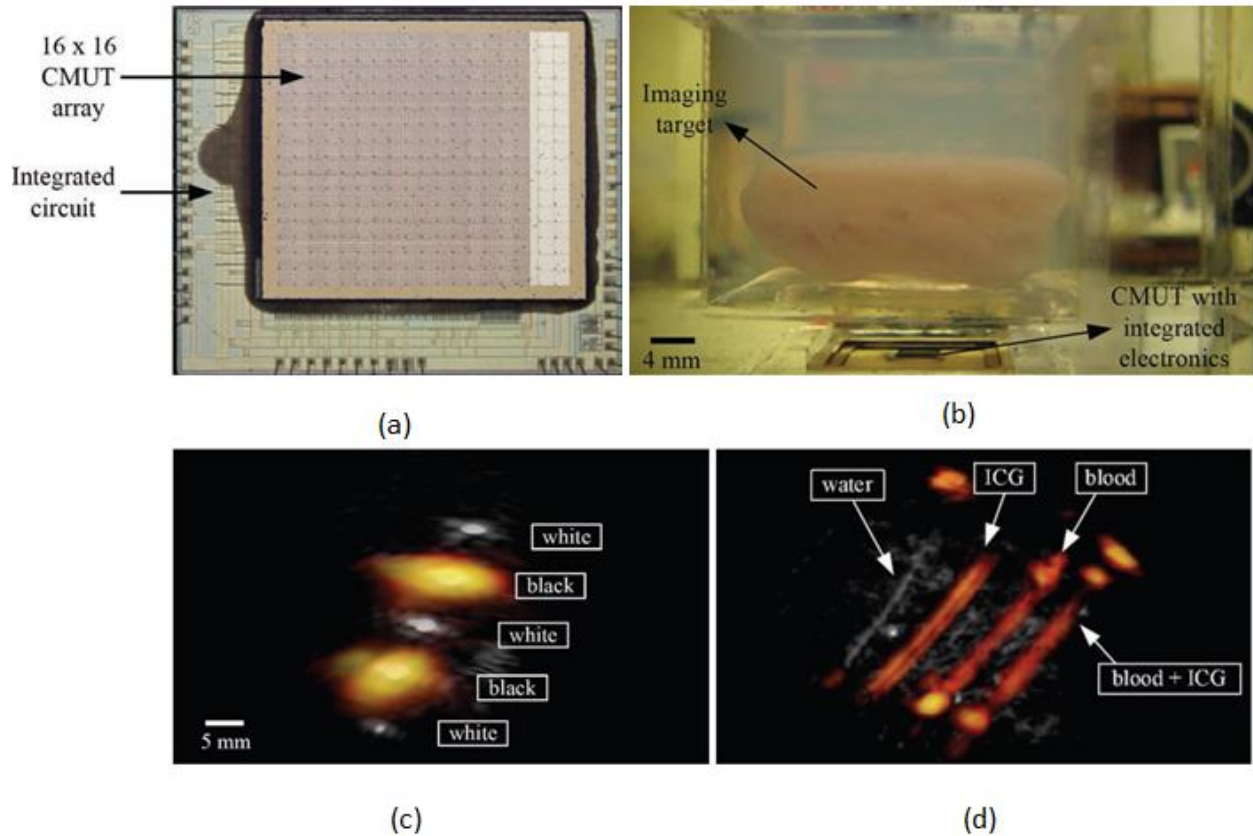


Figure 21: (a) cMUT device, (b) experimental set-up, (c) 3D photoacoustic (hot-metal color scale) image overlaid on a pulse-echo image (gray-scale) of fishing line, and (d) chicken breast [49]

2.4 MEMS-Based Range Finder

Micro-electro-mechanical systems (MEMS) continue to grow more complicated and multifunctional. These systems often include both sensing and actuating capabilities that allow for the fabrication of a variety of devices. Sensing subsystems are of primary importance for all types of microscale detection. In the sensing area, a MEMS-based rangefinder has advantages including low cost and high portability with a small size even though it also has disadvantages with weak output pressure and short distance [50].

Kuratli *et al.* [50] developed a MEMS-based acoustic rangefinder embedded with $0.8\ \mu\text{m}$ CMOS. The device is driven by thermal actuation system and generates ultrasound. Operation frequency of the device is 100 kHz and the range is 11 cm. They used the phase shift method to compensate a disadvantage of CW measurement and ToF measurement: short range.

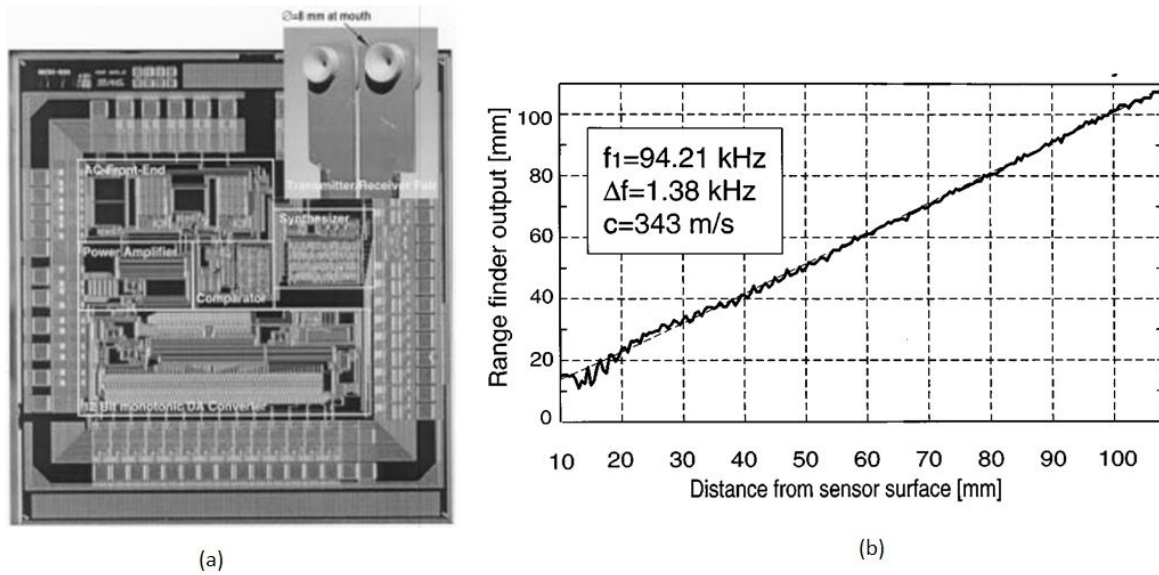


Figure 22: MEMS-based range finder. (a) Package with CMOS and transducer, and (b) range test result [50].

Przybyla *et al.* [11, 51] developed an ultrasound rangefinder using AlN based piezoelectric micromachined ultrasound transducer (pMUT) technology. The first device operates at 375 kHz and the range is 45 cm. SPL of the device is 85 dB at the resonant frequency. They measure the distance between the sensor and a target using a ToF method. As the distance increases, signal attenuation causes an increase in the signal noise [11]. They also developed an advanced device with distance $> 1\ \text{m}$ as shown in Figure 23. The device has a resonant frequency of 215 kHz and quality factor Q is 20 [51].

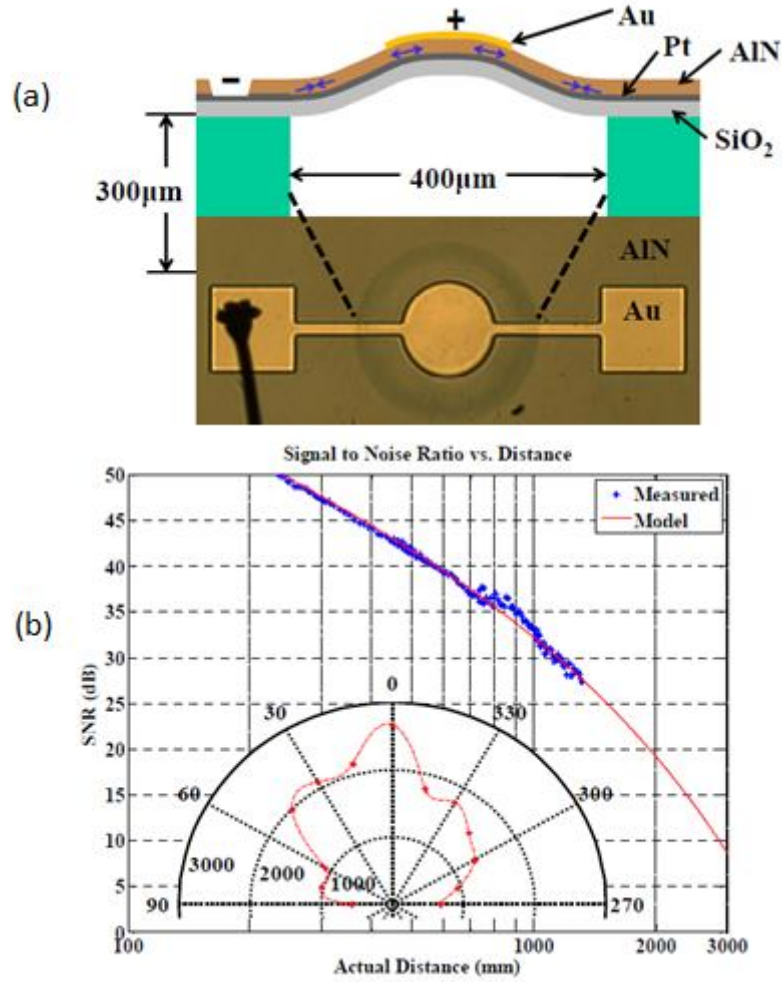


Figure 23: (a) pMUT-based range finder with distance > 1 m, and (b) Signal-to-Noise ratio vs distance [51].

Przybyla *et al.* [10] also showed a 2D ultrasonic depth sensor using pMUT technology. They used a transmitter and 7 receiver elements for angle measurement. Detection range is a 750 mm maximum range and $\pm 35^\circ$ angle span. A membrane has 2 μm thick AlN/Mo/AlN/Al layer as shown in Figure 24 (a). The device has a resonant frequency of 190 kHz and quality factor Q is 15. They calculate the angle at which the transmitted waves reach the receive transducer, using the difference in arrival time between adjacent elements in Figure 24 (b).

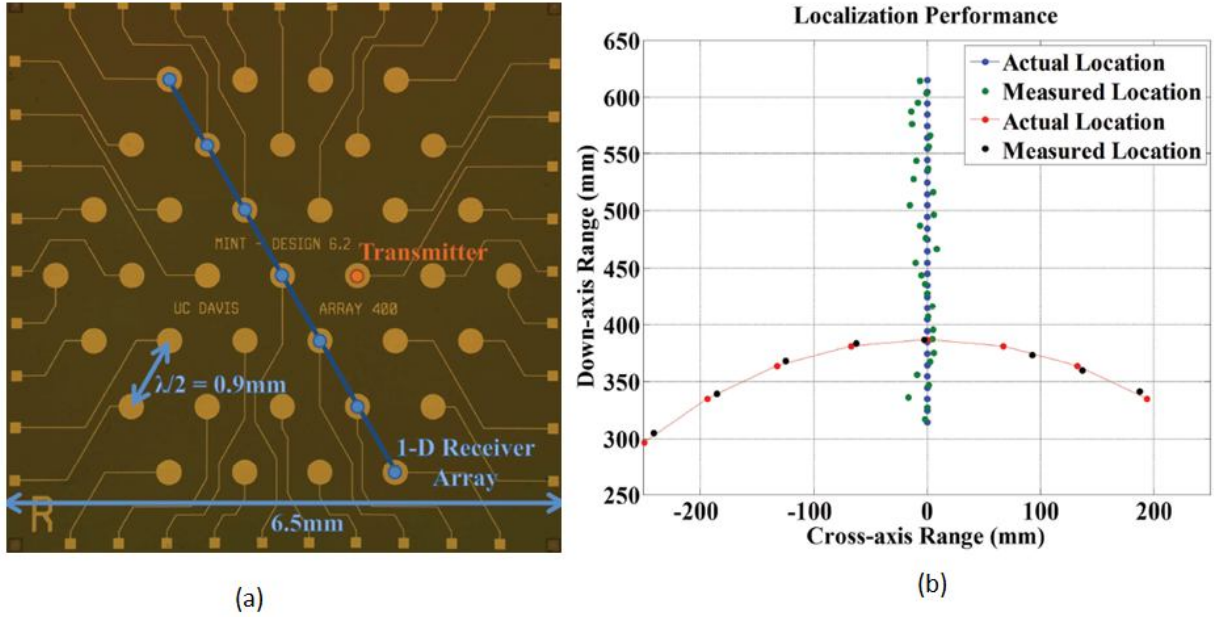


Figure 24: (a) pMUT array with transmitters and receivers, and (b) the result of the angle measurement [10].

Yamashita *et al.* [52] developed ultrasonic phased array sensors with scattered resonant frequencies, using piezoelectric materials (Figure 25). For signal processing, a wavefront was used for delay-summation method. The device has a membrane with a gold top electrode, piezoelectric thin film, and Pt/Ti electrode with a resonant frequency of 80 kHz.

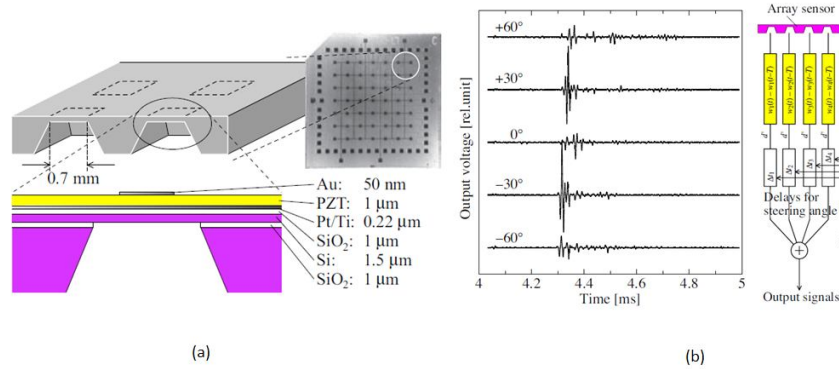


Figure 25: (a) Sensor array, and (b) the result of the distance measurement [52].

| | Frequency (kHz) | Technology | Range (m) | Drive Voltage (V) | Resolution |
|------------------------------|--------------------|---------------|--------------|---------------------------------|------------|
| Kuratli <i>et al.</i> [50] | 100 | Thermal | 0.11 | V_{pp} : 3, V_{bias} : 5 | - |
| Przybyla <i>et al.</i> [51] | 215 | pMUT | 1.3 | - | - |
| Przybyla <i>et al.</i> [10] | 190 | pMUT | 0.5 | V_{pp} : 30 | 5 cm |
| Yamashita <i>et al.</i> [52] | 80 | Piezoelectric | >0.7 | - | - |
| This work | 180 | cMUT | 1.5 | V_{pp} : 140, V_{bias} : 10 | 1 cm/s |

Table 2: Comparison between this work and other MEMS-based rangefinders.

Comparing our devices with other MEMS-based rangefinders in Table 2 shows the key factor of the rangefinder development: long range with low drive voltage. A range of other devices [10, 50-52] is 0.1 m – 1.3 m. The short range limits device applications. However, the current cMUT device provides a longer range than the piezoelectric rangefinders. This allows for various long range applications: environmental measurements with rain and ice, sports applications like running sensors, security systems, and industrial applications like robot positioning.

The piezoelectric sensors use small drive voltages due to a large linear displacement [10] as shown in Table 2. However, the cMUT sensors use high voltage (140 V_{pp}). Use of the high voltage drive can cause high power consumption and safety issues. The drive voltage of the cMUT devices needs to be reduced.

Chapter 3

Design

This chapter discusses the design of cMUT sensors. Two kinds of cMUTs, the PolyMUMPs chip and the nickel-on-glass chip, are introduced. The first section shows the structure of the PolyMUMPs® chip and its fabrication by the MEMSCAP foundry service. The second section introduces the structure of the nickel-on-glass chip and its fabrication based on a custom process including nickel plating and copper plating to deposit a thick metal structure. This procedure can provide fast turnaround, flexibility and low cost. Furthermore, this procedure can produce low stray capacitance sensors using a glass wafer. This is one of the major drivers of system noise reduction.

3.1. PolyMUMPs® Chip

3.1.1. Structure

The polysilicon cMUT sensors consist of a membrane with 600 μm diameter, an anchor, dimples (prevention for membrane stiction), vent holes, a corrugation (to relax the tensile residual stresses during fabrication), and a bottom electrode (Figure 26). The device was designed with the resonant frequency 185 kHz, to achieve an approximately 10 degree beamwidth with a 1 cm aperture, and safely to reduce the resonant frequency with gold.

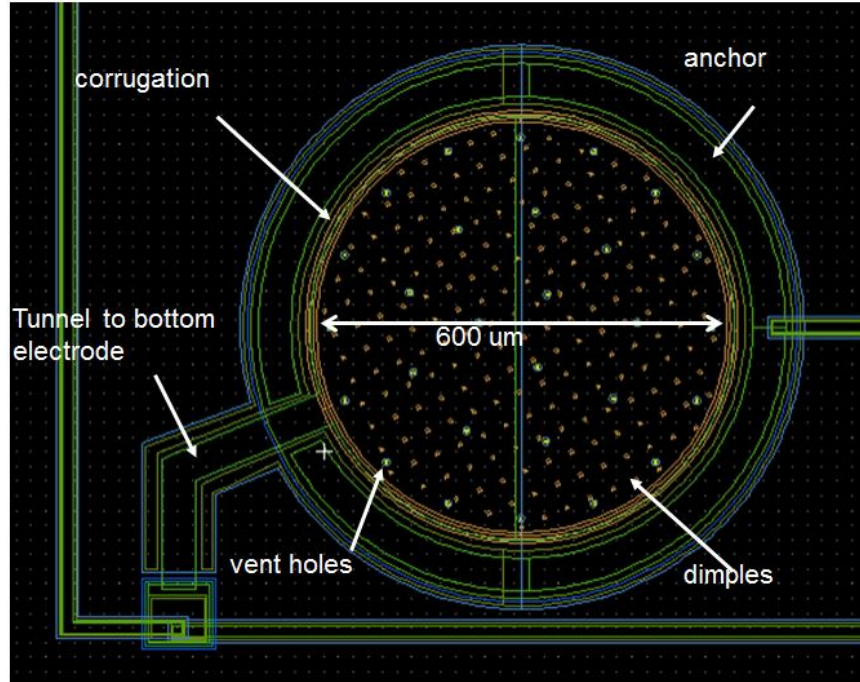


Figure 26: Schematic of a single element (top view).

3.1.2. Fabrication

The cMUT sensor array was fabricated using the MEMSCAP PolyMUMPs® process along with facilities at Tufts University in the Tuft Micro and Nano Fabrication Facility (TMNF). PolyMUMPs® is a foundry process that manufactures polysilicon structure using surface micromachining. Seven physical layers, including three structural, two sacrificial and one metal layer are used in the process.

The fabrication procedure for the sensor begins with a silicon wafer with high phosphorus surface doping as shown in Figure 27 (1). Low pressure chemical vapor deposition (LPCVD) is utilized to deposit a 600 nm silicon nitride as shown in Figure 27 (2). After the deposition of silicon nitride, 500 nm thick polysilicon (the Poly 0 layer) is deposited for the

building of the bottom electrode by using LPCVD, and then patterned by photolithography and plasma etching as shown in Figure 27 (3). After the bottom electrode layer is deposited, a 2 μm oxide sacrificial layer is deposited by LPCVD and annealed for 1 hour at 1050 $^{\circ}\text{C}$ as shown in Figure 27 (4). This heavily dopes the Poly 0 layer.

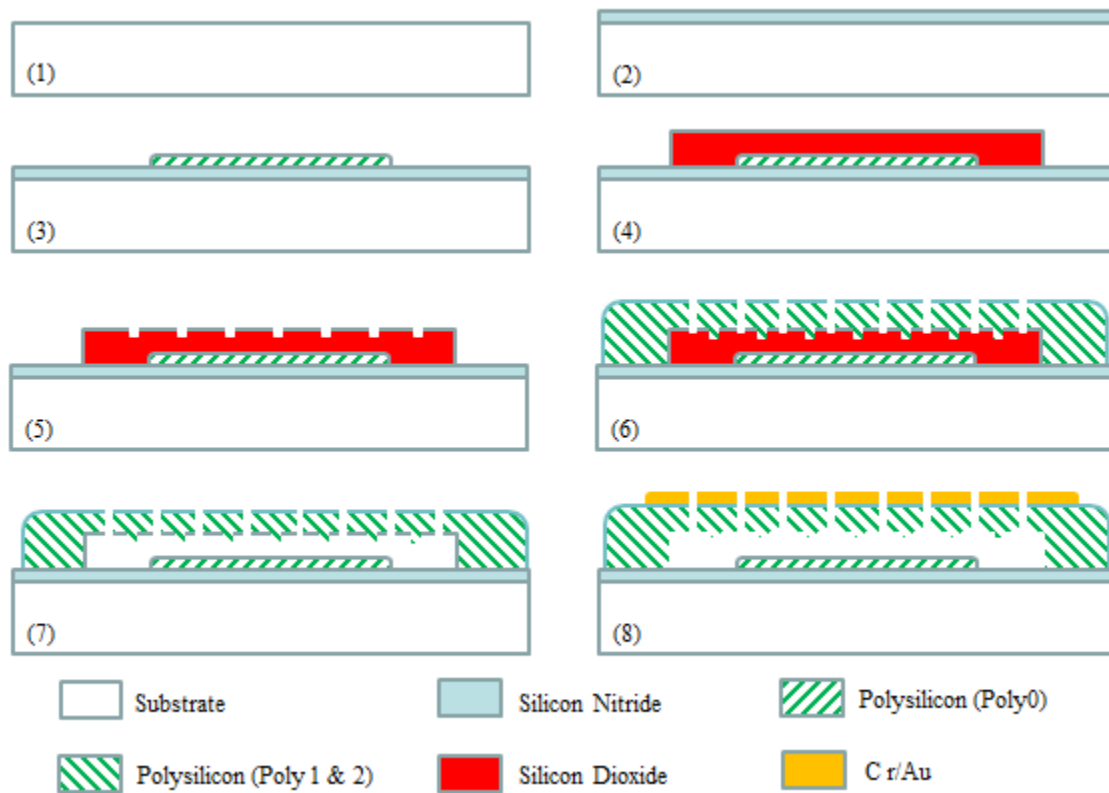


Figure 27: Schematic illustrates the fabrication process using the MEMSCAP PolyMUMPs® process.

750 nm deep dimples are etched in the phosphosilicate glass (PSG) using reactive ion etching as shown in Figure 27 (5) [53]. The anchor regions are then defined by lithography and

RIE. Subsequently, 2 μm polysilicon (Poly 1) is deposited by LPCVD and patterned in a similar fashion as shown in Figure 27 (6). This is the first structural layer.

After the deposition of the first structure layer, a 2nd PSG layer with a thickness of 750 nm is deposited and patterned. For the sensor described here, oxide 2 is completely removed. Following this, the second structure layer of polysilicon (Poly 2) with 1.5 μm thickness is deposited by LPCVD and patterned by RIE. Both polysilicon layers are heavily doped with phosphorous by diffusion from the PSG layers. The diaphragm structure is constructed from both polysilicon layers for a total polysilicon thickness of 3.5 μm . The final step in the PolyMUMPs® process is the deposition of a 500 nm thick layer of Cr/Au, which is patterned by liftoff. This layer is used for electrical interconnect and the bond pads.

After the PolyMUMPs® process, the device is released by etching the sacrificial oxide using 4:1 Hydrofluoric Acid (49%): Hydrochloric Acid (37%) mixture for 150 minutes as shown in Figure 27 (7). Note that the addition of HCl to the release etch is critical. Without HCl, the etch rapidly attacks the polysilicon grain boundaries, dramatically increasing series resistance. After the release etch, one additional Au layer (1.5 micron thick) is deposited to reduce the resonant frequency of the sensor as shown in Figure 27 (8). The Au layer is deposited by sputtering through a stainless steel shadow mask. The shadow mask is 0.006" thick, 5 cm \times 5 cm. A design of the shadow mask is shown in Appendix C.5. Next, the chip is packaged in a ceramic DIP package using epoxy and wirebonded. Figure 28 shows the schematic of the complete sensor. Table 3 and Table 4 give the geometric and the material properties of the sensor structure. The radius of the device (300 μm) was chosen in order to tune the resonant frequency and reduce stiction risk.

| | Property | Value | Units |
|--------------|--|-------|----------------------|
| a | Radius of diaphragm | 300 | μm |
| A_{bottom} | Radius of bottom electrode | 300 | μm |
| t_{poly} | Thickness of polysilicon Layer | 3.5 | μm |
| t_{gold} | Thickness of Gold Layer | 1.5 | μm |
| A_{hole} | Radius of diaphragm vent holes | 2 | μm |
| C_c | Center-to-center spacing of vent holes | 100 | μm |
| n | Number of vent holes in diaphragm | 28 | <i>Dimensionless</i> |

Table 3: Geometric properties of the PolyMUMPs® cMUT sensor

| Symbol | Property | Value | Units | Reference(s) |
|---------------|--------------------------------------|-------|--------------------|--------------|
| ρ_{poly} | Density of polysilicon | 2320 | kg/ m ³ | [54] |
| ρ_{gold} | Density of gold | 19300 | kg/ m ³ | [55, 56] |
| E_{poly} | Modulus of elasticity of polysilicon | 158 | GPa | [57, 58] |
| E_{gold} | Modulus of elasticity of gold | 80 | GPa | [55, 56] |
| ν_{poly} | Poisson's ratio of polysilicon | 0.22 | Dimensionless | [57, 58] |
| ν_{gold} | Poisson's ratio of gold | 0.44 | Dimensionless | [55, 56] |

Table 4: Material properties of a diaphragm

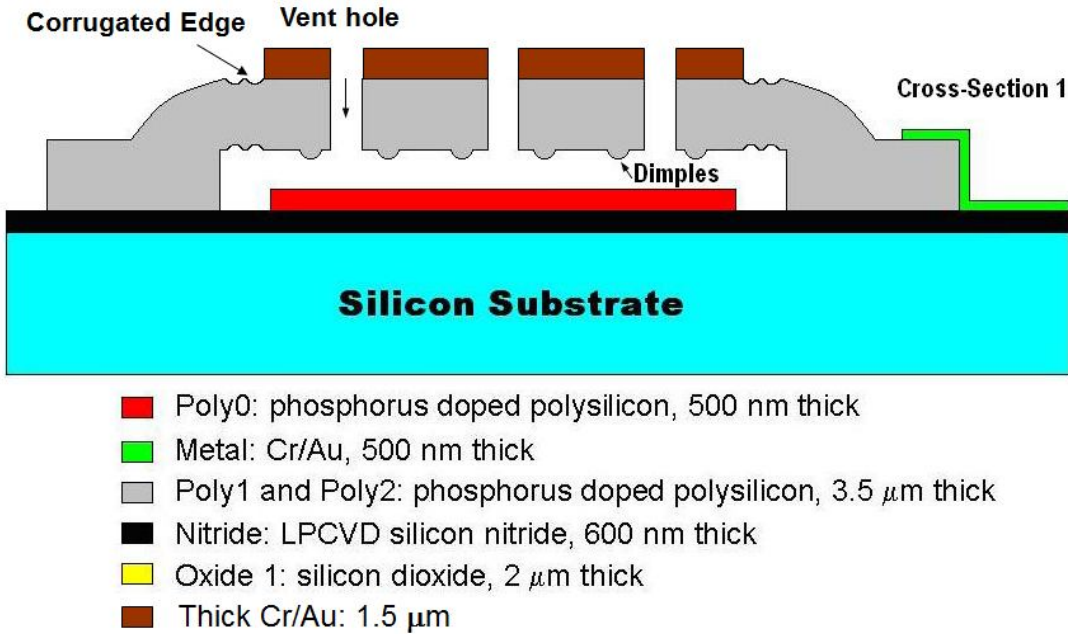
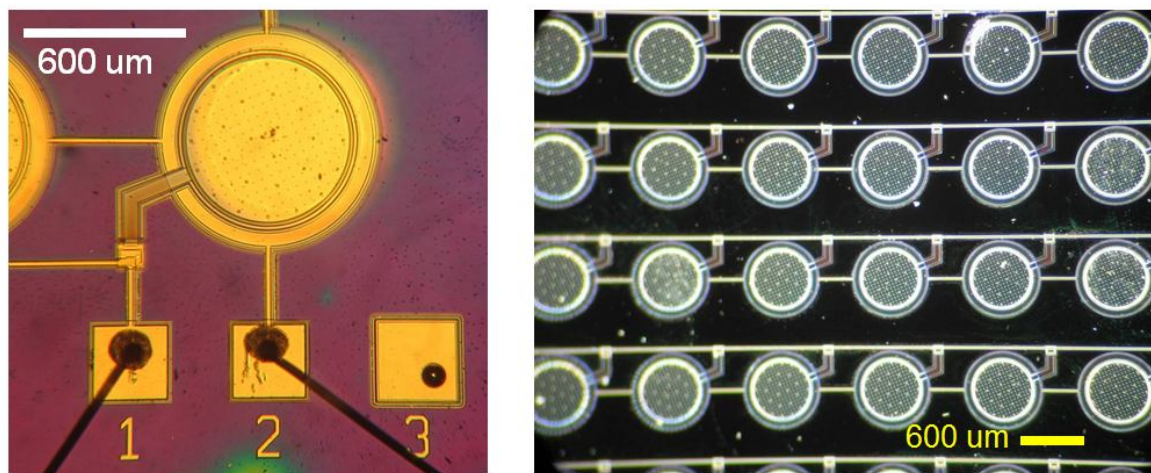


Figure 28: Schematic of one element in the cMUT sensor array showing the cross-sectional diagram after Au deposition.



Single Element After Packaging **Portion of array – Darkfield Illumination**

Figure 29: Photograph of a single element (left) and the cMUT arrays in an 8×8 pattern (right).

The cMUT sensor array consists of an 8×8 pattern where the elements are arrayed on a $1.01 \text{ cm} \times 1.01 \text{ cm}$ chip, as shown in Figure 29. Every sensor is connected in parallel. There are 2 bonding pads along the bottom edge of the chip for electrical connection. The element center-to-center pitch is 1.1 mm. Packaging uses a ceramic dual in-line (DIP) package to which the MEMS array is wirebonded. The device was designed with the resonant frequency 185 kHz, to achieve an approximately 10 degree beamwidth with a 1 cm aperture, and safely to reduce the resonant frequency with gold.

3.2. Nickel-on-glass chip

3.2.1. Structure

A nickel-on-glass cMUT sensor consists of a membrane with $600 \text{ }\mu\text{m}$ diameter, an anchor, and a bottom electrode (Figure 30). The device was designed with the resonant frequency 175 kHz, to achieve an approximately 10 degree beamwidth with a 1 cm aperture.

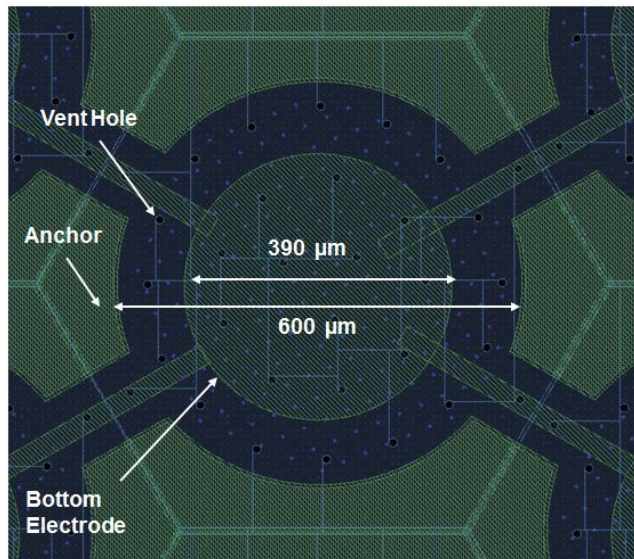


Figure 30: Schematic of a single element (top view).

3.2.2. Fabrication

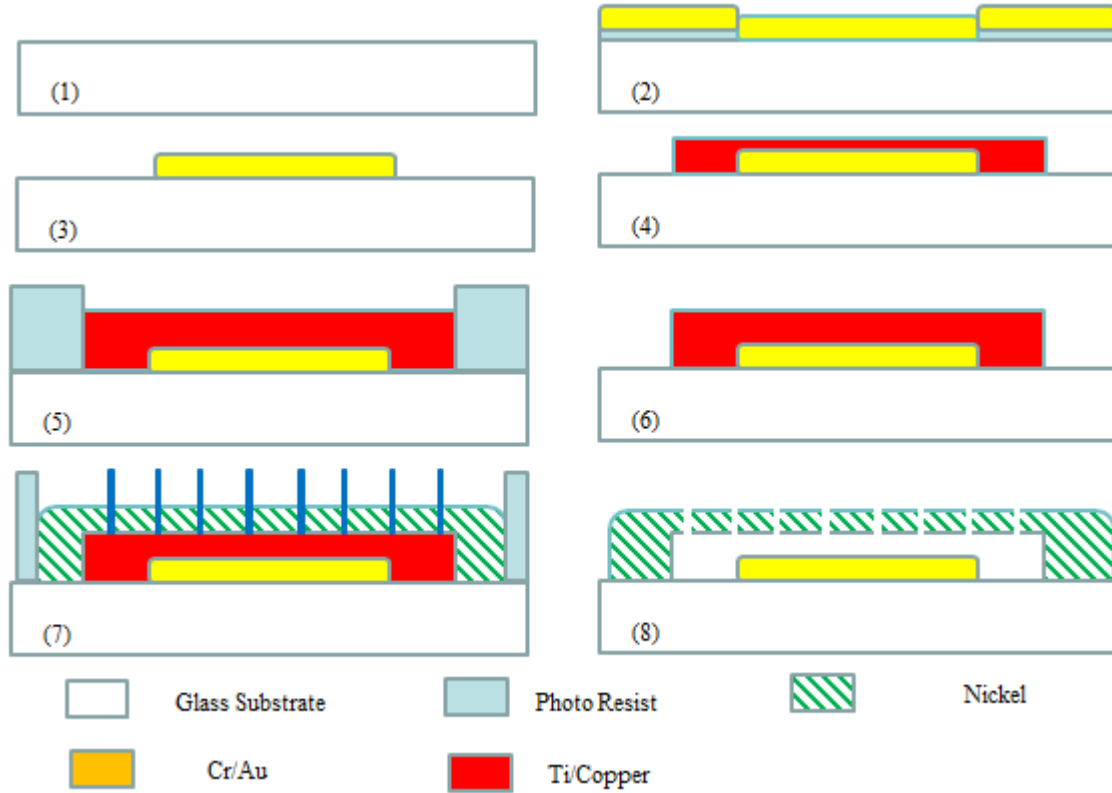


Figure 31: The fabrication process using the nickel plating and the copper plating.

The complete fabrication procedure is given in appendix A. The cMUT sensor was fabricated with nickel surface micromachining in the Tufts Micro & Nano Fabrication facility (TMNF). The process starts with a 550 μm thick soda lime glass wafer as shown in Figure 31 (1). To clean the wafer, piranha clean was done for 5 min. 75 nm/225 nm thick Cr/Au interconnects (a bottom electrode and bonding pads) are deposited with sputtering and patterned by liftoff using liftoff resist (LOR) and AZ 9245 photoresist as shown in Figure 31 (2, 3).

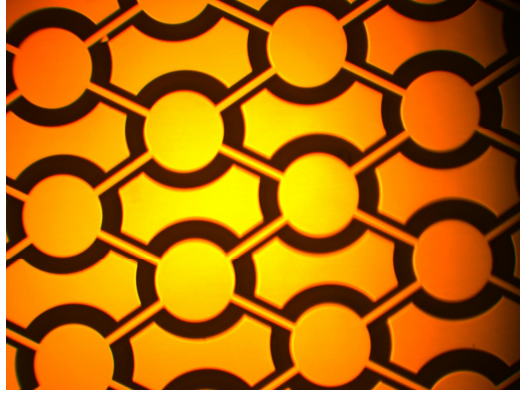


Figure 32: Cr/Au interconnect and bottom electrodes after the liftoff.

Then another thin seed layer of Ti/Cu (30nm/300nm) was deposited in preparation for copper plating and is patterned by liftoff using LOR as shown in Figure 31 (4). 8 μm thick AZ 9245 photoresist is spun as shown in Figure 31 (5). Before copper plating, a copper oxide was removed with copper plating solution. A 5 μm sacrificial layer of copper was electroplated on the top of seed layer to cover the entire substrate except contact region for 35-40 min as shown in Figure 31 (6). Plating rate is ≈ 150 nm/min. After the copper plating, the sacrificial layer is complete.

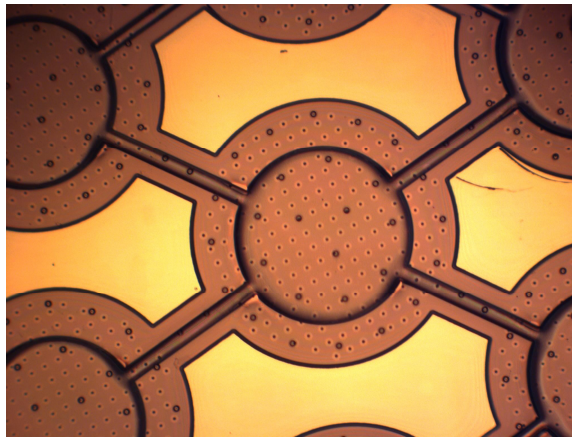


Figure 33: Copper sacrificial layer and Cr/Au interconnection after the copper plating.

An AZ 9260 mold is then deposited and photo-patterned. The 9 μm thick structure was electroplated in the commercial nickel plating solution for 90-100 min as shown in Figure 31 (7). Plating rate is ≈ 100 nm/min and surface roughness R_a is 31-43 nm. The structure layer completes. To minimize the surface roughness of plated structure in the both plating procedures, the small plating current (≈ 5 mA/cm²) was driven, as well as agitating and filtering the plating solution.

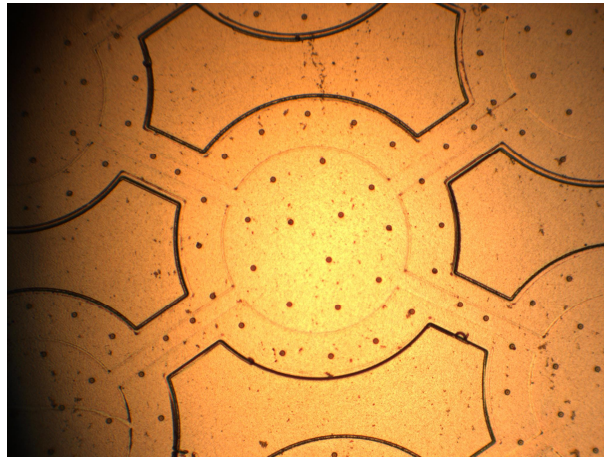


Figure 34: Nickel structure layer with vent holes after the nickel plating.

At this point, a protective photoresist layer was spun on for dicing the wafer. Finally, the sacrificial layer was etched away in a mixture of 1 part Acetic Acid to 1 part 30% Hydrogen Peroxide to 18 parts DI water for 24 hours, and then chip is rinsed in water, isopropanol, and methanol. It is finally allowed to air dry in a dry box that is flooded with clean dry air with a low relative humidity as shown in Figure 31 (8).

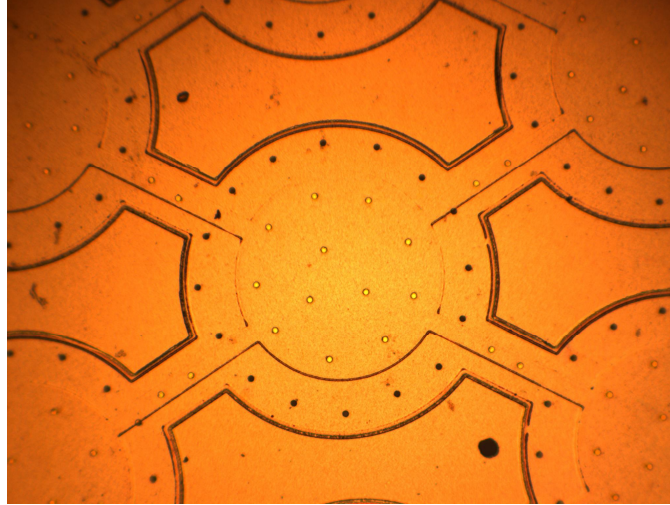


Figure 35: Nickel structure after the release with the acetic acid, hydrogen peroxide, and water etch.

The chip is next packaged into a 16 pin DIP package. The package is ball bonded to the chip using 25 micrometer diameter gold wire. Table 5 and Table 6 give the geometric and the material properties of the sensor structure. Figure 37 and 38 show SEM pictures of completed devices.

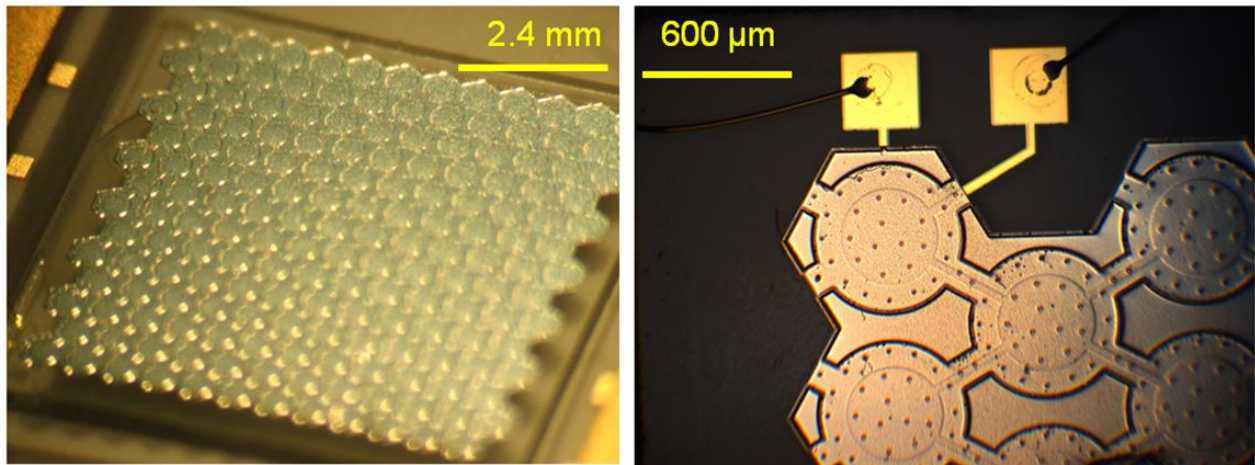


Figure 36: Photograph of nickel cMUT array after packaging (left) and the cMUT arrays in zoom-in (right).

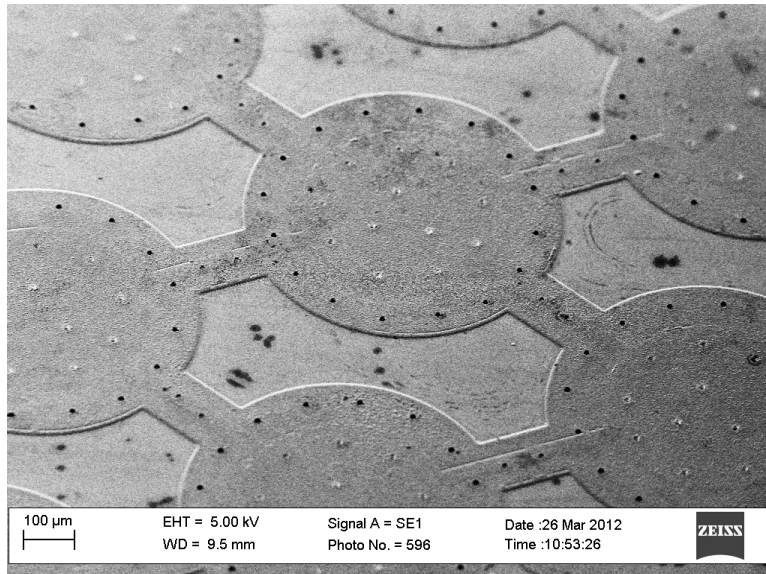


Figure 37: SEM of the nickel cMUT array after the release.

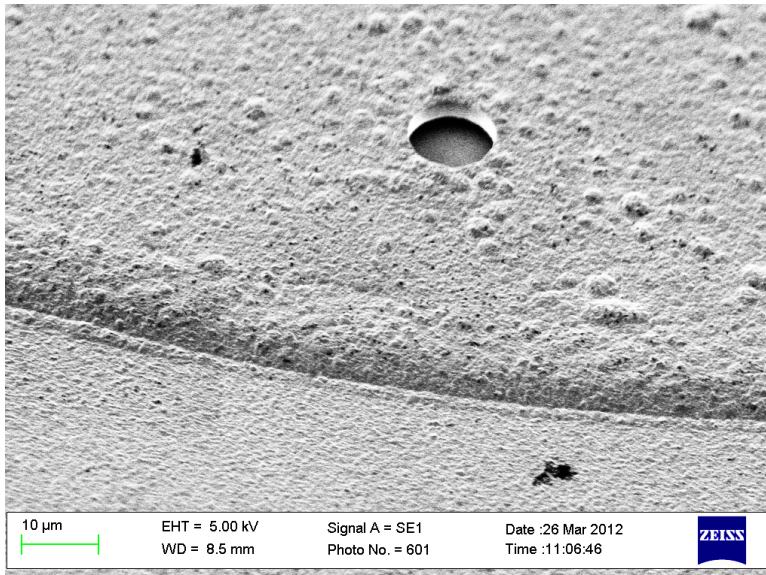


Figure 38: SEM of a vent hole after the release.

| Symbol | Property | Value | Units |
|--------------|-----------------------------------|-------|---------------|
| A | Radius of diaphragm | 300 | μm |
| A_{bottom} | Radius of bottom electrode | 195 | μm |
| t_{nickel} | Thickness of nickel Layer | 9 | μm |
| t_{gap} | Thickness of sacrificial Layer | 5 | μm |
| A_{hole} | Radius of diaphragm vent holes | 5 | μm |
| N | Number of vent holes in diaphragm | 28 | Dimensionless |

Table 5: Geometric properties of the nickel-on-glass cMUT sensor

| Symbol | Property | Value | Units | Reference(s) |
|-------------------|---------------------------------|-------|---------------|------------------------|
| ρ_{nickel} | Density of nickel | 8.9 | g/cm^3 | [55] |
| E_{nickel} | Modulus of elasticity of nickel | 205 | GPa | [59] |
| σ_{nickel} | Residual stress of nickel | -265 | GPa | Computed from C-V data |
| ν_{nickel} | Poisson's ratio of nickel | 0.31 | Dimensionless | [54] |

Table 6: Material properties of a diaphragm

The nickel cMUT sensor array consists of 12×14 elements with hexagonal pattern on a $1.01 \text{ cm} \times 1.01 \text{ cm}$ chip, as shown in Figure 36 (left). Every sensor is connected in parallel. There are 2 bonding pads along the bottom edge of the chip for electrical connection (Figure 36 (right)). Packaging uses a ceramic dual in-line (DIP) package to which the MEMS array is wirebonded.

Chapter 4

Modeling and Electronics Design

In this chapter, mathematical modeling of the devices is introduced. The first section shows the sensor modeling. The modeling of both chips (the PolyMUMPs® chip and the nickel-on-glass chip) is based on the lumped element modeling method. Due to their geometries and material properties, modeling approaches are slightly different. The second section discusses the electronic design of receivers and a transmitter.

4.1. Sensor Design

4.1.1. Lumped Element Modeling (LEM)

The membrane of a cMUT sensor vibrates with a 2 dimensional pattern, and acoustic pressure fields are 3 dimensional. Therefore, it is complex to analyze the behavior of the membrane. For efficient calculation, lumped element modeling is used instead of 3D coupled acoustic vibration modeling. LEM simplifies the behavior of the membrane to a single degree of freedom motion (Figure 39). For use of the valid LEM, there is an assumption that the wavelength of an acoustic wave must be much larger than the membrane diameter of the device.

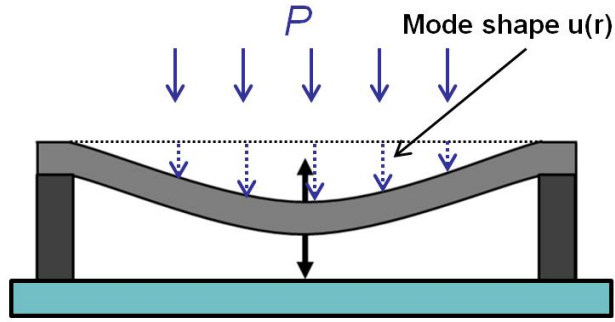


Figure 39: single degree of freedom (single mode) simplification of the diaphragm behavior using LEM

Equivalent circuit elements of LEM include the mechanical and acoustical elements of the cMUT sensor. There is a mathematical relationship between conjugate power variables in each energy domain. Table 7 and 8 shows conjugate power variables and elements in each energy domain.

| Energy Domain | Effort (f) | Flow (u) |
|---------------|-----------------------------------|--|
| Mechanical | <i>Force (N)</i> | <i>Velocity (m/s)</i> |
| Acoustical | <i>Pressure (N/m²)</i> | <i>Volume Velocity (m³/s)</i> |

Table 7: Conjugate power variables in Mechanical and Acoustical Domain.

LEM consists of various elements through which energy flows into the system. There are three linear components in each domain (a resistor, a capacitor, and an inductor). The system loses energy through the resistor, stores potential energy through the capacitor, and stores kinetic energy through the inductor. Table 8 shows lumped elements in each domain.

| Energy Domain | Resistance | Capacitance | Inductance |
|---------------|-----------------------|---------------|----------------|
| Mechanical | $R_m (N \cdot s/m)$ | $C_m (m/N)$ | $M_m (kg)$ |
| Acoustical | $R_a (N \cdot s/m^5)$ | $C_a (m^5/N)$ | $M_a (kg/m^4)$ |

Table 8: Lumped elements in mechanical and acoustical domain.

The relationship between the effort power variable and the flow variable using lumped elements and is shown in Table 9.

| Energy Domain | Resistance | Capacitance | Inductance |
|---------------|-------------|---------------------|---------------------|
| Mechanical | $f = R_m u$ | $u = j\omega C_m f$ | $f = j\omega M_m u$ |
| Acoustical | $f = R_a u$ | $u = j\omega C_a f$ | $f = j\omega M_a u$ |

Table 9: Relationship between conjugate power variables in each domain

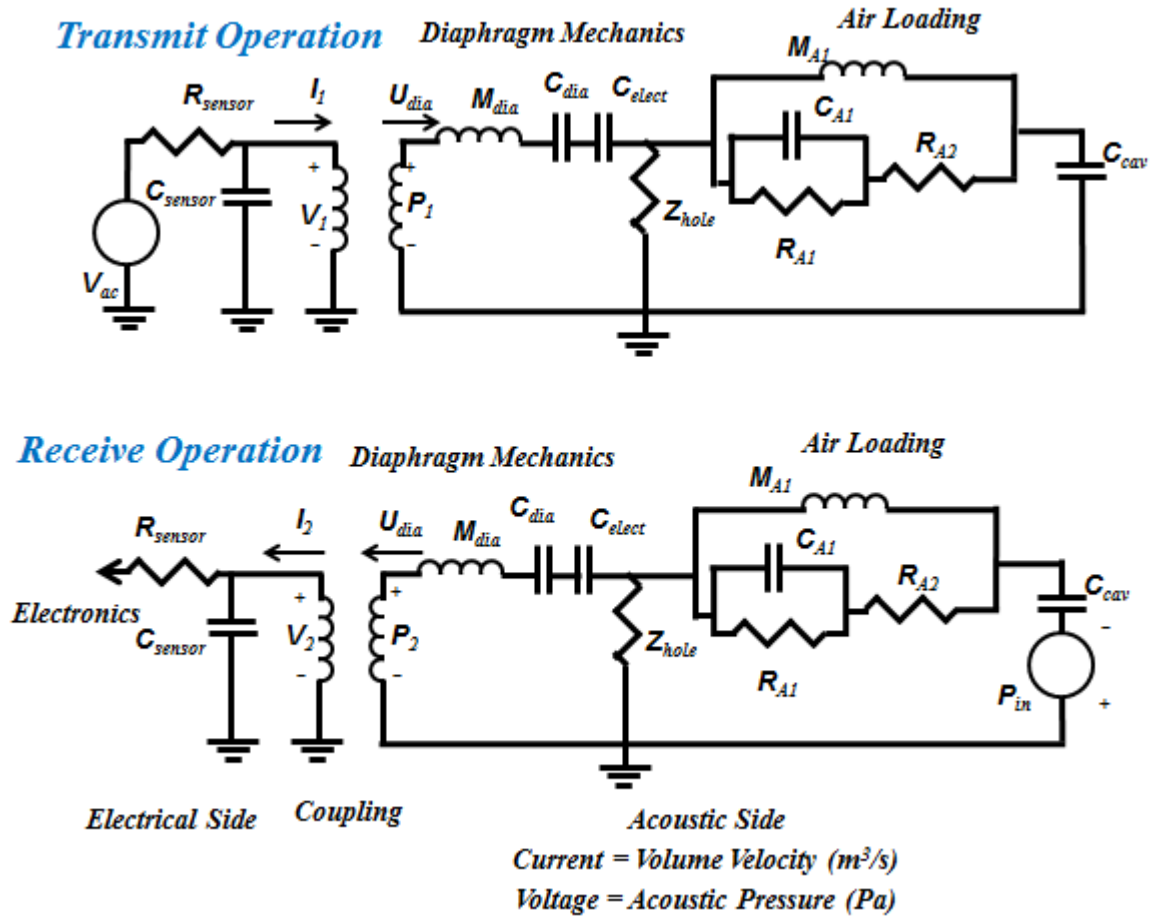


Figure 40: Coupled mechanical-electrical lumped element model.

Using these relationships, a LEM was developed for computational analysis of the transducer behavior [17, 60]. Figure 40 shows the LEM for both the mechanical and electrical equivalent circuitry. This circuitry includes the sub-elements of the model: external environmental loading, cMUT structure, electromechanical coupling, cavity compliance, and the negative electrostatic spring. The modeling procedure closely follows the methods described by Doody *et al.* [17]. The most significant difference from Doody's model is that this device has holes through the diaphragm to front vent the device.

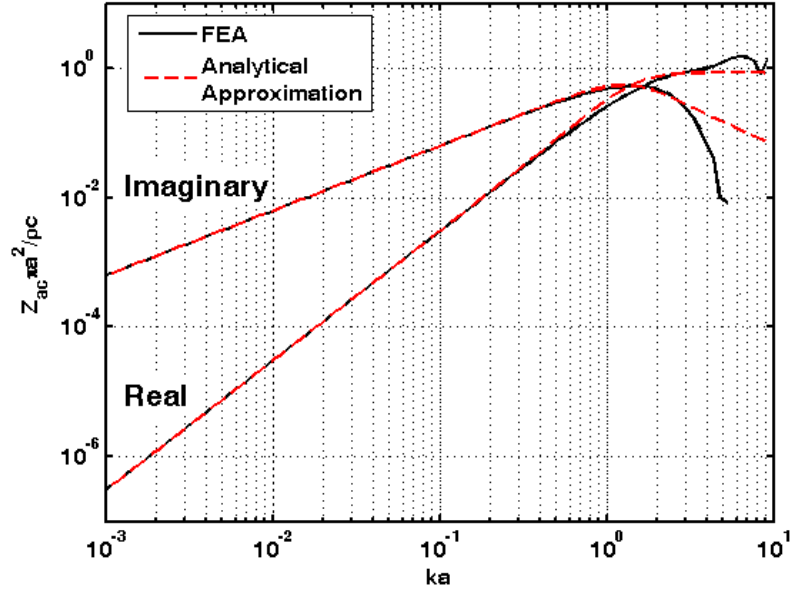


Figure 41: Comparison of finite-element and analytical approximation to the environmental loading presented in nondimensional form.

The environmental mass loading, Z_{env} , represents the acoustic radiation impedance of the vibrating diaphragm radiating into an infinite half-space. The model used in Figure 40 is similar to [17, 60] where the total environmental impedance is computed by integrating the surface pressure times displacement over area, and normalizing by the area integral of surface displacement squared. This formulation preserves power,

$$Z_{env} = \frac{\int u(r)P(r)dA}{\left(\int u(r)dA\right)^2} \quad (4.1)$$

$$R_{A1} = \frac{0.471\rho c}{\pi a^2} \quad (4.2)$$

$$R_{A2} = \frac{0.850\rho c}{\pi a^2} \quad (4.3)$$

$$M_{A1} = \frac{0.628\rho}{\pi a} \quad (4.4)$$

$$C_{A1} = \frac{2.016\pi a^3}{\rho c^2} \quad (4.5)$$

$$u(r) = \left[1 - \left(\frac{r}{a} \right)^2 \right]^2 \quad (4.6)$$

where $u(r)$ is the surface displacement of the diaphragm, $P(r)$ is the surface pressure, and Z_{env} is the effective environmental impedance, which can be modeled using the lumped elements as shown in Figure 40. R_{A1} is the low-frequency radiation resistance asymptote, R_{A2} is the high frequency radiation resistance asymptote, M_{A1} is the low-frequency reactance asymptote, and C_{A1} affects the transition region at high ka . ρ is the density of air, c is the speed of sound, and a is the radius of the diaphragm,. Following the work of Doody *et al.*[17], in order to determine the coefficients in front of each term, a computational model using finite element analysis (FEA) was used [17]. For the PolyMUMPs® chip, the FEA model computed the radiated acoustic pressure field transmitted into an infinite acoustic half-space by an axisymmetric baffled structure oscillating in a clamped static bending mode shape (Equation (4.6)). The effective environmental impedance is defined as Equation (4.1). By numerically matching the environmental impedance frequency response to the model of Figure 40, one arrives at the best expressions for the radiation impedance of an axisymmetric bending plate, given in Equations

(4.2-5). A comparison between the FEA and analytical approximation is shown in Figure 41. The approximate is valid for $ka < 3$.

For the nickel-on-glass chip, a simply supported bending mode shape was used for the FEA model.

$$u(r) = \frac{5+\nu}{1+\nu} - 2 \frac{3+\nu}{5+\nu} \left(\frac{r}{a}\right)^2 + \frac{1+\nu}{5+\nu} \left(\frac{r}{a}\right)^4 \quad (4-7)$$

Where, ν is the Poisson ratio of plated nickel.

Using the simply supported bending mode shape, the analytical approximation is

$$R_{A1} = \frac{0.243\rho c}{\pi a^2} \quad (4-8)$$

$$R_{A2} = \frac{\rho c}{\pi a^2} \quad (4-9)$$

$$M_{A1} = \frac{0.643\rho}{\pi a} \quad (4-10)$$

$$C_{A1} = \frac{5.52\pi a^3}{\rho c^2} \quad (4-11)$$

The impedance from the air flowing through the vent holes and the air flowing laterally in the cavity (known as squeeze film damping) from the vent holes, Z_{hole} , is shown in Figure 40. The impedance is calculated as the sum of two dominant resistances; the resistance for flow through the holes, which comes from the classical small pipe resistance and the squeeze film damping for a perforated plate, estimated using Skvor's formula, (S and C_f below) [60, 61]

$$Z_{hole} = R_{hole} + R_{squeeze} \quad (4.12)$$

$$R_{hole} = \frac{8\mu(t_{structure})}{n\pi a_{hole}^4} \quad (4.13)$$

$$R_{squeeze} = \frac{12\mu C_f}{n\pi t_{gap}^3} \quad (4.14)$$

$$C_f = \frac{S}{2} - \frac{S^2}{8 - 0.25 \ln(S) - 0.375} \quad (4.15)$$

$$S = \frac{\pi a^2}{C_c^2} \quad (4.16)$$

where μ is the viscosity of air, $t_{structure}$ is the total thickness of the diaphragm, n is the number of holes in the diaphragm, a_{hole} is the radius of the holes in the diaphragm, and C_c is the center-to-center spacing of holes in the diaphragm.

The cavity compliance represents the stiffness of the air in the backing cavity as it is compressed by the diaphragm during its deflection. At higher frequencies the stiffness of this backing cavity dominates the displacement of the membrane as well as yielding the first primary resonant peak in the system. C_{cav} is determined from the volume of the gap, V_{gap} divided by the product of the density of air, ρ , and the speed of sound, c , squared.

$$C_{cav} = \frac{V_{gap}}{\rho c^2} \quad (4.17)$$

$$Z_{cav} = \frac{1}{C_{cav}s} \quad (4.18)$$

The compliance of the diaphragm with the effective bending stiffness, and the effective mass of the diaphragm (for the first mode of the thin circular bending plate) are computed using classical thin laminate plate theory,

$$C_{dia} = \frac{\pi a^6}{16 \cdot 12} \frac{1}{D_{eff}} \quad (4.19)$$

$$D_{eff} = \sum_{i=1} \frac{E_i}{1-\nu_i^2} \left(\frac{t_i^3}{12} + t_i y_i^2 \right) \quad (4.20)$$

$$y_c = \frac{\sum_{i=1} z_i \left(\frac{E_i}{1-\nu_i^2} \right)}{\sum_{i=1} \frac{E_i}{1-\nu_i^2}} \quad (4.21)$$

$$y_i = z_i - y_c \quad (4.22)$$

$$M_{dia} = \frac{9 \left(\sum_{i=1} \rho_i t_i \right)}{5\pi a^2} \quad (4.23)$$

where i is the layer type for each layer, y_c is the position of the neutral axis with respect to the bottom of the laminate, y_i is the distance from the center of the i_{th} layer to the neutral axis, and z_i is the position of the center of the i_{th} layer with respect to the bottom of the laminate.

For the nickel-on-glass chip, residual stress, σ_{nickel} , is included for calculation of C_{dia} ,

$$C_{dia} = \frac{1}{\frac{1}{\frac{\pi a^6}{16 \cdot 12} D_{eff}} + \frac{1}{\frac{5\pi a^4 \cdot (\sigma_{nickel} t_{nickel})}{9 \cdot 2.4048^2}}} \quad (4.24)$$

The effective bending stiffness, and the effective mass of the diaphragm,

$$D_{eff} = \frac{E_{nickel}}{1 - \nu_{nickel}^2} \left(\frac{t_{nickel}^3}{12} \right) \quad (4.25)$$

$$M_{dia} = \frac{18(\rho_{nickel} t_{nickel})}{\pi a^4} \int_0^a u(r)^2 r dr \quad (4.26)$$

Where $u(r)$ is the simply supported bending mode shape from eq (4.7)

The coupling from the mechanical to electrical side via the ideal transformer is shown in equation (19-20) where P_l is the effective electrostatic pressure, V_l is the voltage across the electrodes, I_l is the current flow through the capacitor, and U_{dia} is the volume velocity of the diaphragm.

$$P_l = N \cdot V_l \quad (4.27)$$

$$I_l = N \cdot U_{dia} \quad (4.28)$$

The coupling factor N is [17]

$$N = \frac{V_{bias} \epsilon_0}{t_{gap}^2} \quad (4.29)$$

when operating in receive mode, where the cMUT array is held at a constant DC bias, V_{bias} . In transmit mode, the cMUT array is driven with a pure AC drive, and the coupling factor is [17]

$$N = \frac{V_{ac} \epsilon_0}{4t_{gap}^2} \quad (4.30)$$

where V_{ac} is the amplitude of the AC drive signal, and all signals in the linear LEM should now be at twice the drive frequency. This frequency doubling effect is caused by the quadratic nature of the electrostatic coupling.

The electrostatic spring compliance is, in receive mode,

$$C_{elect} = \frac{-t_{gap}^3}{V_{bias}^2 \epsilon_0} \quad (4.31)$$

and, in transmit mode with pure AC drive,

$$C_{elect} = \frac{-16t_{gap}^3}{V_{ac}^2 \epsilon_0} \quad (4.32)$$

$$Z_{dia} = M_{dia} s + \left(\frac{1}{C_{dia} s} + \frac{1}{C_{elect} s} \right) + R_{stray} N^2 \quad (4.33)$$

Modeling of the electrostatic coupling and the negative electrostatic spring follow the methods of Doody *et al.* [17]. Two LEMs of a single cMUT element were used, as can be seen in Figure 40. Summarizing above, the following equation represents the transmit dynamics.

$$H_1(s) = \frac{-(Z_{env} + Z_{cav} + Z_{hole})}{((Z_{hole} + Z_{dia})(Z_{env} + Z_{cav}) + Z_{hole} Z_{dia}) N} = \frac{U_{dia}(s)}{V_{ac}(s)} \quad (4.34)$$

The following equation represents the receiver dynamics.

$$H_2(s) = \frac{-Z_{hole}}{(Z_{hole} + Z_{dia})(Z_{env} + Z_{cav}) + Z_{hole} Z_{dia}} = \frac{U_{dia}(s)}{P_{in}(s)} \quad (4.35)$$

The top model shows the component in “transmit” mode. In this mode, the input voltage, V_{ac} , is driven to the sensor’s diaphragm. The output of this mode is the volume velocity, U_{dia} . It is possible to compute the pressure in the farfield from by summing the baffled monopole fields transmitting from all of the array elements,

$$P = j\rho f \cdot \sum_{m=1}^N \frac{1}{R_m} \cdot U_{dia} e^{-jkR_m} \quad (4.36)$$

where U_{dia} is the diaphragm volume velocity computed from the LEM of a single transducer, $k=\omega/c$ is the acoustic wavenumber, f is the transmit frequency in cycles/sec, ρ is the density of air, and R_m is the scalar distance from the center of the m^{th} array element to the field point. The summation is over the 64 array elements. Since all the elements are identical, all the U_{dia} are the same, and only the distance to the field point, R_m , changes. This transmit model neglects any acoustic coupling between the elements.

The bottom picture shows the component in “receive” mode. In “receive” mode, an acoustic pressure, P_{in} , is delivered from the environment, vibrating the diaphragm of the receiver. The output of the “receive” mode is the diaphragm volume velocity, which must be transformed into current flowing on the electrical side, which is integrated by the charge amplifier to produce the measured voltage output.

For calculation of output pressure, array modeling requires coupled computation. In the coupled computation, each element is influenced by the motion of all other elements in the array. Therefore, the coupled computation requires matrix modeling. For the array in “transmit” mode, the volume velocities of the elements in the array are represented by the following,

$$U_m = H_1 \cdot V_{ac} + \sum_n H_2 (1 - \delta_{mn}) P_{mn} \quad (4.37)$$

P_{mn} is the pressure field produced by the n_{th} element at the m_{th} element's centerpoint, and δ_{mn} is the kronecker delta function.

$$P_{mn} = \frac{\rho}{2\pi} \cdot \frac{s}{R_{mn}} \cdot e^{\frac{R_{mn}s}{c}} U_m \quad (4.38)$$

where R_{mn} is the distance between the m_{th} and n_{th} elements, s is the Laplace transform variable.

The farfield pressure can also be calculated in the transient case by summing the monopole fields from each element,

$$P = \sum \frac{\rho}{2\pi} \cdot \frac{s}{R_m} \cdot e^{\frac{R_ms}{c}} U_m \quad (4.39)$$

where R_m , is the radial distance from the m_{th} element to the field point.

For design of the devices, device performances are considered with the features of the devices based on LEM. Table 10 shows the relationship between geometric properties and the device performances. In all cases, the system is driven at the resonant frequency. The drive voltage is kept constant across cases. The geometry properties, as shown Table 3 and 5, were chosen in order to tune the resonant frequency, beamwidth, Q value, output pressure, and maximum drive voltage.

| | | Q value | Output pressure | Stiction risk | Resonant frequency | Beamwidth | Maximum drive voltage |
|--------------------|---|---------|-----------------|---------------|--------------------|-----------|-----------------------|
| Membrane diameter | ↑ | ↓ | ↓ | ↑ | ↓ | ↑ | ↓ |
| Membrane thickness | ↑ | ↑ | ↑ | ↓ | ↑ | ↓ | ↑ |
| Air gap thickness | ↑ | ↑ | ↓ | ↓ | ↓ | ↑ | ↑ |
| Vent hole diameter | ↑ | ↓ | ↓ | — | — | — | — |

Table 10: Relationship between geometric properties and device performances

4.2. Electronics Design

4.2.1. Receiver Electronics with PolyMUMPs® chip

For simple data acquisition from the cMUT sensors, the electronics on the receiver side was designed (Figure 42). The electronics consists of a charge amplifier and two stages of voltage amplifiers.

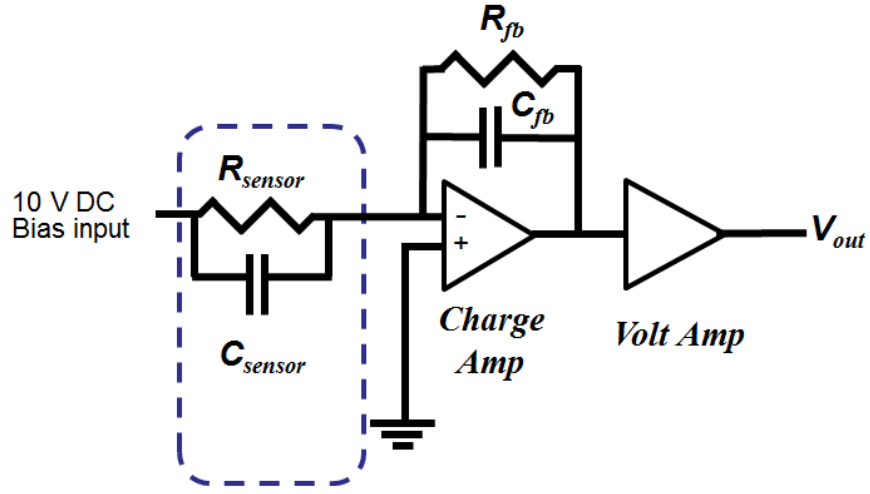


Figure 42: A simplified sensor model and electronics model of the receiver.

For property measurement of sensor (C_{sensor} and R_{sensor}), a sensor model was developed (Figure 42). To find the properties, prediction and experimental result were compared (Figure 43). According to the calculation, the PolyMUMPs® chip has capacitance of 4 nF and resistance of 50 M Ω , and the nickel-on-glass chip has capacitance of 65 pF and resistance of 200 M Ω .

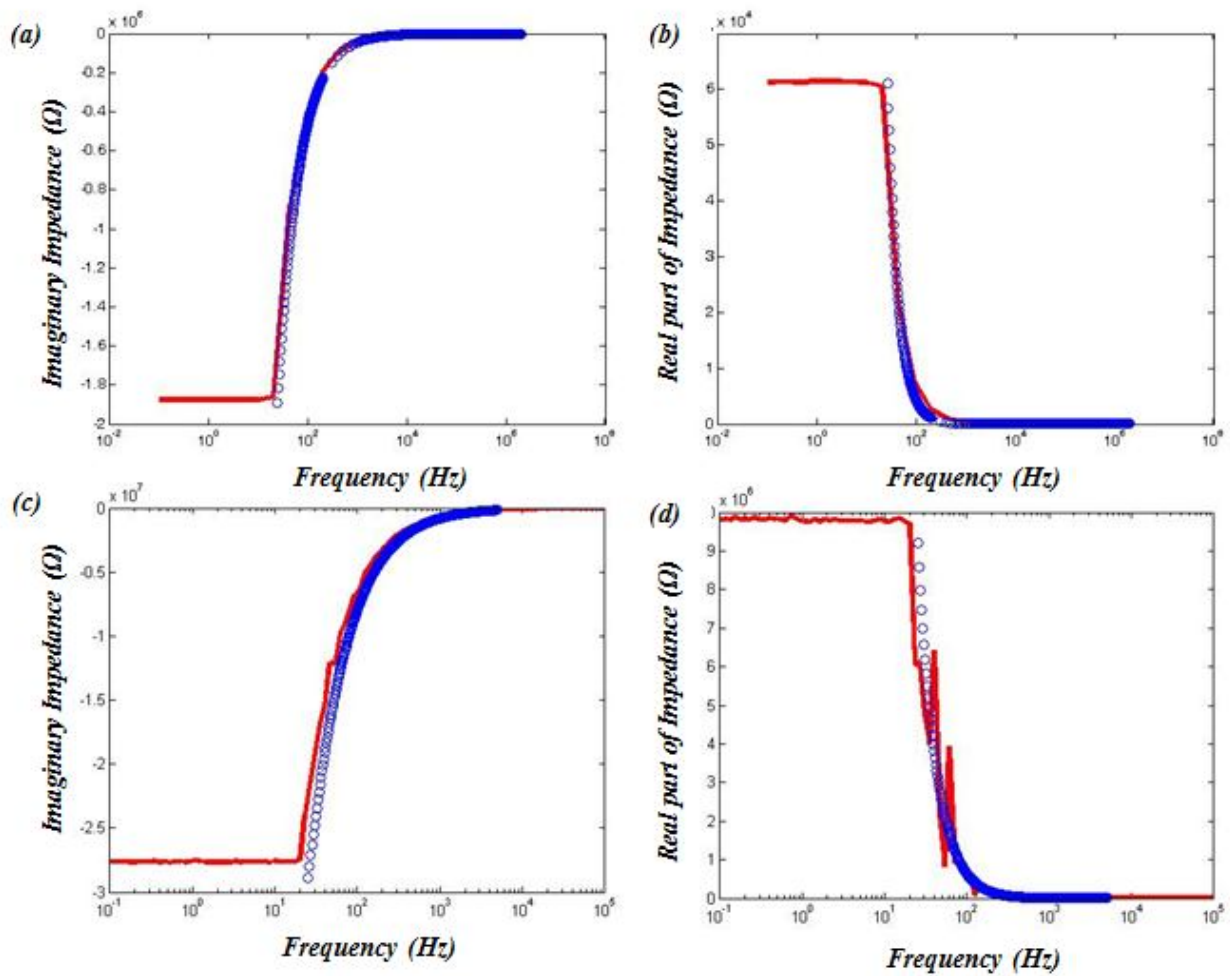


Figure 43: Comparison between impedance model and experimental result. (a-b) PolyMUMPs® results and (c-d) nickel-on-glass chips.

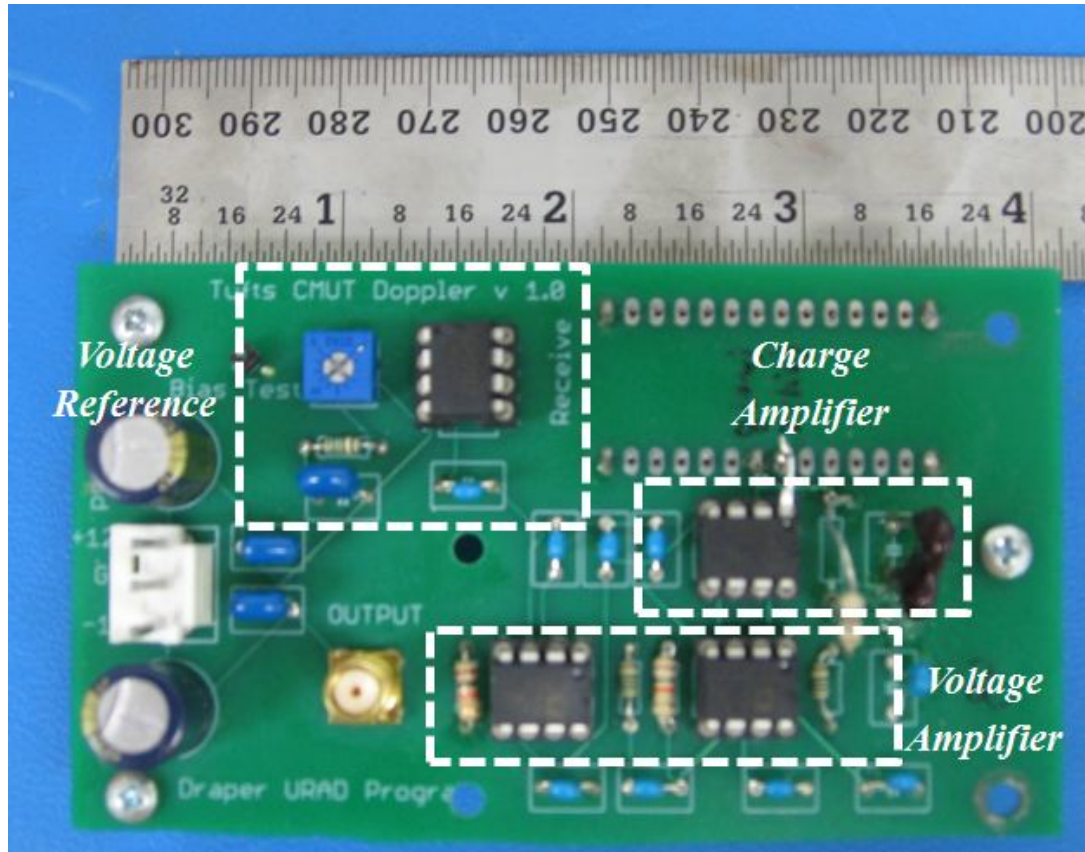


Figure 44: The receiver electronics including a voltage reference, a charge amplifier and voltage amplifiers.

The charge amplifier consists of a feedback capacitor C_{fb} and a feedback resistor R_{fb} , resulting in a high pass filter for the preamplifier stage with AD 8065 low noise operational amplifier [Analog Devices, Wilmington, MA]. Following the charge amplifier, the signal is passed into a series of two operational amplifier based inverting amplifier circuits with single pole high pass filters. The second and third amplifier stages are based on the OP 27 low noise operational amplifier [Analog Devices], each configured with a bandwidth of 2 kHz to 800 kHz. The low frequency cutoff is determined by discrete components in the high pass filter design, and the high frequency cutoff is set by the gain bandwidth product of the amplifier in

combination with the designed gain. Table 10 shows electronics components of the PolyMUMPs® chip. Figure 45 shows the transfer function of the electronics from the experiments.

| PolyMUMPs® chip | |
|-----------------|---------|
| <i>OP Amp</i> | AD 8065 |
| C_{fb} | 150 pF |
| R_{fb} | 10 MΩ |
| C_{sensor} | 4 nF |
| R_{sensor} | 50 MΩ |
| Gain | 40 dB |

Table 11: Electronics component of the PolyMUMPs® chip.

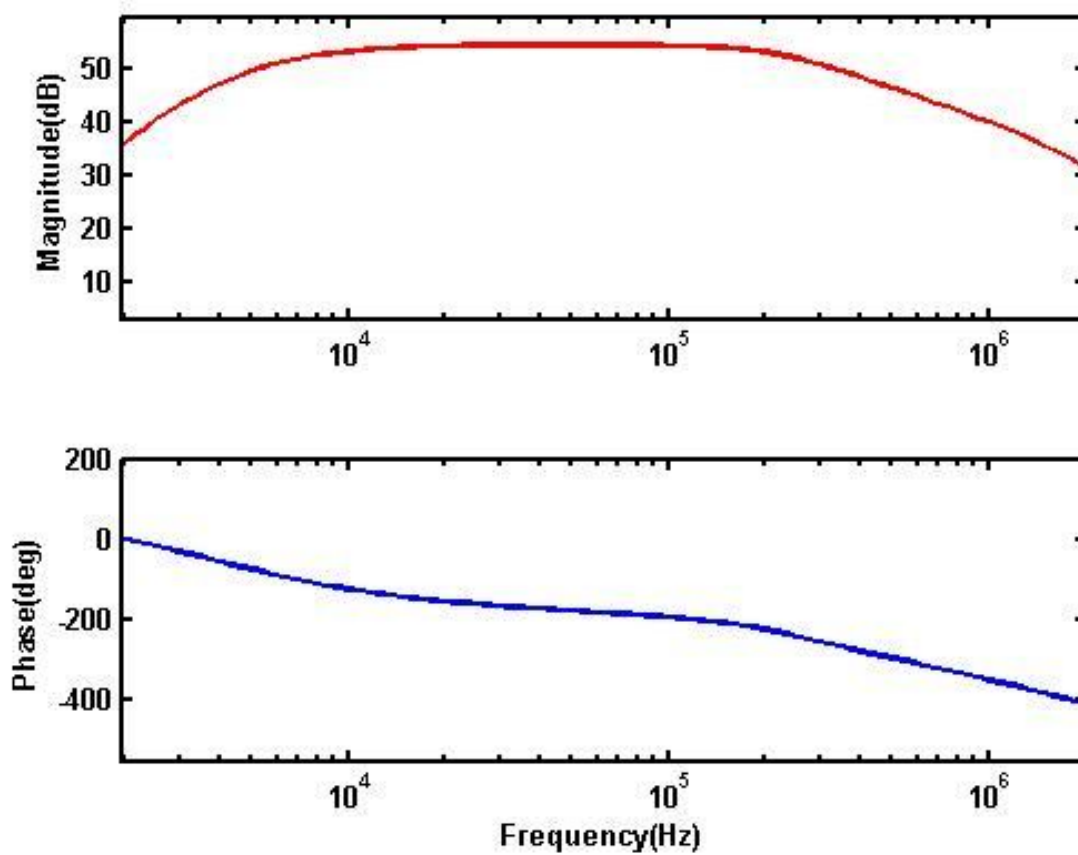


Figure 45: Transfer function of the receiver electronics from experiment.

4.2.2. Transmitter electronics with the nickel-on-glass chip

The nickel-on-glass chip has a higher snapdown voltage (290 V) than the PolyMUMPs® chip does (58 V) (Figure 46). The high snapdown voltage of the nickel-on-glass chip is due to the thicker structure and the thicker air gap. The high snapdown device can sustain a high input voltage swing on the transmitter, and a high DC bias voltage on the receiver.

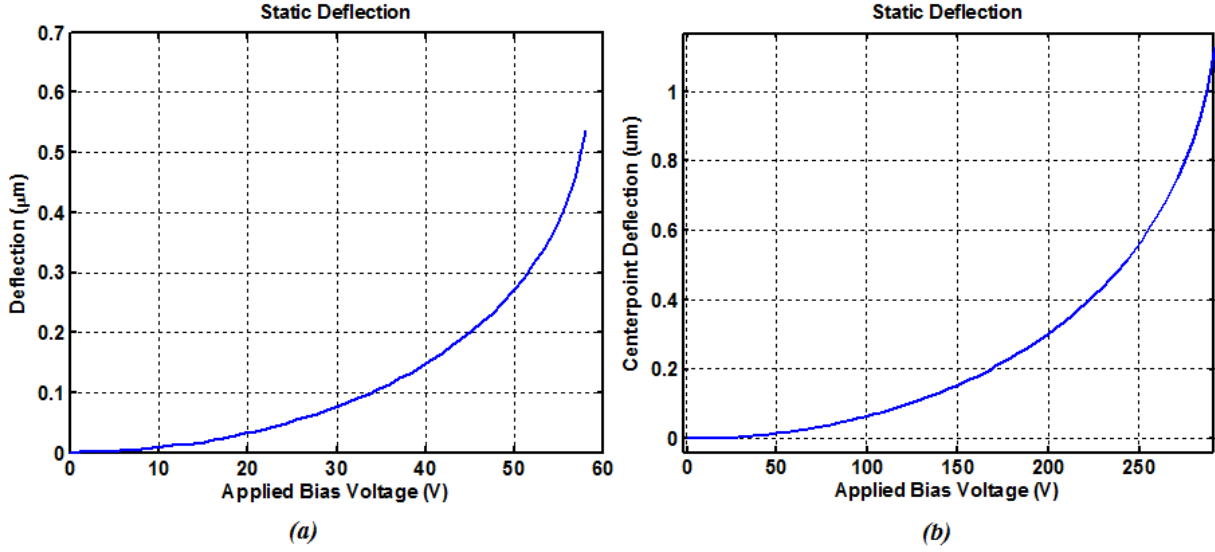


Figure 46: Predicted snapdown voltage comparison between (a) the PolyMUMPs® chip and (b) the nickel-on-glass chip.

For use of high voltage swing for the input, we need a gain stage for the transmitter because a general function generator is limited to 20 $V_{\text{peak-to-peak}}$. In the electronics, a voltage amplifier (OPA 445 high voltage FET-Input operational amplifier [Texas Instrument, Dallas, TX]) was used to increase the voltage swing across the cMUT to as much as 180 $V_{\text{peak-to-peak}}$ when operating on $\pm 45\text{V}$ supplies. This amplifier has a wide power supply range (10-45 V). Figure 47 shows the circuit. This is a bridge amplifier, allowing voltage swings twice as large as the power supply range through a differential drive scheme.

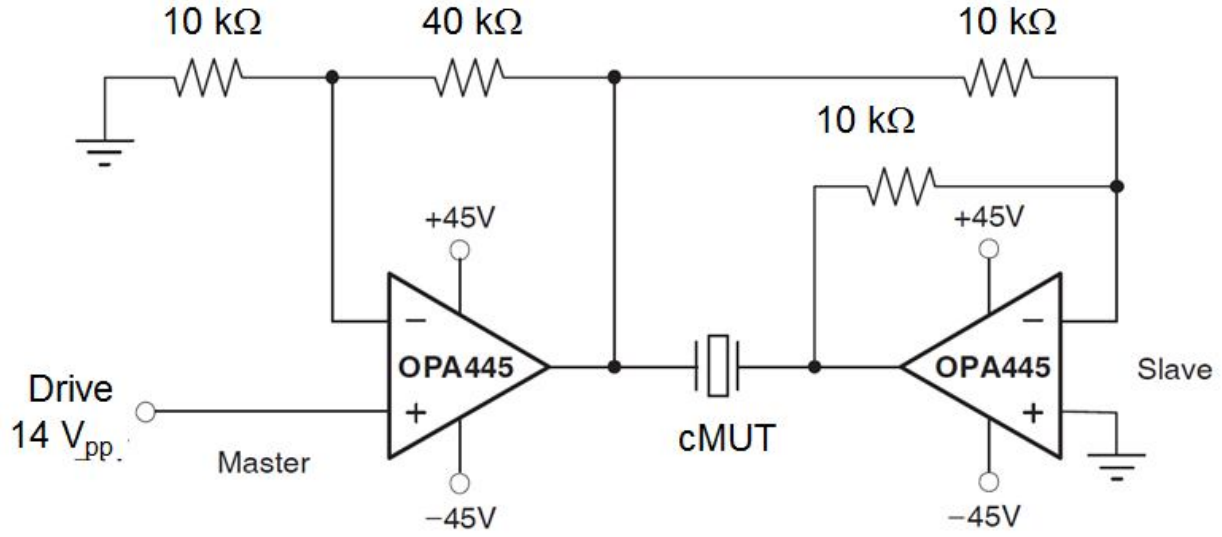


Figure 47: Bridge circuit with the cMUT chip. Modified from [62]

4.2.3. Receiver electronics with the nickel-on-glass chip

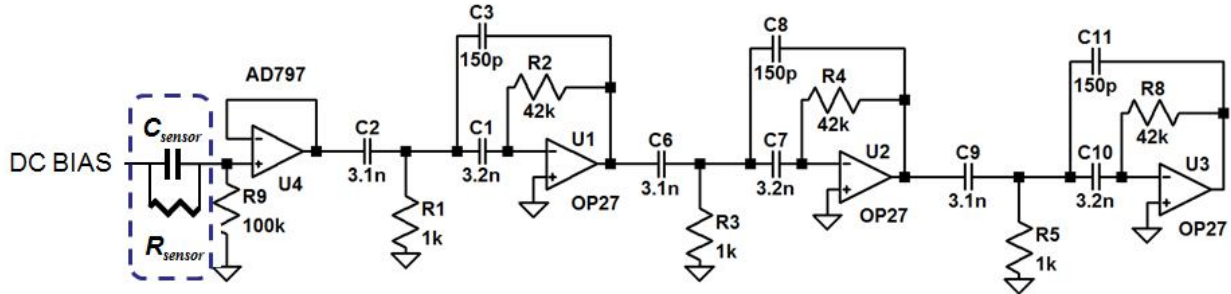


Figure 48: A simplified sensor model and electronics model of the receiver.

The voltage preamplifier consists of a sensor capacitance C_{sensor} and a sensor resistance R_{sensor} , resulting in a high pass filter (cutoff frequency: 27 kHz) for the voltage amplifier stage with AD 797 low noise operational amplifier [Analog Devices, Wilmington, MA]. Following the preamplifier, the signal is passed into a series of three operational amplifier based inverting

amplifier circuits with two pole high pass filters (cutoff frequency: 35 kHz). The voltage amplifier stages are based on the OP 27 low noise operational amplifier [Analog Devices], each configured with a bandwidth of 2 kHz to 800 kHz. Each stage has 26 dB of voltage gain. Table 11 shows the electronics components for the nickel-on-glass chip. Two kinds of DC bias (10 V and 90 V) can be provided, but in experiments, only 10 V DC bias was used because of a heating problem with 90 V DC bias.

| Nickel-on-glass chip | |
|----------------------|-----------------|
| <i>OP Amp</i> | AD 797, OP 27 |
| C_{sensor} | 65 pF |
| R_{sensor} | 200 M Ω |
| Gain | 26 dB per stage |

Table 12: Electronics component of the nickel-on-glass chip.

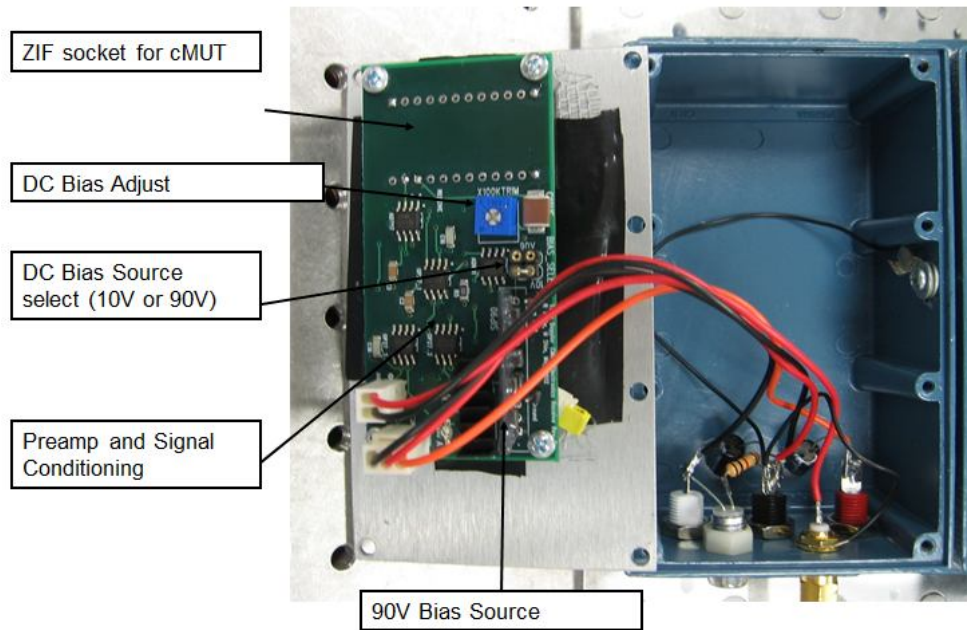


Figure 49: The receiver electronics for the nickel-on-glass chip.

Unlike the previous receiver electronics, the size of the electronics was dramatically reduced. The size of the sensor accounts for only 10% of the previous receiver electronics which consists of through-hole components. This electronics decreases the portability of the sensor system. Figure 49 shows components of the receiver electronics. The receiver electronics consists of a ZIF socket, a DC bias input, the preamplifier, and the voltage amplifiers. The receiver electronics is enclosed by a shielding box for protection from EMI.

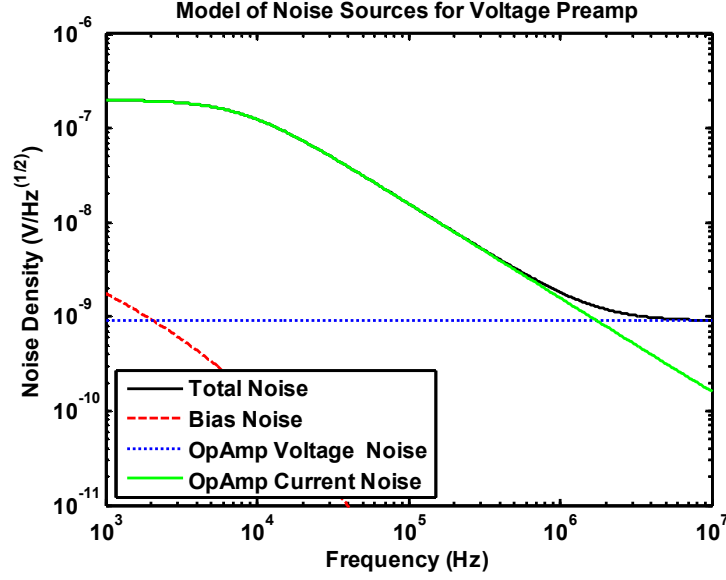


Figure 50: Predicted noise density of the receiver electronics with the nickel-on-glass chip.

An advantage of the nickel-on-glass chip is the low level of noise because of the low sensor capacitance C_{sensor} . To analyze this noise floor of the electronics with the cMUT sensor using the different sources of noise and the total noise in the system, the complex impedance method is used. Calculation of the impedance is the following.

$$Z_{sensor} = R_{stray} + \left(\frac{1}{R_p} + C_{sensor} \cdot j\omega \right)^{-1} \quad (4-40)$$

$$Z_2 = Z_{sensor} + \left(\frac{1}{R_1} + C_{filt} \cdot j\omega \right)^{-1} \quad (4-41)$$

$$V_{bias} = e_{bias} \left(\frac{R_2}{R_2 + Z_{sensor}} \right) \frac{\left(C_{filt} \cdot j\omega + \frac{1}{R_2 + Z_{sensor}} \right)^{-1}}{\left(R_1 + \left(C_{filt} \cdot j\omega + \frac{1}{Z_{sensor} + R_2} \right)^{-1} \right)} \quad (4-42)$$

$$V_{in} = \left(\frac{1}{R_2} + \frac{1}{Z_2} \right)^{-1} i_n \quad (4-43)$$

$$V_{total} = \sqrt{V_{bias}^2 + V_{en}^2 + V_{in}^2} \quad (4-44)$$

where R_{stray} is a stray capacitance of the sensor ($= 14 \Omega$), R_p is a parallel resistance of the sensor ($= 200 \text{ M}\Omega$), R_I is a bias resistance ($= 1 \text{ k}\Omega$), C_{filt} is a bias filter capacitance ($10 \mu\text{F}$), and V_{en} is voltage noise of the amplifier ($0.9 \text{ nV/Hz}^{0.5}$).

As shown in Figure 50, the low frequency is dominated by the current noise of the OP amplifiers up to 2 MHz. Figure 51 shows that the noise model is similar with measured noise.

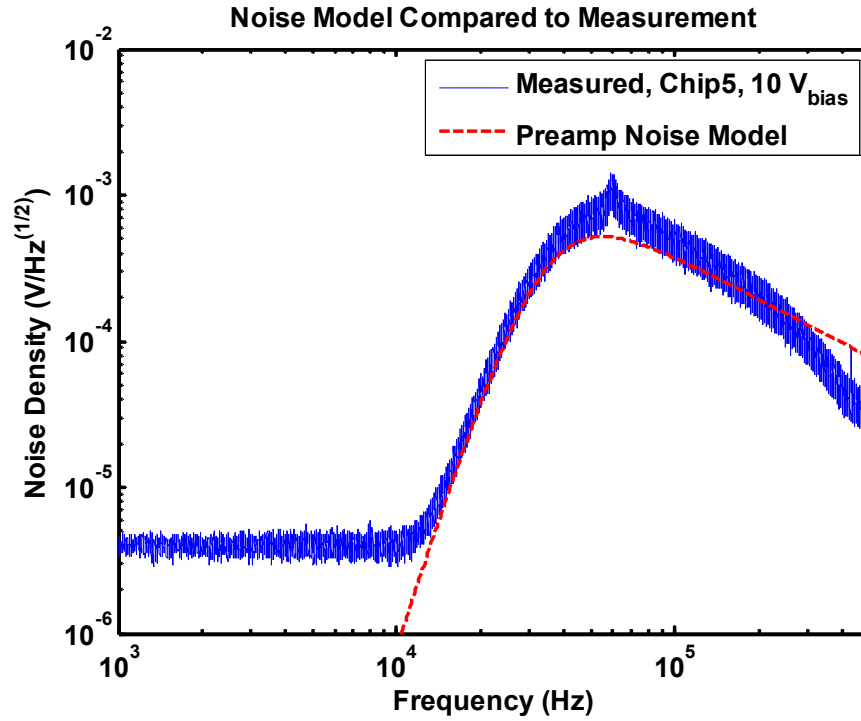


Figure 51: Comparison of noise density between the noise model and the experiment

Chapter 5

Experimental Result

This chapter discusses experimental results using the sensors and the electronics. Each chip shows LDV data, beampatterns, range tests, and velocity tests with a sled.

5.1. PolyMUMPs® Chip

To investigate the dynamic behavior of the sensor membranes, laser Doppler vibrometry (LDV) was used. An OFV 3001 vibrometer [Polytec, Waldbronn, Germany] was used for the LDV measurements (Figure 52). A laser spot was pointed on the center of each membrane and was controlled for automatic scanning using a LabVIEW® program and a universal motion controller [Newport, France]. The whole array was scanned with zigzag pattern (Figure 53). A diameter of the spot is 10 μm with a bandwidth of 20 MHz. A frequency sweep was driven using a signal generator, with an applied DC bias and AC voltage through the channel 0 (Figure 54). The vibratory displacement response of the cMUT sensor array was measured by LDV through the channel 1. A comparison between predicted frequency response results and measurement is shown in Figure 56. The magnitude is normalized to the product of the applied DC bias and AC bias during electrostatic drive. Measured frequency response by LDV is in excellent agreement with model predictions. As expected, the resonant frequency decreased to 185 kHz after a 1.5 μm gold layer was deposited by shadow masking. Before the deposition of Au, the resonant

frequency of the membrane is 430 kHz. The Q value is low (about 9) because of the etch holes. All 64 elements in the array were measured in this fashion. For the transmitter chip, the average value of the resonant frequency of 64 elements is 180.26 kHz and the standard deviation is 3.97 kHz, with 61/64 element yield. For the receiver chip, the average value of the resonant frequency of 64 elements is 193.74 kHz and the standard deviation is 3.69 kHz with 58/64 element yield (Figure 55).

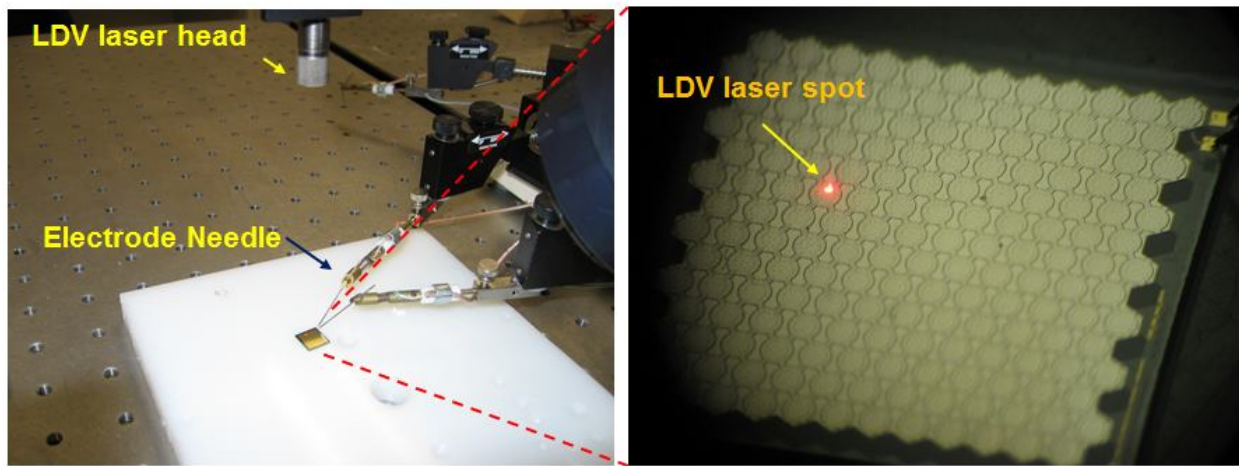


Figure 52: Experimental set-up with LDV and the chip.

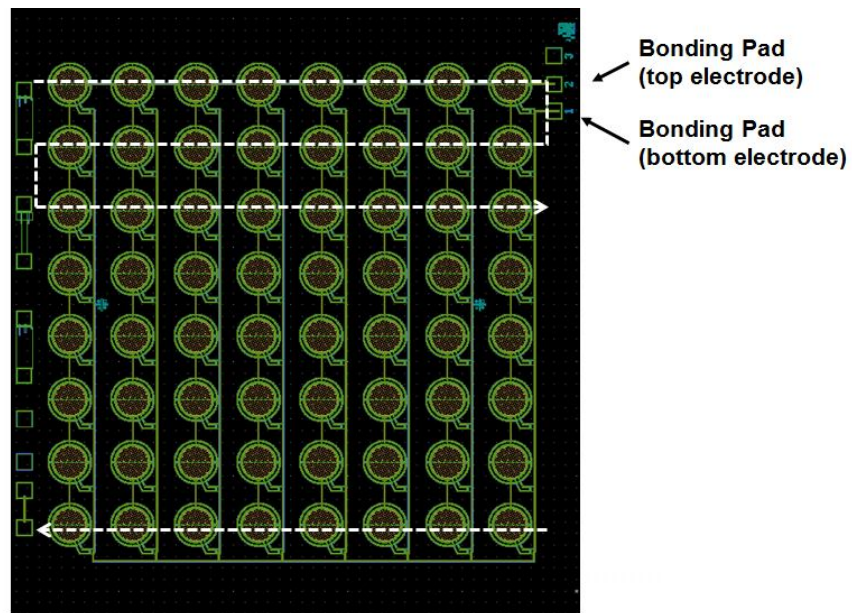


Figure 53: Automatic frequency sweep scanning using a LabVIEW program.

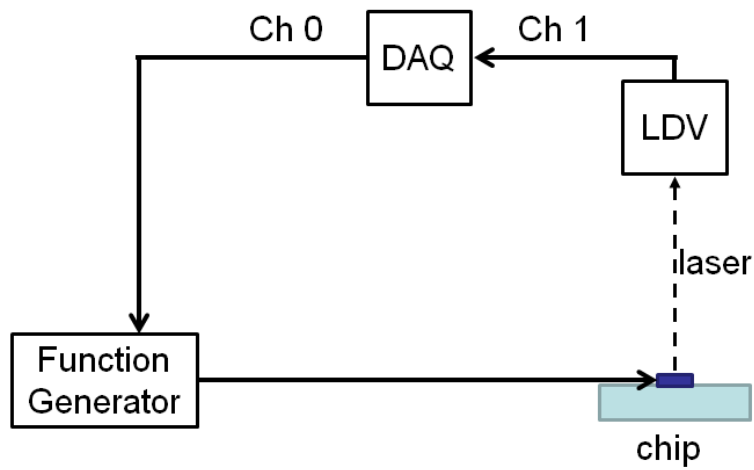


Figure 54: Experimental set-up diagram with LDV and the chip.

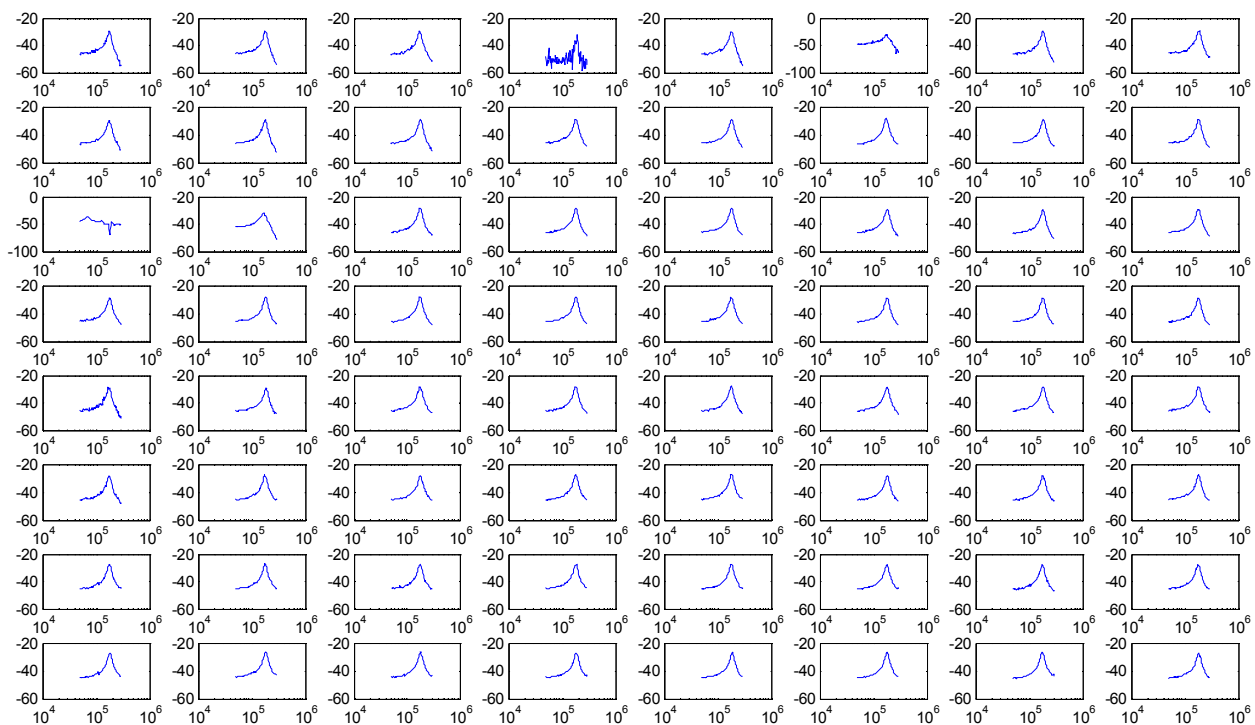


Figure 55: Frequency sweep scanning result for all 64 elements.

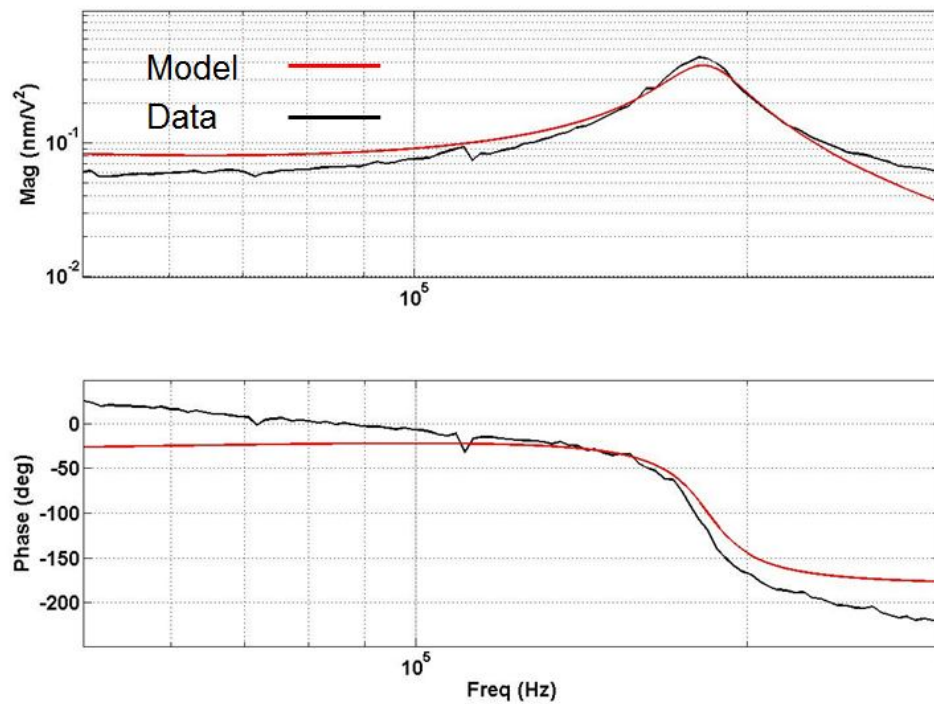


Figure 56: Predicted center point motion frequency response for a single element and the experimental result.

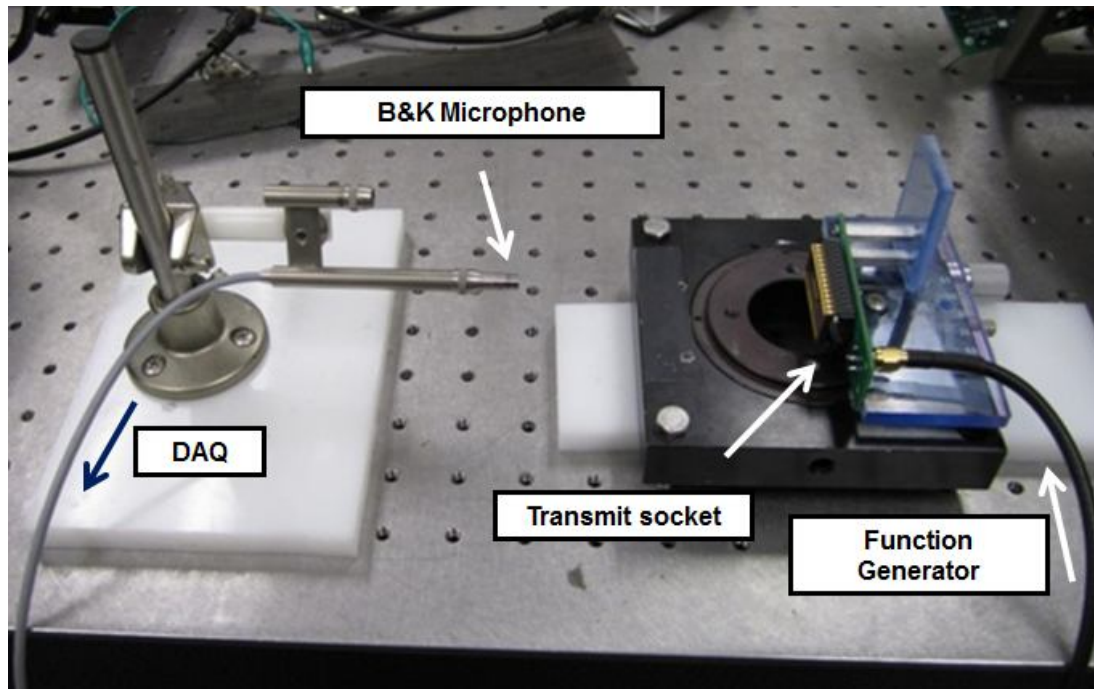


Figure 57: Acoustic transmit test set-up using cMUT Array (80 kHz).

A free field acoustic beampattern measurement was conducted for the array relative to a reference microphone. As shown in Figure 57, on the transmitter side (right side on the figure), a rotary positioner was used to measure beampattern, incrementally rotating the cMUT transmit chip about its center. The transmitted field amplitude was measured with a B&K ¼" free field microphone (left side on the figure). The measurement was conducted in continuous wave operation at 80 kHz. This test was run below the designed operating frequency of the cMUT (185 kHz) because the B&K cannot measure above 100 kHz. Results show a beampattern very similar to model predictions. Beampattern was measured at 10 cm from source (in the farfield of the array, but still within the direct field), using 20 V_{peak-to-peak} drive at 40 kHz (Frequency doubling due to the electrostatic drive produces acoustics at 80 kHz from a 40 kHz drive signal). The measured response is 40 dB SPL at 10 cm on axis (This is relative 20 µPa) (Figure 58).

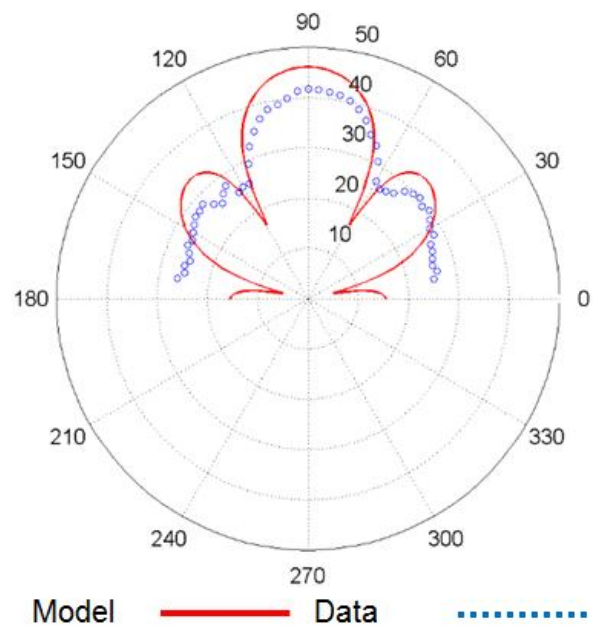


Figure 58: Acoustic transmit test result with beampattern. Beampattern is in units of dB SPL.

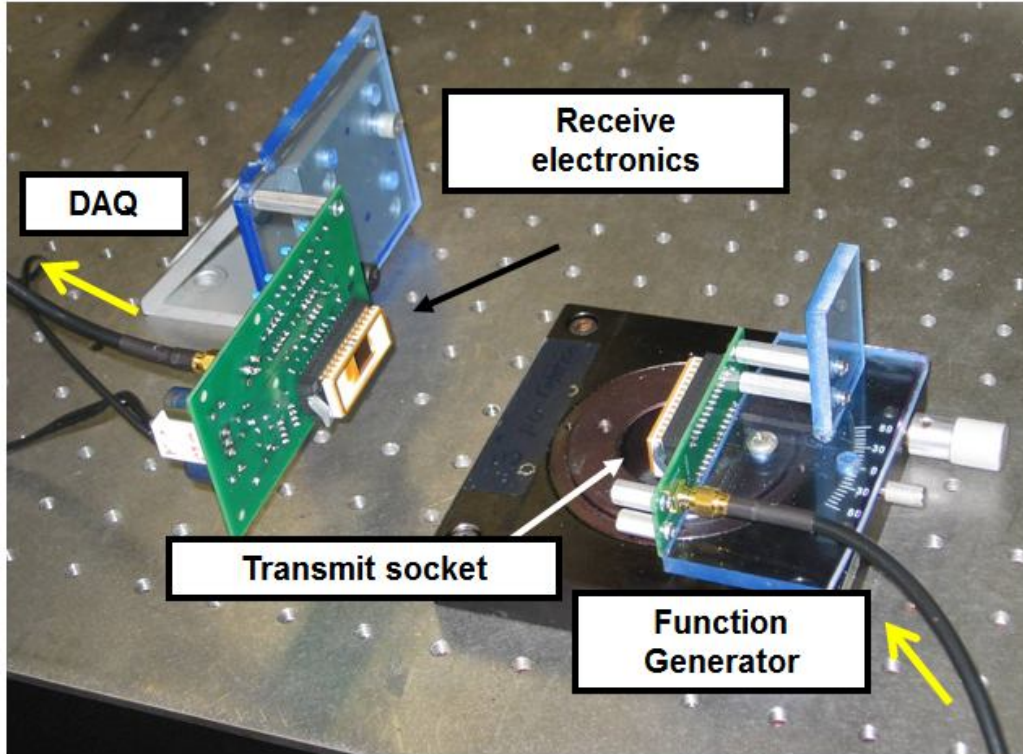


Figure 59: Acoustic transmit & receive test set-up using cMUT Array (185 kHz).

A second free field measurement was conducted using a pair of cMUT chips. The transmitter produced an acoustic signal at 185 kHz. It was driven electrically at 92.5 kHz drive at 20 V_{peak-to-peak}. Again, frequency doubling due to square law electrostatics gave acoustics at 185 kHz. This has the advantage of reducing electromagnetic interference from RF transmission. The transmitter was on the rotary positioner in Figure 59 (right side on the figure). The DC bias on the receiver was 10 V. The transducer arrays were 10 cm apart. The measured response was 0.6 mV_{rms} (55 dB re 1 mV_{rms}) at peak, which compares very well to the predicted 0.7 mV_{rms} from the computational model as shown in Figure 60. The -3 dB beamwidth is as expected at 13

degrees (6.5 degrees on either side of center). The side lobes are down by 15 dB compared to the main lobe.

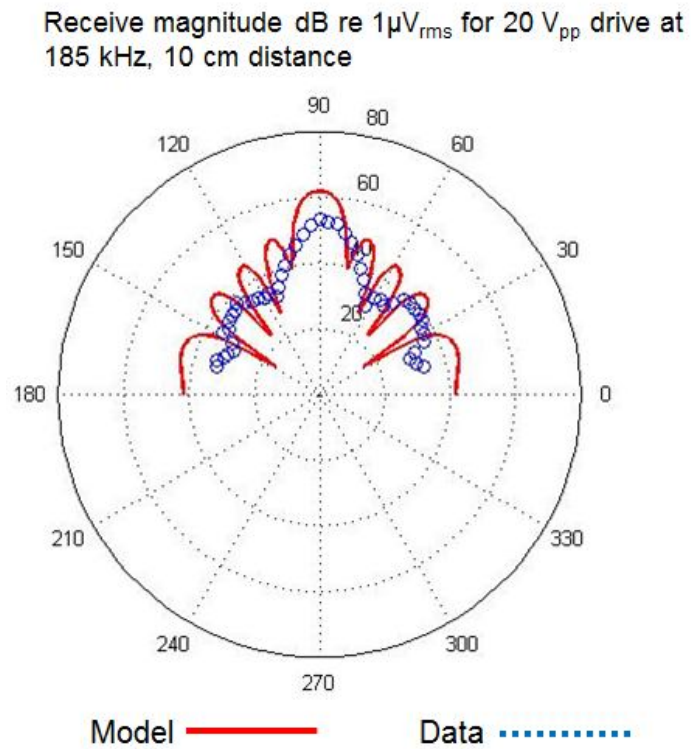


Figure 60: Beampattern of acoustic transmit & receive test with cMUT array.

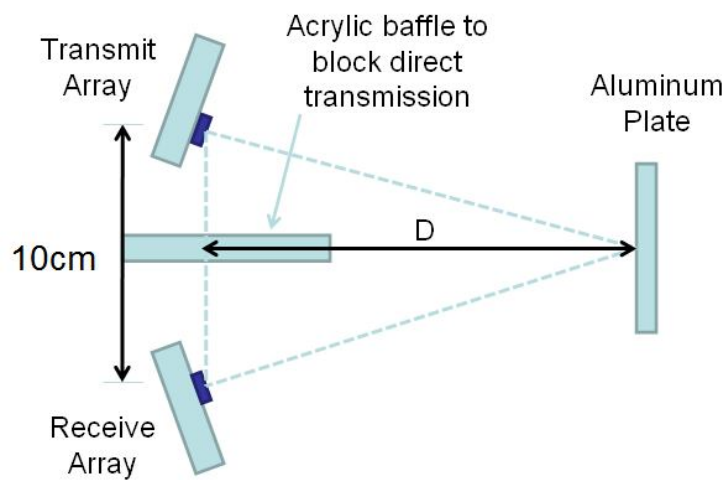


Figure 61: Reflection test set-up using cMUT array.

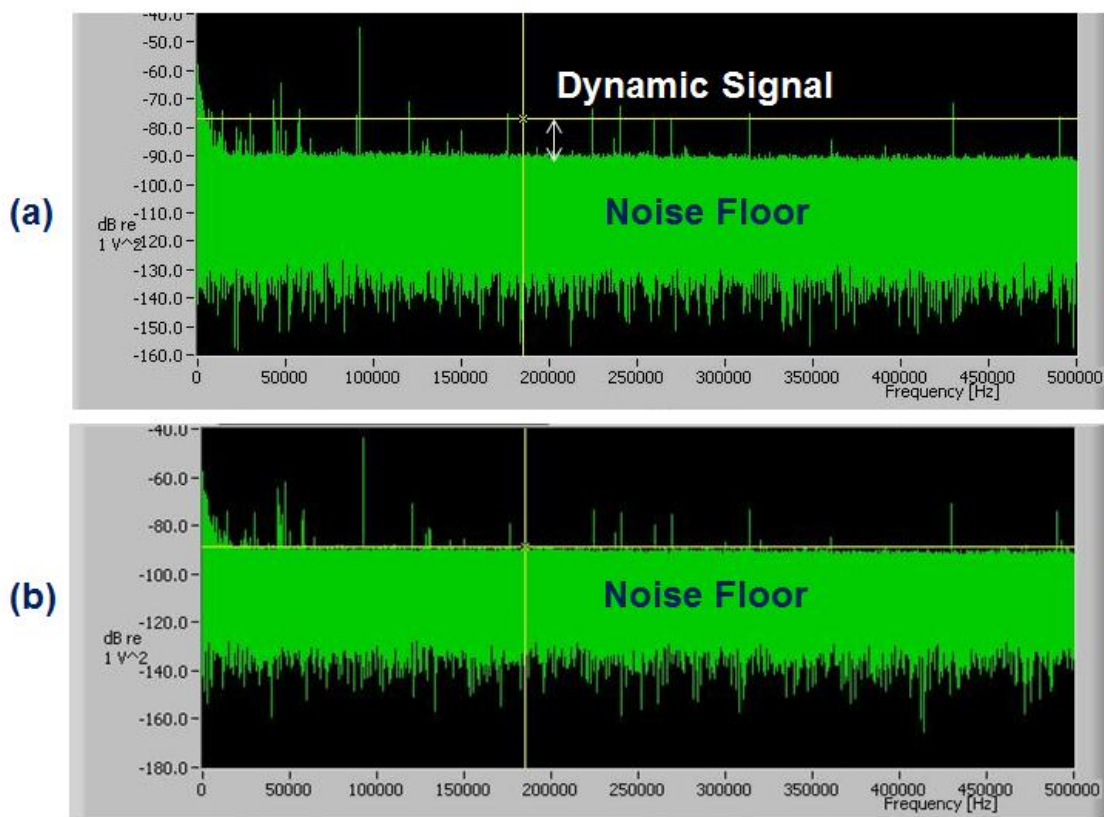


Figure 62: The change of the dynamic signal when D increases. (a) D=10.2 cm, (b) D=30.5 cm

To investigate the achievable range of a reflected acoustic wave, range testing with a reflecting boundary was conducted, as shown in Figure 61. During range testing experiments, the angle of the transducers was adjusted at each distance D in order to maximize the return signal. The lateral distance between the array chips was 10 cm. There was an acrylic plate in between the arrays to prevent direct transmission between the chips. As in the previous experiment, the drive signal was 20 V_{pp} at 92.5 kHz, and the DC bias on the receiver side was 10V. A dynamic signal that exists above the noise floor, decreases as the range D increases. Experimental results for reflected acoustic continuous wave transmit and receive using two chips reflecting off a flat aluminum plate show a maximum range of 60 cm (30 cm out and 30 cm back) as shown Figure 63. Signal power decreases with the square of D as expected. With $D \geq 30$ cm, the signal decreases below the noise floor (-91 dBV_{rms}). Noise is always dependent on sampling. In this experiment, the sampling frequency was $F_s = 1$ MHz and the number of samples was 2^{22} , resulting in a total data acquisition time of 4.2 seconds per point. The resulting noise bandwidth is 0.24 Hz.

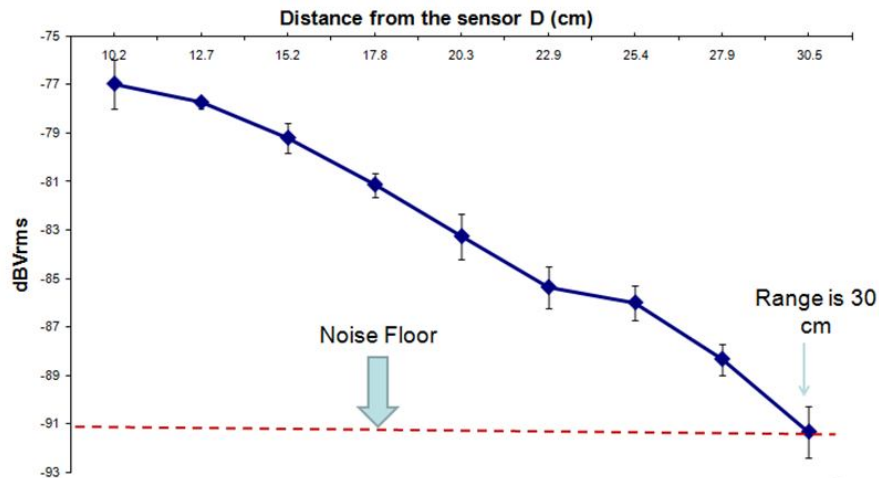


Figure 63: Range test result. The sensor signal is in dBV_{rms} in a 0.24 Hz band (4.2 second averaging time).

The system noise is dominated by the voltage noise of the preamplifier chip. A high speed operational amplifier, the AD8065 [Analog Devices, Wilmington, MA], was used to reduce the system noise as much as possible. Voltage noise dominates current noise, bias noise, and thermal noise for this particular system, thus the noise density at the system output can be estimated from the preamplifier voltage noise amplified by the preamplifier gain and second and third stage gains, assuming that we are in the passband of all amplifiers,

$$e_{noise} = e_n \left| 1 - \frac{C_s}{C_{fb}} \right| G_1 G_2 \quad (5-1)$$

where $e_n = 7 \text{ nV}/\sqrt{\text{Hz}}$ is the AD8065 voltage noise density, $C_s = 4 \text{ nF}$ is the sensor capacitance, $C_{fb} = 150 \text{ pF}$ is the feedback capacitance of the preamp, and $G_1 = G_2 = 10$ are the passband gains of the second and third stage amplifiers. This simple model results in an estimated noise floor of $18 \text{ } \mu\text{V}/\sqrt{\text{Hz}}$ at the system output, similar to the measured $60 \text{ } \mu\text{V}/\sqrt{\text{Hz}}$ noise.

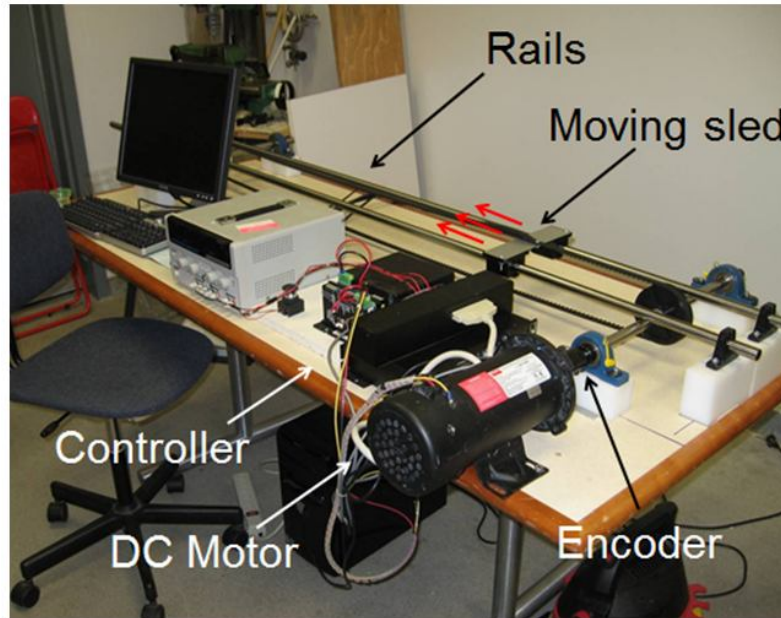


Figure 64: Experimental set-up for the velocity test.

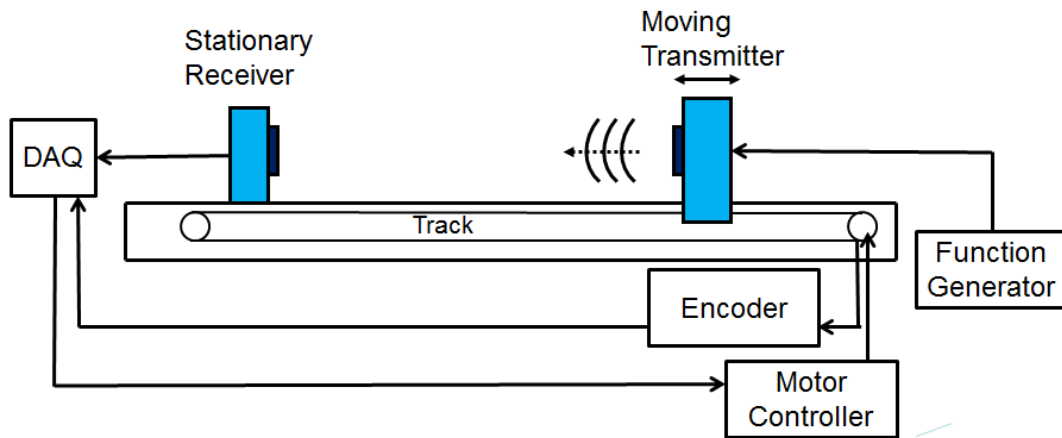


Figure 65: Schematic of a set-up for the velocity test.

Finally, a velocity sled was constructed and used to demonstrate measureable Doppler shifts at velocities from 0.2 m/s to 0.8 m/s. The velocity test setup consists of a speed controller, a DC motor, an encoder, and a moving sled, as shown in Figure 64. Figure 65 shows a schematic of a set-up for velocity test. The transmitter faces the receiver. The tests were conducted with one transducer moving and the receiver stationary, so no reflections were needed; this improved the signal to noise ratio. The continuous acoustic wave at 185 kHz was sent from the transmitter while the sled accelerated up to speed and then back to zero. The controller controls the velocity and distance of the sled, communicating with the DC motor. The test was operated for 1s. The sled moves for 0.5s with the specific velocity and stops for 0.5s, with acceleration and deceleration period in between. Figure 66 shows the Doppler shift using a spectrogram as time runs for a particular speed (0.4 m/s), and a sketch of the velocity profile. A Doppler shift is clearly seen. There is some spread of velocities, particularly during the motion, due to the fluctuation of the sled velocity. When the sled stops, because of some overshoot, the frequency band drops below 185 kHz.

Figure 67 shows similar spectrograms as the maximum velocity of the sled changes between 0.2 m/s and 0.8 m/s. To show the trend of the Doppler shift, ‘*ad hoc*’ profiles are included in the figures. The velocity profile from the cMUTs while the sled moves, approaches the expected velocity (red dotted lines). The Doppler shift increases as the velocity of the sled increases. Greater variability and overshoot is also seen at the higher velocities, probably due to higher variability in real sled velocity. Data was captured at $F_s=0.5$ MHz, and sampling points $N=500000$. The spectrogram uses a 2^{17} point window (Hamming window) with 62% overlap. The time window 0.262 sec, thus $\Delta f=3.814$ Hz was used.

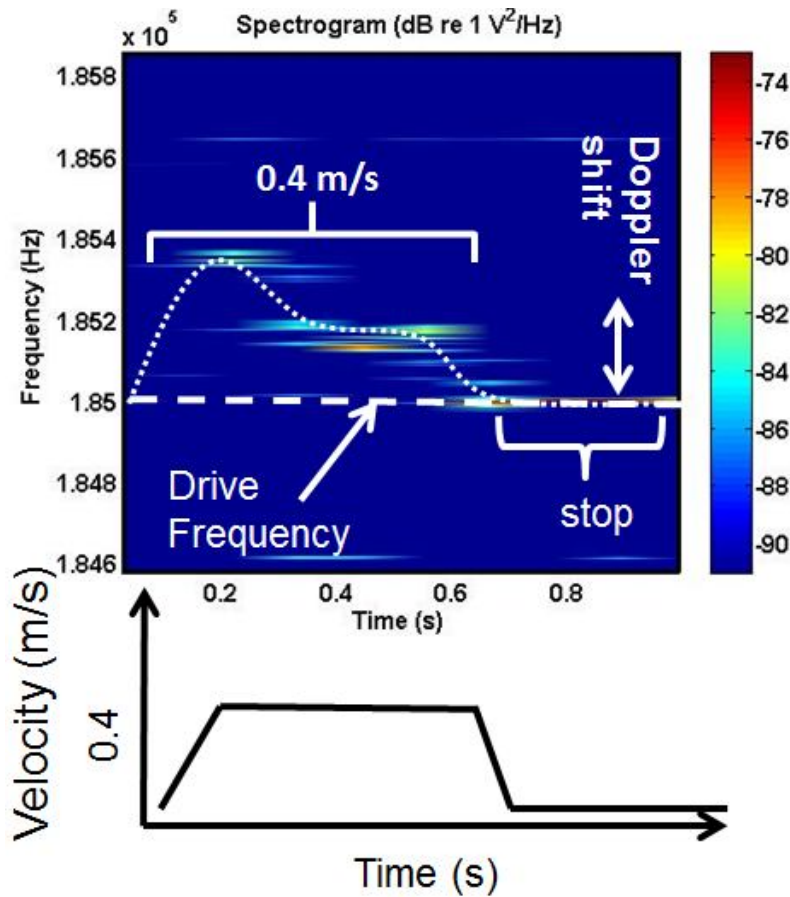


Figure 66: Spectrogram after the velocity test and an experimental concept.

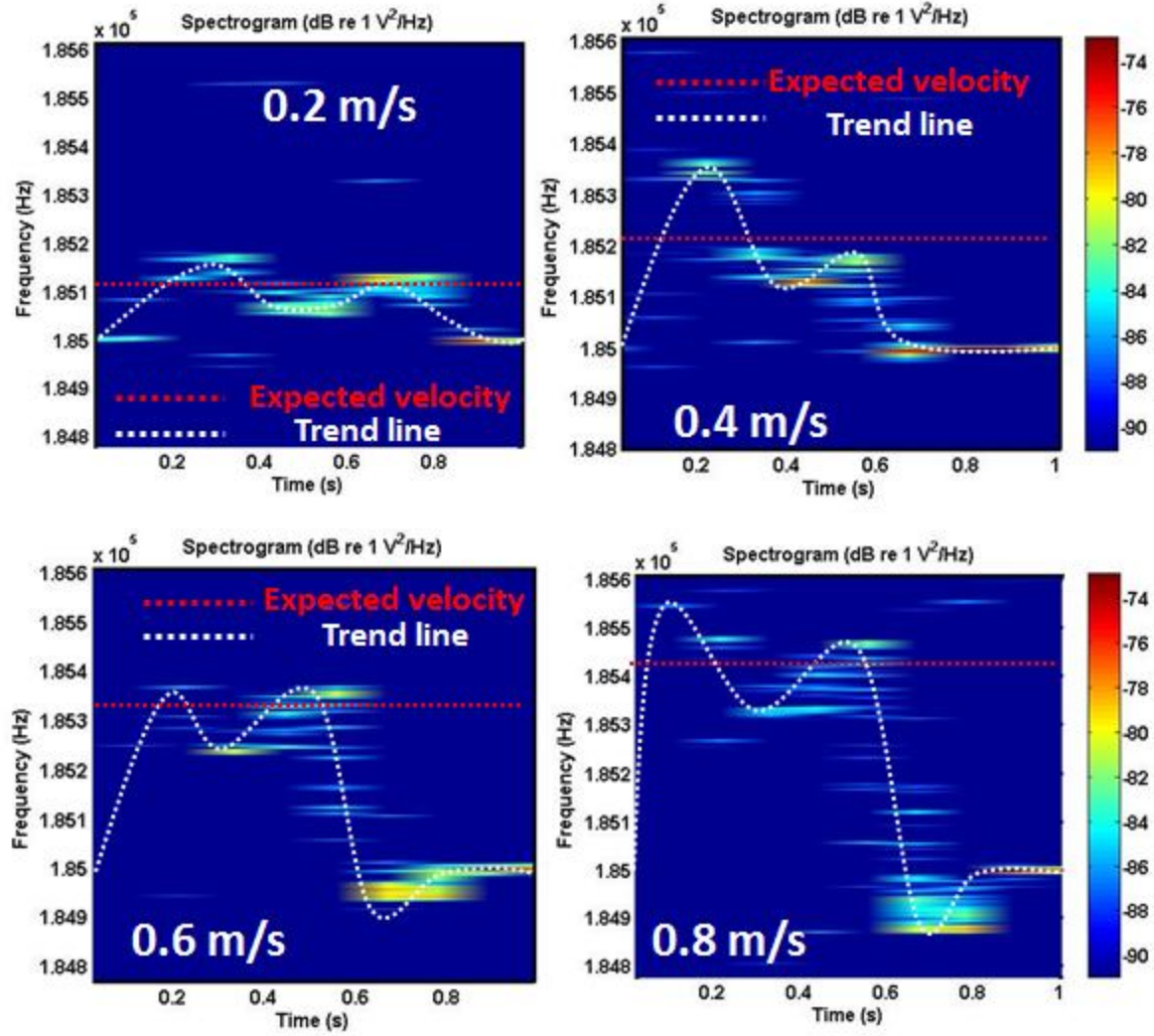


Figure 67: Spectrograms of the shifted frequency during different velocity tests.

5.2. Nickel-on-glass Chip

On the nickel-on-glass chips, the first test conducted was a DC bias voltage vs static capacitance test. In this test, a DC bias is driven between the electrodes and the membrane is pulled down

toward the bottom electrode by the electrostatic force. The membrane moves until the electrostatic force reaches equilibrium with the internal force of the membrane.

Since the force is proportional to the square of voltage, the bias voltage vs capacitance has quadratic relationship. Figure 68 shows this behavior correctly. The capacitance was measured with a precision LCR meter, E4980 [Agilent Technologies, Santa Clara, CA] and was performed with a bias voltage sweep between -40 V to 40 V. Importantly, this data can be used to determine residual stress in the nickel, which impacts the membrane compliance. By changing stress in the model, we are able to determine that the stress is -265 MPa (265 MPa compressive) to achieve a good fit to the measured CV data, as shown in Figure 68. The model is the same LEM described in chapter 4, but is at DC, so only compliance is important. The nonlinear relationships for N and C_{elect} must be included.

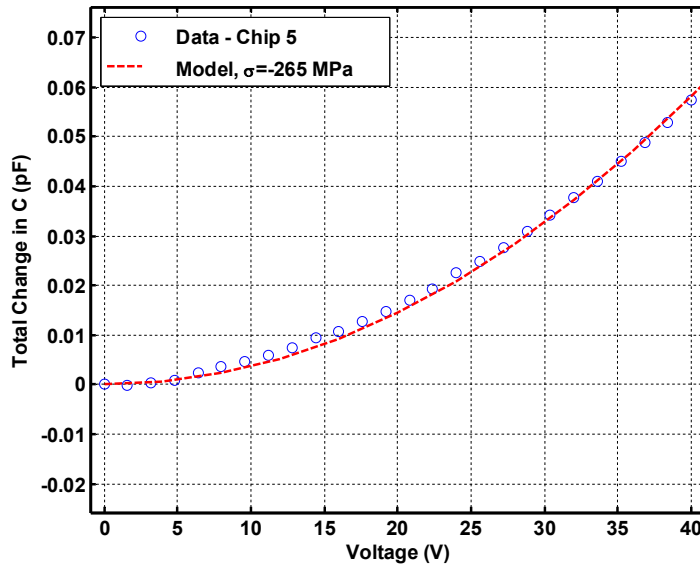


Figure 68: Predicted voltage-capacitance model and the experimental result.

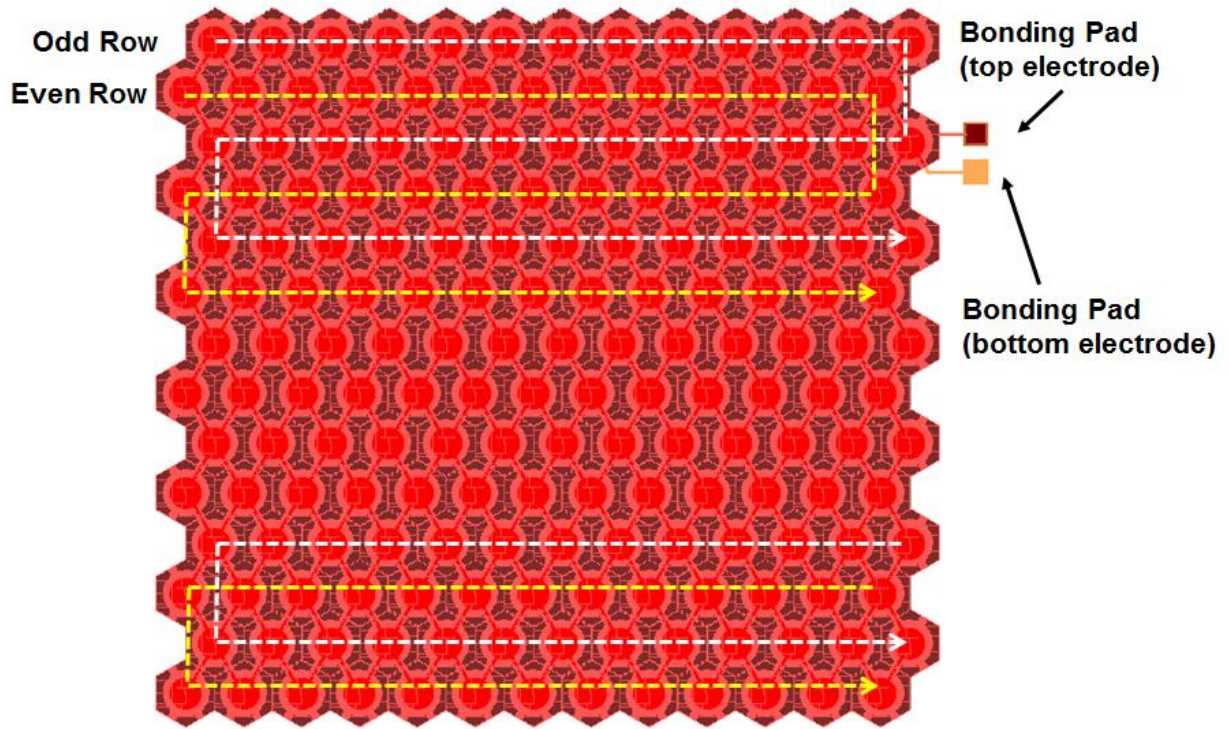


Figure 69: Automatic frequency sweep scanning using a LabVIEW program.

To investigate the dynamic behavior of the sensor membranes, laser Doppler vibrometry (LDV) was used. A laser spot was pointed on the center of each membrane. The whole array was scanned with a zigzag pattern twice with even rows and odd rows (Figure 69). A frequency sweep was driven using a signal generator, with an applied DC bias (5 V) and AC voltage (5 V). The vibratory displacement response of the cMUT sensor array was measured by LDV.

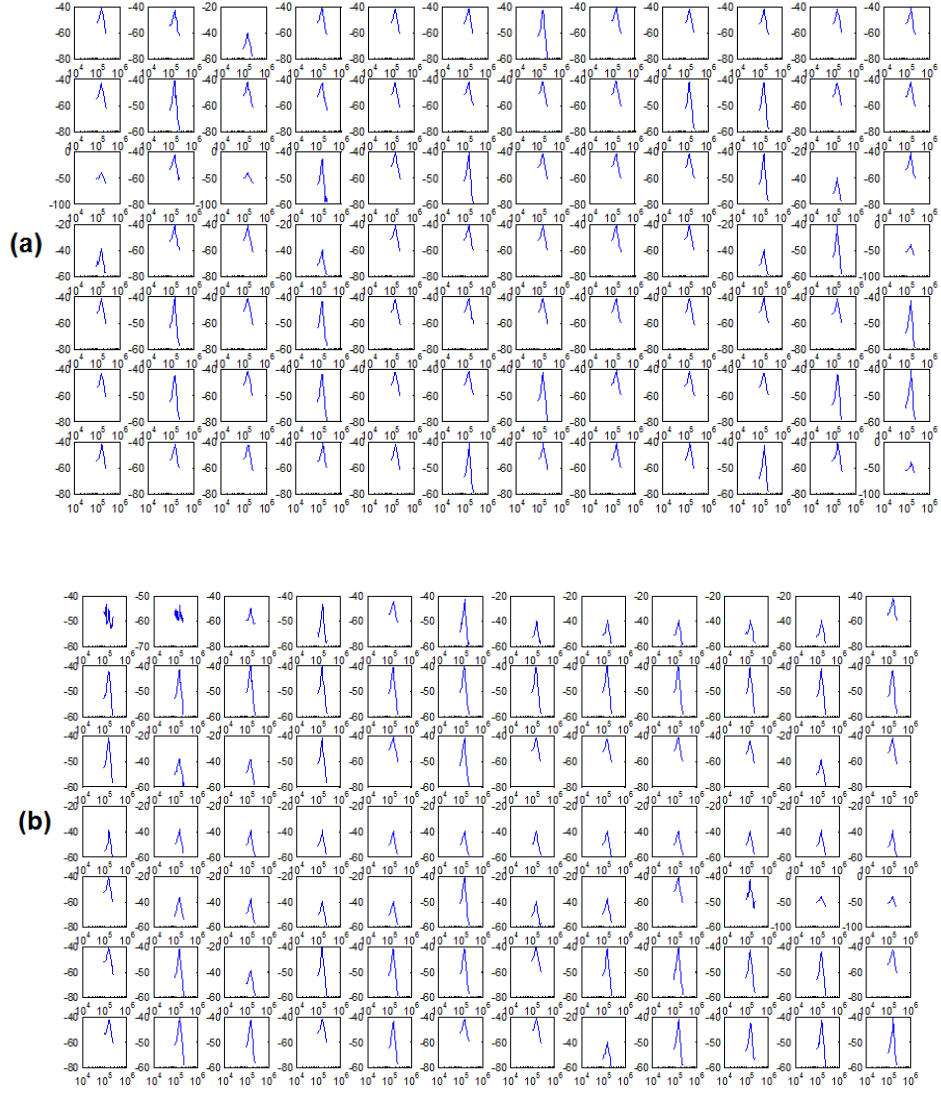


Figure 70: Frequency sweep scanning result for all 168 elements. (a) The odd row and (b) the even row.

As expected, the resonant frequency was between 155-185 kHz. All 168 elements in the array were measured in this fashion. For the transmitter chip, the average value of the resonant frequency of 168 elements is 158.56 kHz and the standard deviation is 4.96 kHz, with 166/168 yield. For the receiver chip, the average value of the resonant frequency of 168 elements is 188.40 kHz and the standard deviation is 10.06 kHz with 163/168 element yield (Figure 70).

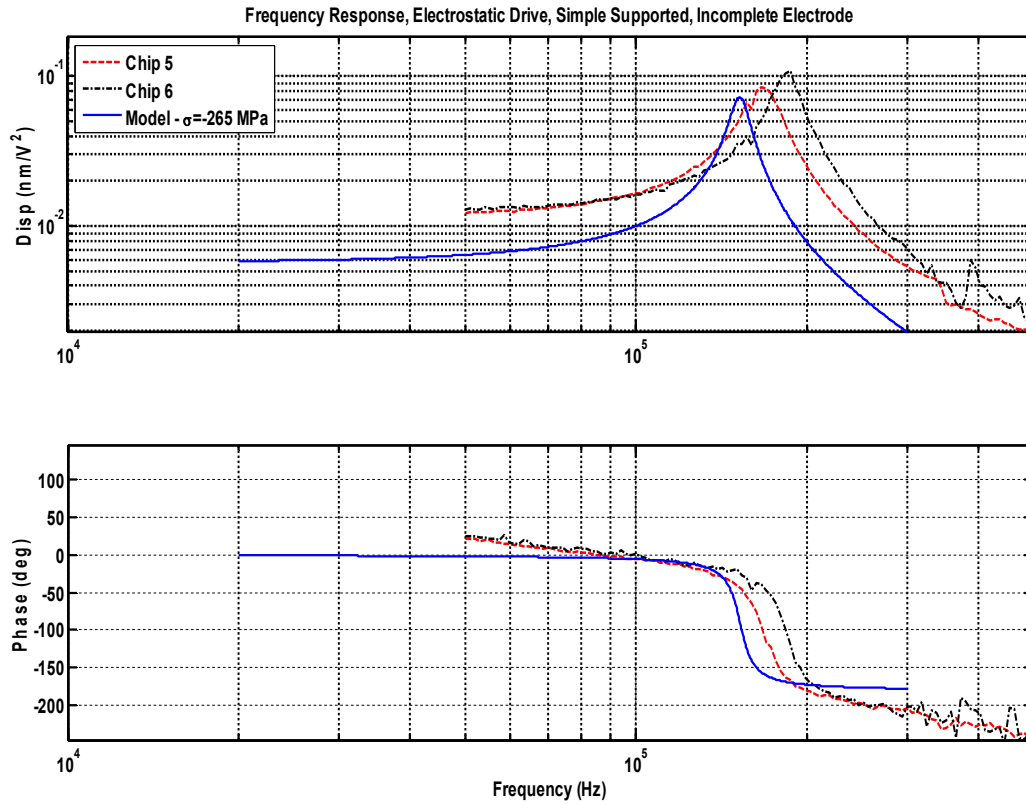


Figure 71: Predicted center point motion frequency response for a single element and the experimental result.

A comparison between predicted frequency response results and measurement is shown in Figure 71. The magnitude is normalized to the product of the applied DC bias and AC bias during electrostatic drive. Residual stress of electroplated nickel layer ($\sigma = -265$ MPa), as determined from CV data was included. Sensitivity of the nickel device (0.1 nm/V^2) is lower than the PolyMUMPs® chip (0.4 nm/V^2), due to the larger air gap. However, the nickel-on-glass chip has more elements, a higher drive voltage, and lower stray capacitance, which more than

make up for the lower sensitivity. The measured frequency response by LDV is in excellent agreement with model predictions.

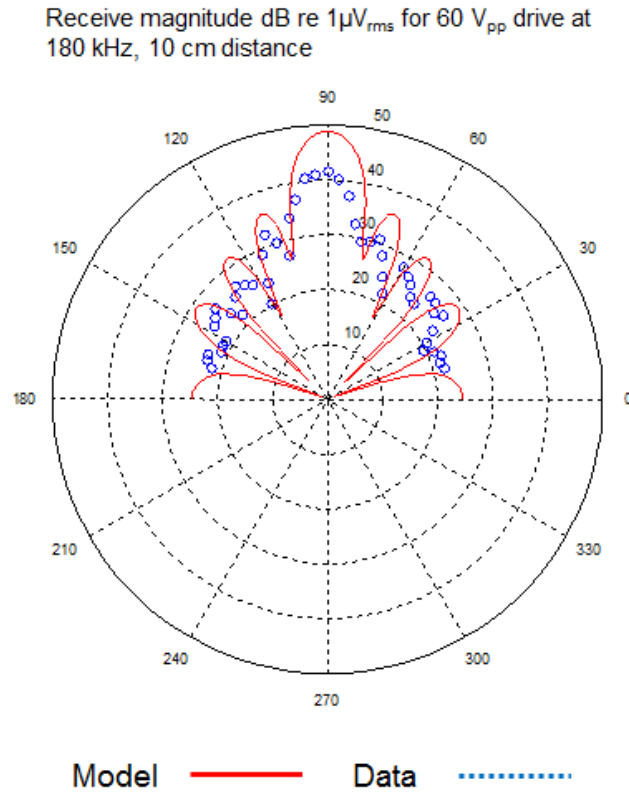


Figure 72: Acoustic transmit & receive test using cMUT Array (180 kHz) and beampattern.

A free field measurement was conducted using a pair of cMUT chips. The transmitter produced an acoustic signal at 180 kHz. It was driven electrically at 90 kHz drive at 20 V_{peak-to-peak}. Again, frequency doubling due to square law electrostatics gave acoustics at 180 kHz. The DC bias on the receiver was 10 V. The transducer arrays were 10 cm apart. The measured response was 0.12 mV_{rms} (42 dB re 1 mV_{rms}) at peak, which compares well to the predicted 0.15 mV_{rms} from the computational model as shown Figure 72. The -3 dB beamwidth is as

expected at 13 degrees (6.5 degrees on either side of center). The side lobes are down by 20 dB compared to the main lobe.

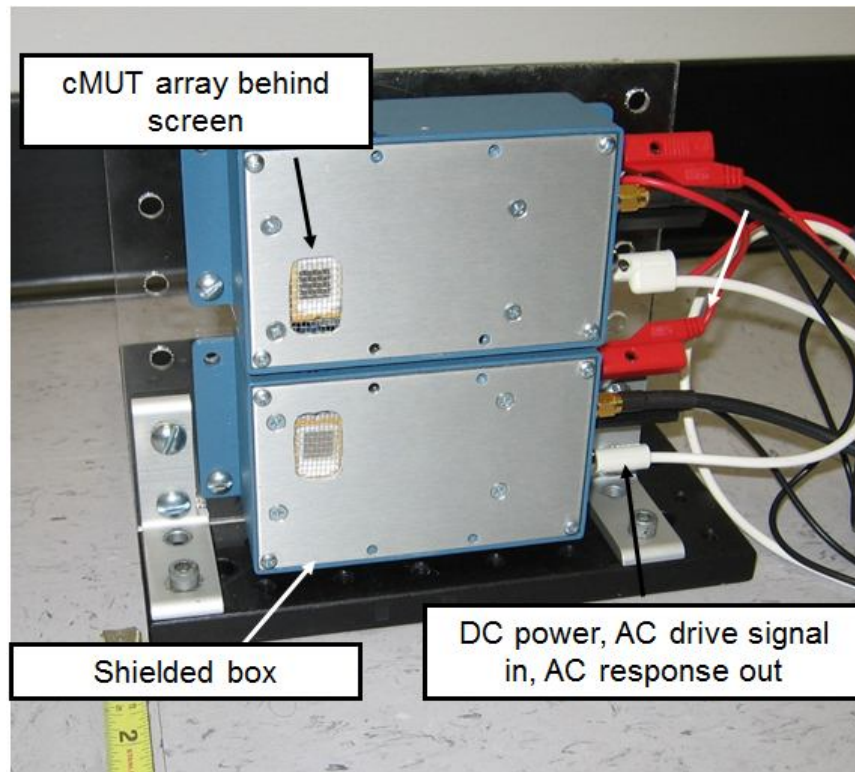


Figure 73: cMUT mounting package shielded with EMI protection.

There is the need for electromagnetic interference (EMI) protection. The increase in voltage swing of the transmitter and in bias voltage of the receiver accompanies the high possibility that EMI can contaminate the receiving system. Therefore a fully receiver-enclosed Faraday cage is needed. However, the use of this Faraday cage can prevent the portability of the ultrasonic system. Therefore the Faraday cage should be small and enclose the system with the smallest amount of surface in the right place (Figure 73). The cMUT arrays and electronics are

installed in a mounting package shielded with EMI protection. In front of the chips, a Faraday cage protects from EMI permeating into the system.

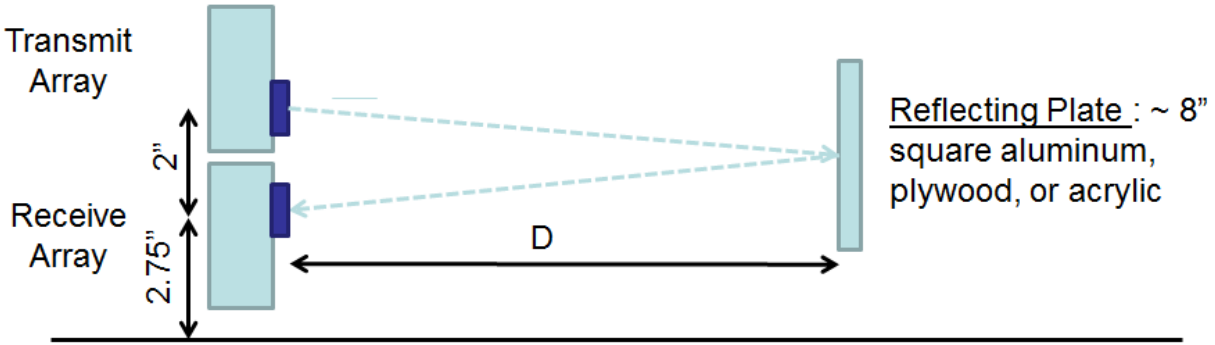


Figure 74: Schematic of range test set-up using cMUT array.

To investigate the achievable range of an acoustic wave, range testing was conducted at 180 kHz, as shown in Figure 74 and 75. The drive signal was 140 V_{pp} at 90 kHz, and the DC bias on the receiver side was 10 V. Unlike the previous experimental set-up with the PolyMUMPs® chip, the nickel-on-glass chip has their angle fixed during range testing. Various reflection materials including plywood, aluminum, and acrylic were used. Experimental results for acoustic continuous wave transmit and receive using two chips show a maximum range of 1.5 m as shown Figure 76. Signal power decreases with the square of D as expected. With $D \geq 1.5$ m, the signal decreases below the background reflection level (-67 dBV_{rms}). Each material has the similar range results. Noise is always dependent on sampling. In this experiment, the sampling frequency was $F_s = 1$ MHz and the number of samples was 2^{20} , resulting in a total data acquisition time of 1.0 seconds per point.

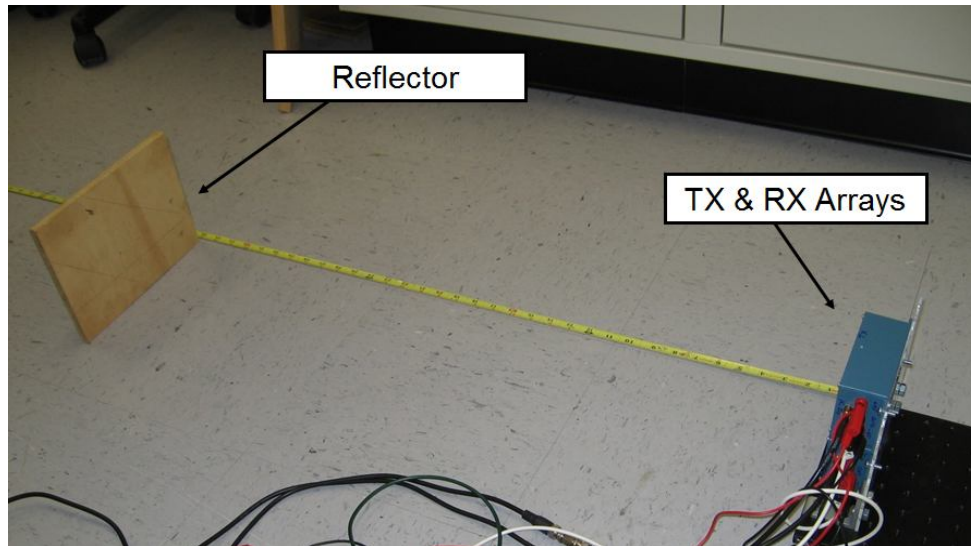


Figure 75: Range test set-up using cMUT array.

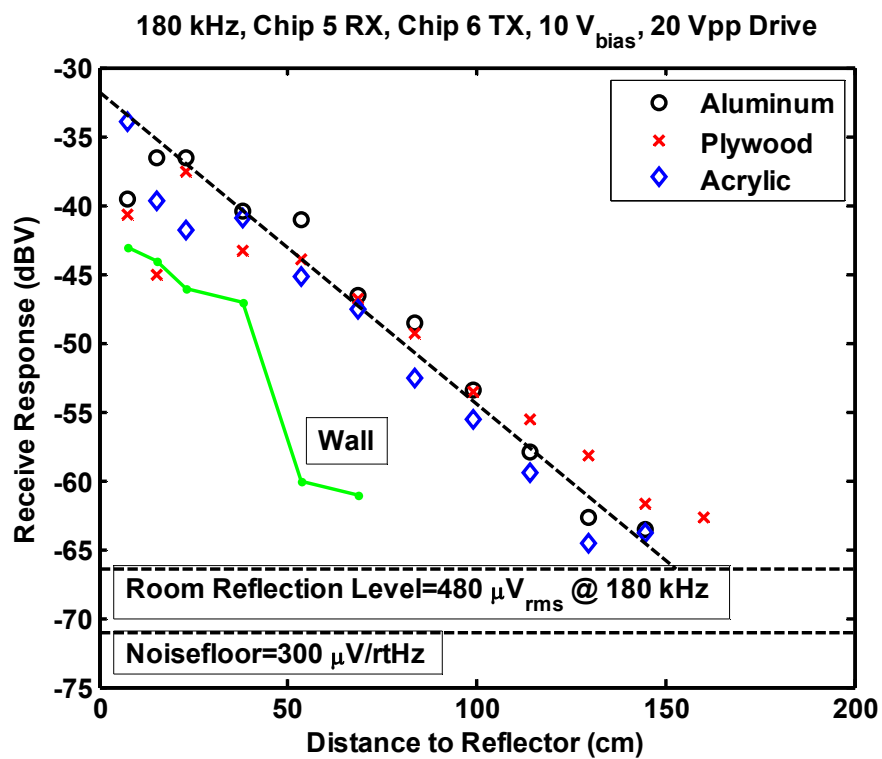


Figure 76: Range test result using cMUT array with three reflection materials such as aluminum, plywood, and acrylic.

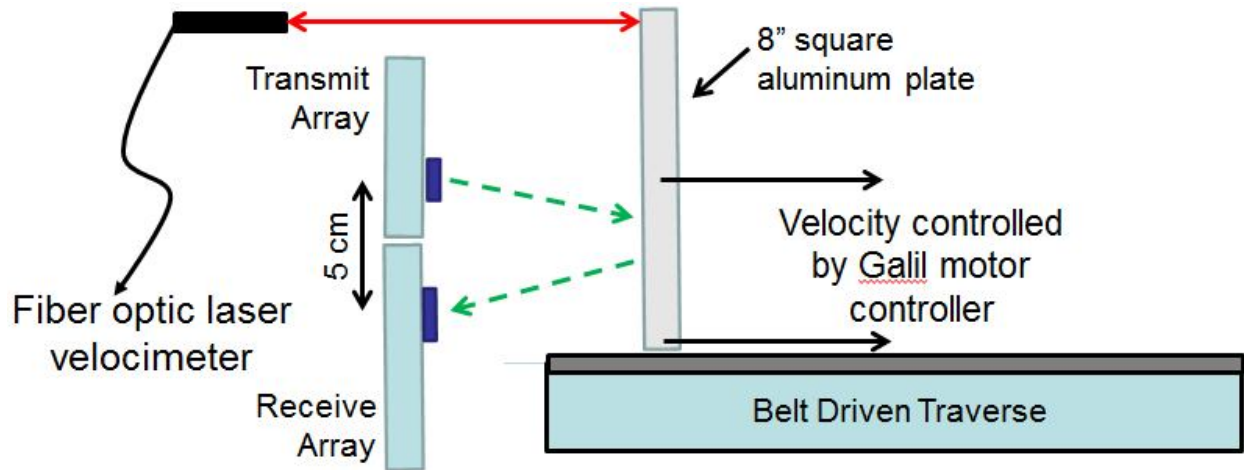


Figure 77: Schematic of a set-up for velocity test.

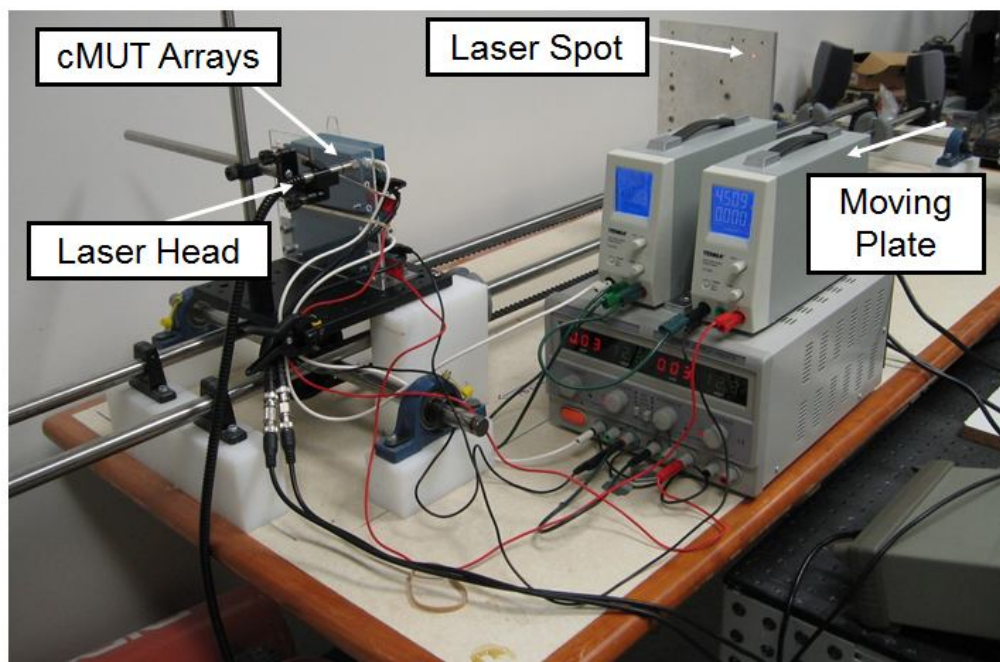


Figure 78: A set-up for velocity test.

Finally, the velocity sled was used to demonstrate measureable Doppler shifts. The continuous acoustic wave at 180 kHz was sent from the transmitter while the sled accelerated up to speed. For velocity comparison, a laser fiber optic vibrometer was used.

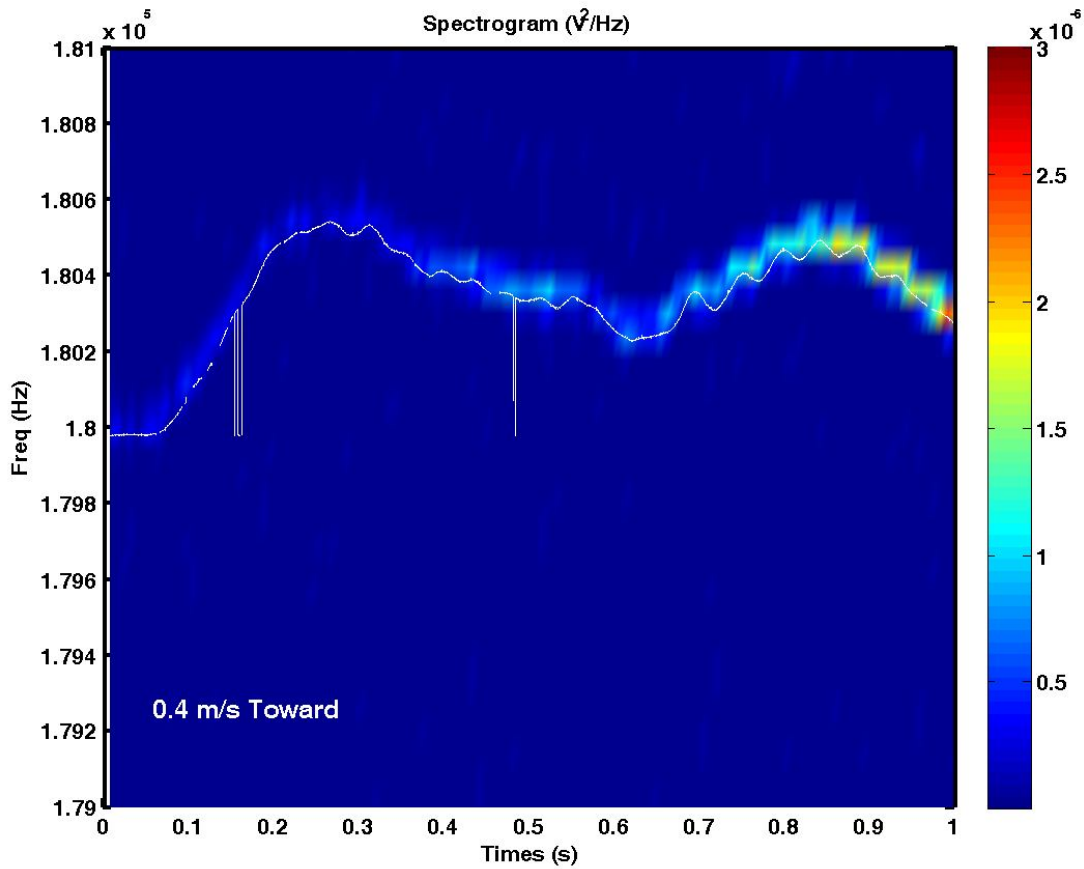


Figure 79: Spectrograms of the sled velocity moving toward the sensor at 0.4 m/s.

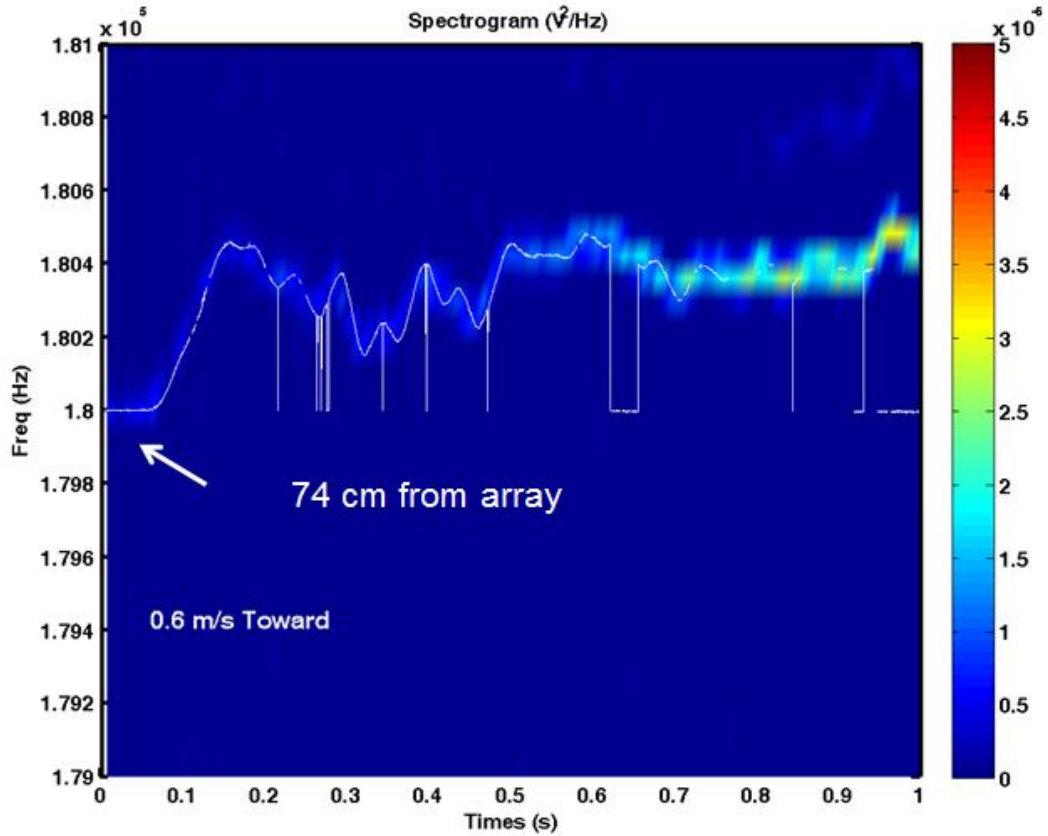


Figure 80: Spectrogram of the sled velocity moving toward the sensor at 0.6 m/s.

Figure 79-80 show spectrograms of the sled velocity moving toward the sensors at 0.4 and 0.6 m/s. As the reflector moves closer, the signal gets louder. The white line shows the expected frequency based on Doppler shifts computed from the velocity as measured by LDV. In the LDV data, there are missing points due to poor reflection for some distances. Velocity profile measured by cMUT sensors matches the LDV data very well. Data was captured at $F_s=1$ MHz, and sampling points $N=2^{20}$. The spectrogram uses a 2^{14} point window (Hamming window) with 50% overlap. The time window 0.016 sec, thus $\Delta f=61$ Hz (5.8 cm/s) was used.

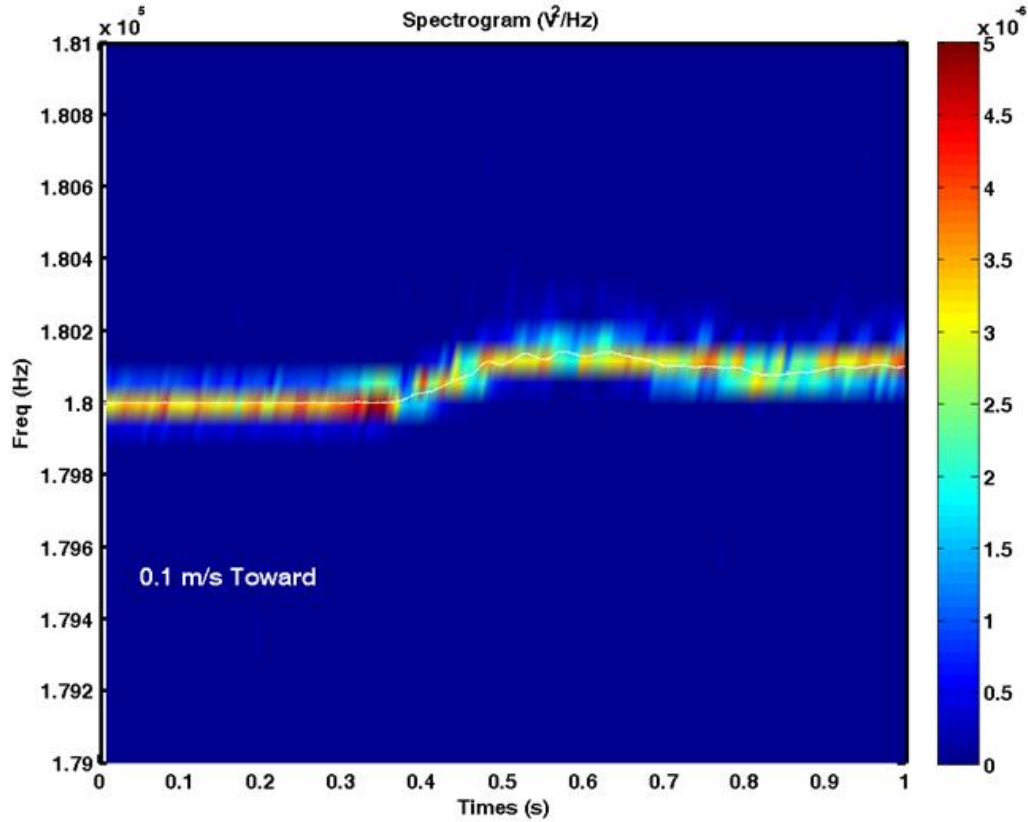


Figure 81: Spectrogram of the sled velocity moving toward the sensors at 0.1 m/s.

Figure 81 shows a spectrogram of the sled velocity moving toward the sensors at 0.1 m/s. At lower speeds, the limitation on velocity due to the windowing is shown and errors increases. In LDV data, there is no missing point at the low speed test. The velocity profile measured by cMUT sensors matches the LDV data.

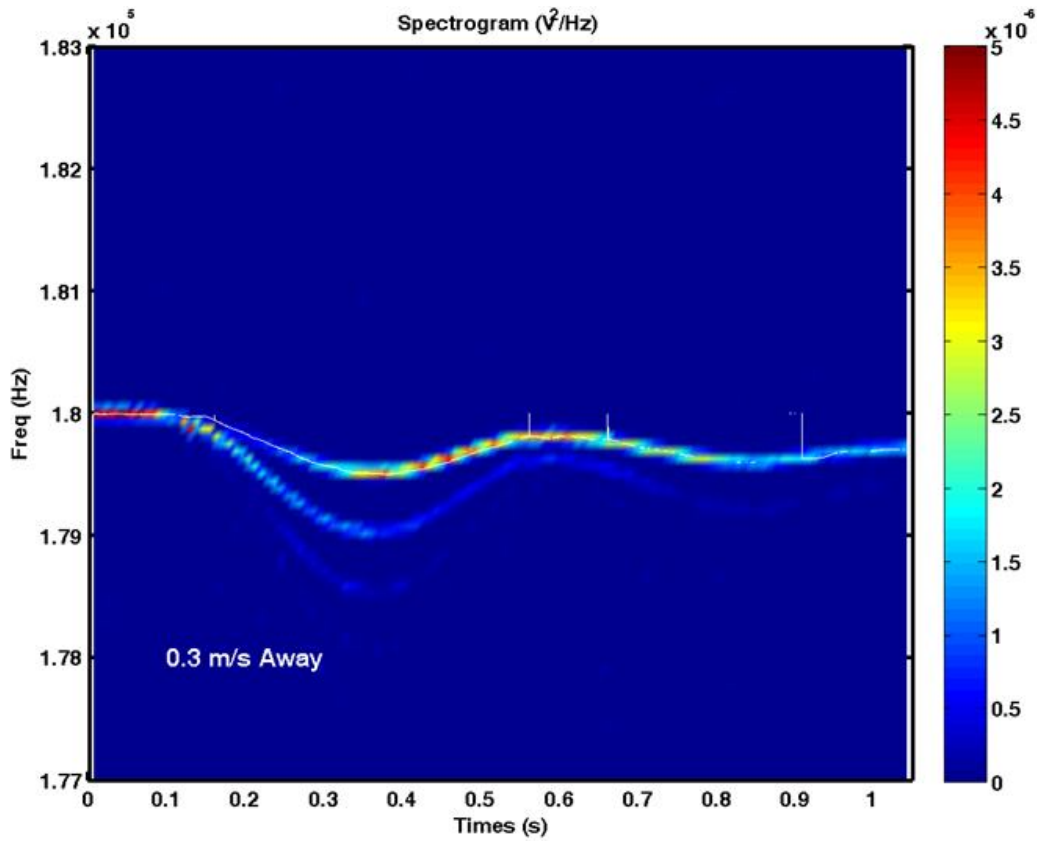


Figure 82: Spectrograms of the sled velocity moving away from the sensors at 0.3 m/s

Figure 82 shows a spectrogram of the sled velocity moving away from the sensors at 0.3m/s. In the spectrogram, there were ‘ghost’ bands at harmonics. This phenomenon requires further investigation. It could be due to multiple reflections.

Chapter 6

Conclusion and Future Work

This chapter shows conclusions and future works.

6.1 Conclusion

Rangefinding technology is required for mobile robot positioning, personal navigation systems, micro air vehicle navigation, obstacle detection, and map building [1-6]. This technology promoted the developments of several sensors: RADAR systems, laser rangefinding systems, and infrared rangefinding systems. However, these sensors do not meet the need for mobile application (size, weight, and cost). The laser rangefinding systems and power RADAR based systems are large and require high power consumption. Furthermore, the infrared rangefinder has problems including nonlinearity and random errors during the data read.

MEMS ultrasonic sensors provide the impetus for several positive changes to the measurement of distance and velocity. First, MEMS acoustic sensors allow for batch fabrication, integration with electronics, and the potential to create quality high volume products at low costs. Second, the MEMS sensor due to its small size consumes mW of electrical power to generate acoustical waves. Laser rangefinders generate sufficient optical power from the order of 1W electrical drive source [10]. Therefore, in this work, an ultrasonic velocity sensor using MEMS technology is explored as an alternative or complementary sensing technology. This technology

works off of a different sensing modality than other rangefinding sensors such as laser based, RF RADARs or piezoelectric systems and may have advantages in certain environments.

An acoustic Doppler velocity measurement system using MEMS capacitive micromachined ultrasound transducer (cMUT) array technology was modeled with lumped element modeling, developed with a micro fabrication and characterized with a variety of experiments.

This dissertation contains cMUT modeling using the lumped element model [17] of a single element transducer. LEM includes an environmental loading model, diaphragm mechanics, and electromechanical coupling.

Along with LEM, the nickel-on-glass chip is developed with a 3 layer nickel-on-glass MEMS fabrication process. The process is considerably simple to and provides a baseline fabrication process for the production of a range of low stray capacitance sensors.

For simple data acquisition from the cMUT sensors, the receiver electronics were designed, based on the sensor properties. The receiver consists of the preamplifier and the voltage amplifiers. This circuit has a low level of noise floor. Furthermore, for use of a high voltage swing for the input, the transmitter with the bridge circuit was designed. Both electronics were enclosed with Faraday cages for EMI protection.

| | PolyMUMPs® | Nickel-on-glass |
|--|---------------|-----------------|
| Snapdown Voltage | 60 | 290 |
| Sensitivity (nm/V^2) | 0.4 | 0.1 |
| C_{sensor} | 4 nF | 65 pF |
| R_{sensor} | 54 M Ω | 200 M Ω |
| Range (m) | 0.6 | 3.0 |
| Driving Voltage (V_{pp}) | 20 | 140 |

Table 13: Performance comparison between a PolyMUMPs® chip and a nickel-on-glass chip.

Experimental results show a maximum range of 60 cm (30 cm out and 30 cm back) using the PolyMUMPs arrays. To improve the range problem, the nickel-on-glass process was developed. The nickel-on-glass chips have high snap down voltage (290V). Therefore, a high voltage swing can be used (140 $V_{\text{peak to peak}}$). The nickel chips have a maximum range of 3.0 m (1.5 m out and 1.5 mm back).

LDV measurements demonstrate that the membrane displacement of the PolyMUMPs® array at center point is $0.4 \text{ nm}/\text{V}^2$ at 185 kHz and that of nickel array $0.1 \text{ nm}/\text{V}^2$. Beampattern measurements show a 13 degree -3dB beamwidth (6.5 degrees either side of center). The sidelobes are 15 dB below the main lobe. These results agree with theoretical models. A velocity sled was constructed and used to demonstrate measureable Doppler shifts at varying velocities. The Doppler shifts match the expected frequency shifts over this range. With the nickel-on-glass chips, velocity testing at velocities from 0.1 to 0.6 m/s shows excellent agreement with a laser velocimetry. Velocity resolution is approximately 5 cm/s in a 60 Hz band (60 velocity updates per second). This system was demonstrated for reflectors out to 74 cm in this setup (16 millisecond averaging). Velocity resolution and time resolution can be traded off dynamically. By using a

longer time window and thereby reducing temporal resolution, velocity resolution can be increased. This tradeoff can be managed flexibly during signal processing.

6.2 Future Work

There are several areas where this work can be improved. The major challenges for this type of system appear to be efficient algorithms for real time processing. The current approach uses post processing after obtaining data. The post processing inhibits the mobility. For real time processing, the digital system needs to be designed and integrated.

Another issue is an increase in the bias voltage of the receiver electronics. The current work uses 10 V DC bias because of a high heating problem. With 90 V DC bias or higher, high signal-to-noise ratio can be obtained and maximum range of a device can increase.

Use of the device in harsh environments (wind, snow, rain) can be considered. The current test set-ups of the research are based on clear transmission paths and normal specular reflection. Further study of angle dependence and environmental effects is needed.

Reflection off of various surfaces can be tested. Each material has different reflection rates and reflection angles, considering surface roughness of the material. The dissertation uses only 3 materials (aluminum, plywood, and acrylic). Therefore, various materials can be tested for reflection rate and angle measurement.

Distance measurements using frequency modulated continuous wave (FMCW) can be included in the system. With FMCW, velocity information and distance information can be obtained simultaneously. This can contribute to the utility of the system.

Appendix A

A.1 Fabrication Runsheet of the Nickel-on-glass Chip

RUNSHEET

Process Name: Surface Micromachining

Process Goal: Micromachine various surface micromachined devices with a copper sacrificial layer, nickel structure, and Cr/Au interconnect.

Refer to SOPs: “Standard Lithography”, “OAI Aligner”, “Laurell Spinner”, “NSC-3000 Sputter”, “March RIE”, “Copper Electroplating”, “Nickel Electroplating”, “LOR Liftoff”.

Starting Substrates: 100±.2mm Soda Lime 550±50µm Thick DSP (60/40) W/Rounded Edges & Primary Flat Only.

| <u>Step Name</u> | <u>Parameters</u> | <u>Measurements/Comments</u> |
|---|--|---|
| 1. Examine mask | Microscope. | |
| 2. Piranha Clean | Piranha clean starting substrates, 1:1 H ₂ SO ₄ :H ₂ O ₂ (30%) by volume. 10 mins clean, 5 mins DI water x 2. | |
| 3. O₂ Clean | 200W, 120sec, 100% O ₂ (~300 mT) in March RIE | |
| 4. Lithography #1 Metal layer: 250nm Thick and 10µm minimum feature size | LOR20B: 500 rpm 4sec, 2000 rpm 45sec, 200C 5min softbake; AZ9245: 500 rpm 5 sec spread, 4500 rpm 60 sec spin, 115C 1 min 30 sec softbake, 20 sec exposure (hard contact), 2~3 min develop in AZ400K:water 1:3, 2 x 2 DI water rinse, air gun dry | <u>Notes:</u> LOR20B: <u>2000 rpm = 2.0 µm</u> AZ9245: <u>4500 rpm = 3.5 µm</u> |
| 5. O₂ Descum | 150W, 30 sec, 100% O ₂ (280 mT) plasma descum in March RIE | |
| 6. Sputter Cr/Au | Pump down for > 1 hour (<5e-5 torr). Use 60 sec target clean. Sputter on 75 nm Cr | Cr: 2.8 A/sec |

| | | |
|--|--|---|
| | (200 W), 225 nm Au (150 W) at 5 mT | Au: 8 A/sec <u>Ra ~ 5 nm</u> |
| 7. Liftoff | Heating Remover 1165 to 60C for > 5hr. (No need for swab and sonicator). Don't let metal particles settle out and dry in place!!! Rinse with IPA, 2 x DI water. Air gun dry. | Measure metal thickness and roughness |
| 8. Lithography #2 Seed layer: 2µm Thick and 10µm minimum feature size | HMDS/SPR220-3 500 rpm 4 sec spread, 3000 rpm 30 sec spin, 115C 90secsoftbake, 6sec exposure (hard contact), 90 sec 115C PEB, 2 min 15 sec develop MFCD26, 2 x 2 DI water rinse, air gun dry | <u>Notes:</u> <u>3000rpm=2.1 µm</u> Measure resist thickness, width of smallest feature, and alignment: |
| 9. O₂ Descum | 150 W, 30 sec, 100% O ₂ (280 mT) plasma descum in March RIE | |
| 10. Sputter Ti/Cu | Pump down for >1 hours. Sputter on 30 nm Ti (150 W), 300 nm Cu (200 W), at 5 mT | <u>Ti = 0.8 A/sec</u> <u>Cu = 3.3 A/sec</u> <u>Ra ~ 5 nm</u> |
| 11. Liftoff | Liftoff Ti/Cu in acetone, with agitation, swabbing, and sonication as needed. Be careful not to let metal particles settle out and dry in place!!! Rinse with acetone/IPA, 2 x DI water. Air gun dry. | Measure metal thickness and roughness |
| 12. Lithography #3 Sacrificial layer: 2µm Thick and 10µm minimum feature size | HMDS/AZ9245 500 rpm 5 sec spread, 1000 rpm 60 sec spin, 115C 2.5 min softbake, 35 sec exposure (hard contact), 5 min develop in AZ400K:water 1:3, 2 x DI water rinse, air gun dry | <u>Notes:</u> 1000 rpm= 8 µm thick Measure resist thickness |
| 13. O₂ Descum | 150 W, 30 sec, 100% O ₂ (280 mT) plasma descum in March RIE | Measure photoresist thickness |
| 14. Copper oxide | Etch copper oxide off in Copper Plating | |

| | | |
|---|--|---|
| etch | solution for 3min, 2 x 2 min water rinse and immediately into nickel plating solution. | |
| 15. Copper Electroplating | Plate on thick Cu (filter). See Cu plating SOP. TECHNI COPPER FB BATH RTU, room temp, 5 mA/cm ² results in 150 nm/min. 2 x DI water rinse. | <u>Notes:</u> Wafer area = 78 cm ² , so 5 mA/cm ² is ~0.4 A. Ra = 10~15 nm |
| 15. Strip Photoresist | 10 minute acetone soak, 5 min IPA, 3 min x 2 water, air dry, | Measure metal thickness |
| 16. O₂ Descum (As needed) | 200W, 120sec, 100% O ₂ (300 mT) in March RIE | |
| 17. Lithography #4 Structure layer: 8um structure and 4um minimum feature size | HMDS/AZ9260, 500 rpm 5 sec spread, 1500 rpm 60 sec spin 115C 2.5 min softbake, 1 st : 80sec EBR exposure, 7min Develop (acetone swab 300 rpm as needed), 2 nd : 20 sec exposure, 8 min develop, AZ400K:water 1:3, 2 x 2 DI water rinse, air gun dry | <u>Notes:</u> <u>1500 rpm = 9~10 um</u> Measure resist thickness |
| 18. O₂ Descum | 150W, 30 sec, 100% O ₂ (280 mT) plasma descum in March RIE | |
| 20. Copper oxide etch | Etch copper oxide off in Copper Plating solution for 3min, 2 x 2 min water rinse and immediately into nickel plating solution. | |
| 21. Nickel Electroplating | Plate on thick Ni. See Ni plating SOP. NICKEL SULFAMATE SEMI BRIGHT RUT MECHANICAL AGITATION, 50C, 5 mA/cm ² results in 100 nm/min. | <u>Notes:</u> An area is 30.74cm ² , so 5 mA/cm ² is 0.15 A. If accounting EBR, I = 0.2 A. |
| 22. Dice wafer | MA dicing saw – dice into individual dies | <u>Note:</u> chips are 10.2 mm center to center on cuts, results in 10.1 mm x 10.1 mm chips after dicing. |
| 23. Strip Photoresist | 10 min acetone soak, 5 min IPA, 5 min x2 water | |
| 24. O₂ Clean | 200W, 120 sec, 100% O ₂ (280 mT) plasma clean in March RIE | |

| | | |
|--------------------------------------|---|-----------------------------|
| (If necessary) | | |
| 25. Copper Wet Etch (Release) | 1:1:18 CH ₃ COOH: H ₂ O ₂ : Water 1 day, 10min x2 DI water rinse, IPA 10 min, Methanol 30 min, 2hr dry in drybox at reduced relative humidity. | RH in a dry box during dry: |

Appendix B

Matlab Script

B.1 Modeling of a single transducer of the nickel-on-glass chip.

```
%Working in m-kg-s units
%For a Doppler CMUT device with holes using the CMUT model as
%described in the JMEMS paper (2011) including electrostatic
%spring and gap change due to DC bias
%but also with the model of hole damping and squeeze film damping from
%before

%Geometric properties of the design:
a=300e-6; %radius of diaphragm (m)
agap=a; %radius of gap cavity (m)
relect=195e-6; %radius of the electrode (m)
Ahole2=5e-6; %radius of hole in poly2 layer... this is the diaphragm (m)
CC2=100e-6; %center to center spacing of holes in poly 2 layer(m)
n2=28;%Number of holes

%Electrical properties of the design:
%Note : if using AC only with amplitude V0 (so 2*V0 peak-to-peak),
%set Vdc=sqrt((V0^2)/2), Vac=0.5*Vdc. Also set f=2*drive freq
%Vdc=sqrt(10); %Applied bias (Vdc)
%Vac=0.5*sqrt(10); %Applied AC voltage (Vac)
Vdc=5;
Vac=5;
ep0=8.854e-12; %Permittivity of free space (F/m)
Cfb=670e-12; %Feedback capacitor in charge amp (F)
Rfb=1e6; %Feedback capacitor in the charge amp (Ohms)
Cblock1=0.1e-6; %DC blocking cap between charge amp and first inverting amp
(F)
Rblock1=1e3; %Resistor to ground after DC blocking cap and first inverting
amp (Ohms)
Cblock2=0.1e-6; %DC blocking cap between charge amp and second inverting amp
(F)
Rblock2=1e3; %Resistor to ground after DC blocking cap and second inverting
amp (Ohms)
Gain=400; %Total gain of both OP27 amps in the passband (gain 1 x gain 2)
Rp=200e6; %Stray resistance in parallel with diaphragms
Cp=61e-12; %Total chip capacitance (including package, wiring, etc)
Rs=14; %Stray resistance between diaphragm and metal trace (Ohms)
fbreak=8e6*Cp/Cfb; %High frequency break frequency for the AD797 (Hz)

%Material properties of structural layer:
%rhopoly2=2330; %Density of structural layer (kg/m^3) polysilicon
```

```

rhopoly2=8912; %Density of structural layer (kg/m^3) nickel
%E=160e9; %Elastic modulus of structural layer (Pa) polysilicon
E=200e9; %Elastic modulus of structural layer (Pa) nickel ... may reduce for
some plating conditions!
%nu=0.22; %Poisson ratio for structural layer (dimensionless) polysilicon
nu=0.31; %Poisson ratio for structural layer (dimensionless) nickel
sigmapoly2=-265e6; %Residual stress in structural layer (Pa)

%Thicknesses of layers:
tpoly2=9e-6; %thickness of structural layer (m) ... diaphragm
Tox=5e-6; %thickness of the gap (m)

de=0.0; %Material hysteretic damping (fractional)

%Material properties of the gold layer on top of the diaphragm
rhogold=19300; %Density of gold (kg/m^3)
Egold=79e9; %Modulus of gold (Pa)
tgold=0e-6; %Gold thickness (set to zero if not used to coat the diaphragm)
nugold=0.4; %Poisson ratio of gold
sigmagold=0; %Residual stress in gold (Pa)

%Material Properties of Parylene Layer on top of the gold
rhopary=1289; %Density of Parylene-C (kg/m^3) given in (g/cm^3) from
http://www.parylene.com/technology/PTC-Parylene-Properties-Chart-2007.pdf
E2=59e6; %Elastic Modulus of Parylene-C (Pa) C. Y. Shih, T. A. Harder and Y.
C. Tai "Yield strength of thin-film parylene-C " Microsystems Technologies
p407
nu2=0.4; %Poisson's ratio for Parylene-C (dimensionless) C. Y. Shih, T. A.
Harder and Y. C. Tai "Yield strength of thin-film parylene-C " Microsystems
Technologies p409
tpary=0e-6; %thickness of Parylene-C (m)
sigmapary=0; %Residual stress in parylene (Pa)

%Acoustic properties of the medium:
rho=1.21; %density of air environment (kg/m^3)
%rho=1000; %density of water environment (kg/m^3)
c=343; %speed of sound in air environment (m/s)
%c=1482; %speed of sound in water environment (m/s)
mu=2e-5; %Viscosity of air (Pa*s)

fstart=2e4; %start frequency (Hz)
fstop=3e5; %stop frequency (Hz)
numfreq=1000;

%Compute pressure at this distance from the center of the array:
Rcenter=0.1; %m

%END USER PARAMS-----

f=logspace(log10(fstart),log10(fstop),numfreq);
Vcav=Tox*pi*agap^2; %volume of the gap (m^3)

%New bending stiffness for the thin laminate plate of Polysilicon and

```

```

%Parylene and Gold
z1=tpoly2/2;
z2=tpoly2+(tgold/2);
z3=tpoly2+tgold+(tpary/2);
yc=((z1*E/(1-nu^2))+(z2*Egold/(1-nugold^2))+(z3*E2/(1-nu2^2)))/((E/(1-
nu^2))+(Egold/(1-nugold^2))+(E2/(1-nu2^2)));
y1=z1-yc;
y2=z2-yc;
y3=z3-yc;
Dpoly=(E/(1-nu^2))*((tpoly2^3)/12)+tpoly2*y1^2;
Dgold=(Egold/(1-nugold^2))*((tgold^3)/12)+tgold*y2^2;
Dpary=(E2/(1-nu2^2))*((tpary^3)/12)+tpary*y3^2;
Dnew=Dpoly+Dgold+Dpary;

%Diaphragm acoustic compliance, mass and center point to volume velocity
%displacement (From Sheplak and Nishida, JMEMS, Dec 2007):
Cdia=(pi*a^6/(12*16))/Dnew; %Volume compliance of a thin laminate bending
circular clamped plate [m^3/Pa]
Mdia=(9/(5*pi*a^2))*(rhopoly2*tpoly2+rhogold*tgold+rhopary*tpary); %Effective
mass of a thin laminate bending circular clamped plate
ctr=3/(pi*a^2); %Center point to volume displacement ratio of a pure bending
circular clamped plate [m/m^2]

%Add in residual stress effects:
if (sigmapoly2*tpoly2+sigmagold*tgold+sigmapary*tpary)==0
    Cdia=Cdia;
else

Cdia=1/(1/Cdia+1/((5*pi*a^4)/(9*(2.4048^2)))/(sigmapoly2*tpoly2+sigmagold*tgol
d+sigmapary*tpary));
end

%To add in material damping:
Cdia=Cdia/(1+1i*de);

%Compute the electrostatic coupling and electrostatic spring:
r1=linspace(0,relect,1000);
r2=linspace(0,a,1000);

%Using a clamped static bending shape
%Junuthula Reddy, "Theory and Analysis of Elastic Plates and Shells", p. 168.
% w1=(1-((r1/a).^2)).^2;
% w2=(1-((r2/a).^2)).^2;

%For static modeshape simply supported:
%Junuthula Reddy, "Theory and Analysis of Elastic Plates and Shells", p. 168.
nu=0.31; %Poisson ratio
w1=((5+nu)/(1+nu)-2*(3+nu)/(1+nu))*((r1/a).^2)+((r1/a).^4))*((1+nu)/(5+nu));
w2=((5+nu)/(1+nu)-2*(3+nu)/(1+nu))*((r2/a).^2)+((r2/a).^4))*((1+nu)/(5+nu));

%We want to find the displacement due to the DC bias application and
%from that get Celect and N. Start from zero displacement and iterate:

```

```

x=0; %Centerpoint static deflection
change=1;
iter=0;
while abs(change)>1e-3 && iter<100
    term=((Tox-x*w1)/ep0).^(-3);
    term2=((Tox-x*w1)/ep0).^(-2);

    int1=trapz(r1,w1.*term2.*r1*2*pi);
    int2=trapz(r2,w2.*r2*2*pi);
    int1b=trapz(r1,w1.*w1.*term.*r1*2*pi);

    %Electrostatic spring:
    Celect=-ep0^2/Vdc^2*int2*int2/int1b;

    %Electroacoustic coupling:
    N=int1/int2*Vdc/ep0;

    oldx=x;
    %Using these values get an estimate of x:
    x=((N*0.5*Vdc)*(1/Cdia+1/Celect)^(-1))/int2;

    change=(x-oldx)/x;
    iter=iter+1;
end
%Cavity volume compliance:
Ccav=(Vcav-x*int2)/(rho*c^2); %Cavity compliance of the air gap.

for cnt=1:numfreq,
    % disp([num2str(round(cnt/numfreq*100)) '%complete'])
    omega=f(cnt)*2*pi;

    lambda=c/f(cnt);
    k=(2*pi)/lambda;

    %External environmental loading:
    %Simply Supported:
    RA1=0.243*rho*c/(pi*a^2);
    CA1=5.52*pi*a^3/(rho*c^2);
    RA2=rho*c/(pi*a^2);
    MA1=0.643*rho/(pi*a);

    %Clamped:
    %RA1=0.471*rho*c/(pi*a^2);
    %CA1=2.016*pi*a^3/(rho*c^2);
    %RA2=0.850*rho*c/(pi*a^2);
    %MA1=0.628*rho/(pi*a);

    Z1=1./(1/RA1+CA1*1i*omega);
    Z2=Z1+RA2;
    Zac=1./(1./Z2 + 1./(MA1*1i*omega));

```

```

%Squeeze film damping model (with perforations...Scvor's formula):
AScvor=(pi*(Ahole2)^2)/(CC2^2); %Ratio of hole area to unit cell area
CA=AScvor/2-(AScvor^2)/8-0.25*log(AScvor)-3/8; %Correction factor
Rsqueeze=12*mu*CA/(n2*pi*Tox^3);

%Diaphragm hole model (Martin, Liu... Sheplak, Nishida, AIAA, 44th AIAA
Aerospace Sciences Meeting and Exhibit, Reno, Nevada, Jan. 9-12, 2006):
Rhole=(1/n2)*8*mu*(tpoly2+tpary)/(pi*Ahole2^4);

Z1=Rhole+Rsqueeze;
Z2=Mdia*li*omega+(1/(Cdia*li*omega)+1/(Celect*li*omega))+Rs*N*N;
Z3=(1/(Ccav*li*omega));

%Transfer function giving volume velocity out (m^3/s) per AC voltage
%applied to the electrodes for an isolated element.
H1=-(Zac+Z3+Z1)/((Z1+Z2)*(Zac+Z3)+Z1*Z2)*N;

%Transfer function giving volume velocity out (m^3/s) per pressure
%applied to the surface of the diaphragm (Pa) for an isolated element.
H2=-Z1/((Z1+Z2)*(Zac+Z3)+Z1*Z2);

%Transmit Response:
u(cnt)=H1*Vac*1/(Rs*Cp*li*omega+(Rs+Rp)/Rp); %This is total volume
velocity of the membrane in m^3/s in response to electrostatic drive
uctr(cnt)=-u(cnt)*ctr/(li*omega)*1e9/(Vac*Vdc); %This is the center point
displacement in nm/V^2
VD(cnt)=u(cnt)/(li*omega)/(Vac*Vdc); %This is the volume displacement in
m^3/V^2
Pspatial(cnt)=u(cnt)*li*rho*f(cnt).*exp(-li*omega*Rcenter/c)./Rcenter;

%Receive Response:
P=1;
Uout(cnt)=H2*P; %This is the volume velocity in m^3/s
uctr_receive(cnt)=Uout(cnt)*ctr/(j*omega)*1e9/(P); %This is the
%center point displacement of each element in nm/Pa

Vout(cnt)=-
Uout(cnt)*N*(Rp*Rfb/((1+Cfb*Rfb*li*omega)*(Rp+Rs+Rs*Rp*Cp*li*omega)))*((Rbloc
k1*Cblock1*li*omega)/(Rblock1*Cblock1*li*omega+1))*((Rblock2*Cblock2*li*omega
)/(Rblock2*Cblock2*li*omega+1))*(Gain/(1+li*(omega/(fbreak*2*pi)))));

end

peak_cnt=find(abs(Pspatial)==max(abs(Pspatial)));
peak_frequency=f(peak_cnt);
fhalfpower1=max(f(abs(Pspatial)<(max(abs(Pspatial)))/sqrt(2) &
f<peak_frequency));
fhalfpower2=min(f(abs(Pspatial)<(max(abs(Pspatial)))/sqrt(2) &
f>peak_frequency));
deltaf=fhalfpower2-fhalfpower1;
percent_frac_bandwidth=100*deltaf/peak_frequency;

```

```

power_out=(pi*rho/c)*((abs(u(peak_cnt))*f(peak_cnt))^2);

disp('Transmit:')
pretty_print=sprintf('Peak Freq=%0.2f MHz, Percent Frac Bandwidth=%0.1f%%\nTotal Power Output at Peak=%0.3f microWatt',peak_frequency*1e-6,percent_frac_bandwidth,1e6*power_out);
disp(pretty_print)
pretty_print=sprintf('Pressure at R=%0.2f mm, %0.2f MHz, is %0.1f dB SPL\n',Rcenter*1000,peak_frequency*1e-6,20*log10(abs(Pspatial(peak_cnt))/(20e-6*sqrt(2))));
disp(pretty_print)


figure
subplot(2,1,1)
loglog(f,abs(Vout),'linewidth',2)
grid
hold on
set(gca,'Linewidth',2,'fontsize',10,'fontweight','bold')
ylabel('Sens (V/Pa)')
title('Frequency Response, Receive Sensitivity')
subplot(2,1,2)
semilogx(f,180*angle(Vout)/pi,'linewidth',2)
grid
set(gca,'Linewidth',2,'fontsize',10,'fontweight','bold')
xlabel('Frequency (Hz)')
ylabel('Phase (deg)')


figure
semilogx(f,20*log10(abs(Pspatial*Vdc*Vac)/(sqrt(2)*20e-6)),'linewidth',2)
grid
hold on
set(gca,'Linewidth',2,'fontsize',10,'fontweight','bold')
ylabel('Transmit Pressure (dB re 20 \muPa)')
title(['Transmit at R=' num2str(Rcenter) ' m, V_{ac}=' num2str(Vac) ', V_{dc}=' num2str(Vdc) ])
set(gca,'Linewidth',2,'fontsize',10,'fontweight','bold')


figure
subplot(2,1,1)
loglog(f,abs(uctr),'linewidth',2)
grid
hold on
set(gca,'Linewidth',2,'fontsize',12,'fontweight','bold')
ylabel('Disp (nm/V^2)')
title(['Frequency Response, Vac=' num2str(Vac) ' Vp, Vdc=' num2str(Vdc) ' Vdc'])
subplot(2,1,2)
semilogx(f,180*angle(uctr)/pi,'linewidth',2)
grid
set(gca,'Linewidth',2,'fontsize',12,'fontweight','bold')
xlabel('Frequency (Hz)')
ylabel('Phase (deg)')

```

B.2 Beampattern modeling of sensor arrays in the nickel-on-glass chip.

```
%Working in m-kg-s units
%For an AeroMEMS device with holes using the CMUT model as
%described in the JMEMS paper (summer 2009) including electrostatic
%spring and gap change due to DC bias and external pressure
%Includes fully coupled array effects - every motion of every element
%in the array creates a pressure field that forces every other element
%which radiates, etc ... for both transmit and receive mode.

rmax=0.1; %Maximum radius to compute to [m]
f=180e3; %Frequency [Hz]
xcut=0; %X-plane to cut through (for plotting purposes) [m] center of array
is x=0,y=0

NumX=12; %Num elements in array in X
NumY=14; %Num elements in array in Y
XSpace=724e-6; %Center-to-center spacing in x [m]
YSpace=578e-6; %Center-to-center spacing in y [m]

%Geometric properties of the design:
a=300e-6; %radius of diaphragm (m)
agap=1*a; %radius of gap cavity (m)
relect=195e-6; %radius of the electrode (m)
Ahole2=5e-6; %radius of hole in poly2 layer... this is the diaphragm (m)
CC2=100e-6; %center to center spacing of holes in poly 2 layer(m)
n2=28;%Number of holes

%Electrical properties of the design:
%Note : if using AC only with amplitude V0 (so 2*V0 peak-to-peak),
%set Vdc=sqrt((V0^2)/2), Vac=0.5*Vdc. Also set f=2*drive freq
Vdc=sqrt(450); %Applied bias(Vdc)
Vac=0.5*sqrt(450); %Applied AC voltage(Vac)
ep0=8.854e-12; %Permittivity of free space (F/m)
Rp=200e6; %Stray resistance in parallel with diaphragms
Cp=60e-12; %Total chip capacitance (including package, wiring, etc)
Rs=14; %Stray resistance between diaphragm and metal trace (Ohms)

%Material properties of MUMPS layers:
rhopoly2=8912; %Density of structural layer (kg/m^3) nickel
E=200e9; %Elastic modulus of structural layer (Pa) nickel ... may reduce for
some plating conditions!
nu=0.31; %Poisson ratio for structural layer (dimensionless) nickel
sigmapoly2=-265e6; %Residual stress in structural layer (Pa)

%Thicknesses of MUMPS layers:
tpoly2=9e-6; %thickness of poly2 (m) ... diaphragm
Tox=5e-6; %thickness of the gap (m)

%Material properties of the gold layer on top of the diaphragm
```

```

rhogold=19300; %Density of gold (kg/m^3)
Egold=79e9; %Modulus of gold (Pa)
tgold=0e-6; %Gold thickness (set to zero if not used to coat the diaphragm)
nugold=0.4; %Poisson ratio of gold

%Material Properties of Parylene Layer
rhopary=1289; %Density of Parylene-C (kg/m^3) given in (g/cm^3) from
http://www.parylene.com/technology/PTC-Parylene-Properties-Chart-2007.pdf
E2=59e6; %Elastic Modulus of Parylene-C (Pa) C. Y. Shih, T. A. Harder and Y.
C. Tai "Yield strength of thin-film parylene-C " Microsystems Technologies
p407
nu2=0.4; %Poisson's ratio for Parylene-C (dimensionless) C. Y. Shih, T. A.
Harder and Y. C. Tai "Yield strength of thin-film parylene-C " Microsystems
Technologies p409
tpary=0e-6; %thickness of Parylene-C (m)
de=0; %Material hysteretic damping (fractional)

%Acoustic properties of the medium:
rho=1.2; %density of air environment (kg/m^3)
%rho=1000; %density of water environment (kg/m^3)
c=343; %speed of sound in air environment (m/s)
%c=1482; %speed of sound in water environment (m/s)
Penv=100e3; %Ambient pressure in the environment (Pa)
mu=2e-5; %Viscosity of air (Pa*s)

%END USER PARAMS-----

%Create location of array elements in rectangular grid:
n=0;
Xelem=zeros(NumX*NumY,1);
Yelem=zeros(NumX*NumY,1);

for nx=1:NumX
    for ny=1:NumY
        n=n+1;
        if rem(ny,2)==1
            Xelem(n)=XSpace*(NumX-1)/(-2)+(nx-1)*XSpace;
            Yelem(n)=YSpace*(NumY-1)/(-2)+(ny-1)*YSpace;
        else
            Xelem(n)=XSpace*(NumX-1)/(-2)+(nx-1)*XSpace+(XSpace/2);
            Yelem(n)=YSpace*(NumY-1)/(-2)+(ny-1)*YSpace;
        end
    end
end

Vcav=Tox*pi*agap^2; %volume of the gap (m^3)

%New bending stiffness for the thin laminate plate of Polysilicon and
%Parylene and Gold
z1=tpoly2/2;

```



```

z2=tpoly2+(tgold/2);
z3=tpoly2+tgold+(tpary/2);
yc=((z1*E/(1-nu^2))+(z2*Egold/(1-nugold^2))+(z3*E2/(1-nu2^2)))/((E/(1-
nu^2))+(Egold/(1-nugold^2))+(E2/(1-nu2^2)));
y1=z1-yc;
y2=z2-yc;
y3=z3-yc;
Dpoly=(E/(1-nu^2))*((tpoly2^3)/12)+tpoly2*y1^2);
Dgold=(Egold/(1-nugold^2))*((tgold^3)/12)+tgold*y2^2);
Dpary=(E2/(1-nu2^2))*((tpary^3)/12)+tpary*y3^2);
Dnew=Dpoly+Dgold+Dpary;

%Diaphragm acoustic compliance, mass and center point to volume velocity
%displacement (From Sheplak and Nishida, JMEMS, Dec 2007):
Cdia=(pi*a^6/(12*16))/Dnew; %Volume compliance of a thin laminate bending
circular clamped plate [m^3/Pa]
Mdia=(9/(5*pi*a^2))*(rhopoly2*tpoly2+rhogold*tgold+rhopary*tpary); %Effective
mass of a thin laminate bending circular clamped plate
ctr=3/(pi*a^2); %Center point to volume displacement ratio of a pure bending
circular clamped plate [m/m^2]

%Add in residual stress effects:
if (sigmapoly2*tpoly2)==0
    Cdia=Cdia;
else
    Cdia=1/(1/Cdia+1/((5*pi*a^4)/(9*(2.4048^2)))/(sigmapoly2*tpoly2)));
end

%To add in material damping:
Cdia=Cdia/(1+i*de);

%Compute the electrostatic coupling and electrostatic spring:
r1=linspace(0,relect,1000);
r2=linspace(0,a,1000);

%Using a clamped static bending shape
%Junuthula Reddy, "Theory and Analysis of Elastic Plates and Shells", p. 168.
% w1=(1-((r1/a).^2)).^2;
% w2=(1-((r2/a).^2)).^2;

%For static modeshape simply supported:
%Junuthula Reddy, "Theory and Analysis of Elastic Plates and Shells", p. 168.
%nu=nu2; %Poisson ratio
w1=((5+nu)/(1+nu)-2*(3+nu)/(1+nu))*((r1/a).^2)+((r1/a).^4))*((5+nu)/(1+nu))^(-
1);
w2=((5+nu)/(1+nu)-2*(3+nu)/(1+nu))*((r2/a).^2)+((r2/a).^4))*((5+nu)/(1+nu))^(-
1);

%We want to find the displacement due to the DC bias application and
%from that get Celect and N. Start from zero displacement and iterate:
x=0; %Centerpoint static deflection
change=1;
iter=0;

```

```

while abs(change)>1e-3 && iter<100
    term=( (Tox-x*w1)/ep0).^(-3);
    term2=( (Tox-x*w1)/ep0).^(-2);

    int1=trapz(r1,w1.*term2.*r1*2*pi);
    int2=trapz(r2,w2.*r2*2*pi);
    int1b=trapz(r1,w1.*w1.*term.*r1*2*pi);

    %Electrostatic spring:
    Celect=-ep0^2/Vdc^2*int2*int2/int1b;

    %Electoacoustic coupling:
    N=int1/int2*Vdc/ep0;

    oldx=x;
    %Using these values get an estimate of x:
    x=( (N*0.5*Vdc)*(1/Cdia+1/Celect)^(-1))/int2;

    change=(x-oldx)/x;
    iter=iter+1;
end

%Cavity volume compliance:
Ccav=(Vcav-x*int2)/(rho*c^2); %Cavity compliance of the air gap.

omega=f*2*pi;

s=1j*omega;

lambda=c/f;
k=(2*pi)/lambda;

%External environmental loading:
%Simply supported
RA1=0.243*rho*c/(pi*a^2);
CA1=5.523*pi*a^3/(rho*c^2);
RA2=rho*c/(pi*a^2);
MA1=0.643*rho/(pi*a);

%External environmental loading:
%Clamped:
%RA1=0.471*rho*c/(pi*a^2);
%CA1=2.016*pi*a^3/(rho*c^2);
%RA2=0.850*rho*c/(pi*a^2);
%MA1=0.628*rho/(pi*a);

Z1=1./(1/RA1+CA1*1j*omega);
Z2=Z1+RA2;
Zac=1./(1./Z2 + 1./(MA1*1j*omega));

%Squeeze film damping model (with perforations...Scvor's formula):
AScvor=(pi*(Ahole2)^2)/(CC2^2); %Ratio of hole area to unit cell area

```

```

CA=AScvor/2-(AScvor^2)/8-0.25*log(AScvor)-3/8; %Correction factor
Rsqueeze=12*mu*CA/(n2*pi*Tox^3);

%Diaphragm hole model (Martin, Liu... Sheplak, Nishida, AIAA, 44th AIAA
Aerospace Sciences Meeting and Exhibit, Reno, Nevada, Jan. 9-12, 2006):
Rhole=(1/n2)*8*mu*tpoly2/(pi*Ahole2^4);

Z1=Rhole+Rsqueeze;
Z2=Mdia*1j*omega+(1/(Cdia*1j*omega)+1/(Celect*1j*omega))+Rs*N*N;
Z3=(1/(Ccav*1j*omega));

%Transfer function giving volume velocity out (m^3/s) per AC voltage
%applied to the electrodes for an isolated element.
H1=(Zac+Z3+Z1)/((Z1+Z2)*(Zac+Z3)+Z1*Z2)*N;

%Transfer function giving volume velocity out (m^3/s) per pressure
%applied to the surface of the diaphragm (Pa) for an isolated element.
H2=-Z1/((Z1+Z2)*(Zac+Z3)+Z1*Z2);

%Transmit mode:
RHS=zeros(length(Xelem),1);
A=zeros(length(Xelem),length(Xelem));
u=zeros(length(Xelem),1);

for m=1:length(Xelem),
    RHS(m)=-H1*Vac*1/(Rs*Cp*1i*omega+(Rs+Rp)/Rp);
    for n=1:length(Xelem),
        if n==m,
            A(m,n)=1;
        else
            Rmn=sqrt((Xelem(m)-Xelem(n))^2+(Yelem(m)-Yelem(n))^2);

            A(m,n)=0*(s*rho/(2*pi))*(exp(-j*omega*Rmn/c)/Rmn)*H2;
        end
    end
end

u=A\RHS;
power_out=sum((pi*rho/c)*((abs(u)*f).^2));

theta=linspace(-pi/2, pi/2,101);
r=linspace(0.01*rmax,rmax,50);

P=zeros(length(theta),length(r));

for cnt=1:length(theta),
    for cnt2=1:length(r),
        %y and z position of the current test point:
        y=r(cnt2)*sin(theta(cnt));
        z=r(cnt2)*cos(theta(cnt));
        Y(cnt,cnt2)=y;
        Z(cnt,cnt2)=z;
    end
end

```

```

        for cnt3=1:length(Xelem),
            %x-position of this element:
            x0=Xelem(cnt3);
            %y-position of this element:
            y0=Yelem(cnt3);
            R=sqrt(z^2+(xcut-x0)^2+(y-y0)^2);
            P(cnt,cnt2)=P(cnt,cnt2)+u(cnt3)*j*rho*f*exp(-j*omega*R/c)./R;
        end
    end
end

polar(0,50,'-k')
hold on
Pr=P(:,length(r));
%Vout=(0.0420 + 0.0303i)*Pr'
Vout=(-4.023385000402771e-06 - 1.305113569424476e-05i)*Pr')*168;
%polar(theta+pi/2,20*log10(1000000*(10^(-3.29))*abs(Pr')) % (10^(-2.618)) is
a sensitivity from singletransducer.m
polar(theta+pi/2,20*log10(1000000*abs(Vout)))
%polar(theta+pi/2,abs(Vout))

```

B.3 Noise model of the electronics with the nickel-on-glass chip.

```

% Noise circuit model for microphone array electronics

%Constants
k=1.3806503e-23; %Boltzmann Constant (m^2 kg s^-2 K^-1)
T=25+273; %Temperature (K)
omegab=500*2*pi; %Break frequency of REF01 (Hz)

%Circuit Components
Rfb=200e5; %Feedback resistor (Ohms)
Cfb=67e-12; %Feedback capacitor (Farads)
Csensor=65e-12; %Sensor capacitance [sensor + stray] (Farads)
R1=1e3; %Bias resistor (Ohms)
Cfilt=10e-6; %Bias filter capacitor (Farads)
Rstray=15; %Stray resistance between diaphragm and
metal trace (Ohms)

%Noise Parameters of ICs
en=9e-9; %Voltage noise of the opamp (V/Hz^1/2)
in=0.6e-15; %Current noise of the opamp (A/Hz^1/2)
ifb=sqrt((4*k*T)/Rfb); %Johnson noise of feedback resistor
(A/Hz^1/2)
ebiaslow=2e-6; %Low Frequency ADR01 noise (V/Hz^1/2)

%Testing Frequencies

```

```

fstart=100; %Start frequency (Hz)
fstop=1e6; %Stop freq (Hz)
numfreq=1000; %Number of frequencies
f=logspace(log10(fstart),log10(fstop),numfreq);

for cnt=1:numfreq,
    disp([num2str(round(cnt/numfreq*100)) '% complete'])

    omega=f(cnt)*2*pi; %Frequency in Hz
    ebias=abs(ebiaslow*(1/(1+(omega/omegab)*j))); %Voltage noise ADR01
    (V/Hz^(1/2))

    bandpass=1;

    Vbias(cnt)=(Rfb*Csensor*j*omega./(1+(Rfb*Cfb*j*omega)))*...
        *(1./(1+R1*Cfilt*j*omega+1))*ebias*abs(bandpass);
    Ven(cnt)=(1-((Rfb*Csensor*j*omega)/(1+(Rfb*Cfb*j*omega)))*...
        *en*abs(bandpass);
    Vifb(cnt)=(-Rfb./(1+(Rfb*Cfb*j*omega))*ifb*abs(bandpass);
    Vin(cnt)=(-Rfb./(1+(Rfb*Cfb*j*omega))*in*abs(bandpass);

    Vout(cnt)=sqrt((abs(Vbias(cnt)).^2)+(abs(Ven(cnt)).^2)...
        +(abs(Vifb(cnt)).^2)+(abs(Vin(cnt)).^2)); %+(Vinstamp(cnt).^2)
end

figure
loglog(f,abs(Vout),'k',...
    f,abs(Vbias),'r--',...
    f,abs[63],'b:',...
    f,abs(Vifb),'m-.',...
    f,abs[64],'g','LineWidth',2)
legend('Total Noise',...
    'Bias Noise',...
    'OpAmp Voltage Noise',...
    'Feedback Resistor',...
    'OpAmp Current Noise',3)
grid
%axis([10 100000 1e-8 100])
set(gca,'LineWidth',2,'fontsize',12,'fontweight','bold')
xlabel('Frequency (Hz)')
ylabel('Noise Density (V/Hz^(1/2))')
title('Model of Preamp Noise Sources')

z=[f; abs(Vout)];

```

B.4 Snapdown modeling of a single transduce in the nickel-on-glass chip.

```

%Working in m-kg-s units
%For a vented circular diaphragm device (with diaphragm holes) using the CMUT
model as
%described in the JMEMS paper (Doody 2011) including electrostatic
%spring and gap change due to DC bias
%Computing pull-in due to electrostatic force
%This differs from the JMEMS paper only insofar as the external pressure and
cavity compliance
%are not included since this mfile is for the vented case and we are
computing at DC

%Geometric properties of the design:
R=300e-6; %radius of diaphragm (m)
relect=195e-6; %radius of the electrode (m)

%Electrical properties of the design:
Vdc_start=0; %Min Applied bias (Vdc)
Vdc_stop=400; %Max Applied bias (Vdc)
numV=101; %Number of voltage steps
ep0=8.854e-12; %Permittivity of free space (F/m)

%Material properties of diaphragm:
rho=8912; %Density of diaphragm (kg/m^3)
E=200e9; %Elastic modulus of diaphragm (Pa)
nu=0.31; %Poisson ratio of diaphragm (dimensionless)
sigmaR=-265e6; %residual stress (Pa) positive=tensile

%Thicknesses of layers:
h=9e-6; %thickness of diaphragm (m)
g0=5e-6; %thickness of the gap (m)

%END USER PARAMS-----

%Bending stiffness
D=(E/(1-nu^2))*(h^3)/12;

%Diaphragm acoustic compliance, mass and center point to volume velocity
%displacement (From Sheplak and Nishida, JMEMS, Dec 2007):
Cdia=(pi*R^6/(12*16))/D;
%Volume compliance of a thin bending circular clamped plate [m^3/Pa]
%Mdia=(9/(5*pi*R^2))*(rho*h); %Effective mass of a thin bending circular
clamped plate
%ctr=3/(pi*R^2); %Center point to volume displacement ratio of a pure bending
circular clamped plate [m/m^2]

%Add in residual stress effects:
if sigmaR==0
    Cdia=Cdia;
else
    Cdia=1/(1/Cdia+1/((5*pi*R^4)/(9*(2.4048^2))/(sigmaR*h)));
end

```

```

%Compute the electrostatic coupling and electrostatic spring:
r1=linspace(0,relect,1000);
r2=linspace(0,R,1000);

%Using a clamped static bending shape
%Junuthula Reddy, "Theory and Analysis of Elastic Plates and Shells", p. 168.
w1=(1-((r1/a).^2)).^2;
w2=(1-((r2/a).^2)).^2;
%For static modeshape simply supported:
%Junuthula Reddy, "Theory and Analysis of Elastic Plates and Shells", p. 168.
nu=0.31; %Poisson ratio
w1=((5+nu)/(1+nu)-2*(3+nu)/(1+nu))*((r1/R).^2)+((r1/R).^4))*((1+nu)/(5+nu));
w2=((5+nu)/(1+nu)-2*(3+nu)/(1+nu))*((r2/R).^2)+((r2/R).^4))*((1+nu)/(5+nu));

V=linspace(Vdc_start,Vdc_stop,numV);

for cnt=1:numV,
    Vdc=V(cnt);
    %We want to find the displacement due to the DC bias application and
    %from that get Celect and N. Start from zero displacement and iterate:
    x=0; %Centerpoint deflection
    change=1;
    iter=0;
    while abs(change)>1e-3 && iter<100
        term=((g0-x*w1)/ep0).^(-3);
        term2=((g0-x*w1)/ep0).^(-2);

        int1=trapz(r1,w1.*term2.*r1*2*pi);
        int2=trapz(r2,w2.*r2*2*pi);
        int1b=trapz(r1,w1.*w1.*term.*r1*2*pi);

        %Electrostatic spring:
        Celect=-ep0^2/Vdc^2*int2*int2/int1b;

        %Electroacoustic coupling:
        N=int1/int2*Vdc/ep0;

        oldx=x;
        %Using these values get an estimate of x:
        x=((N*0.5*Vdc)*(1/Cdia+1/Celect)^(-1))/int2;

        change=(x-oldx)/x;
        iter=iter+1;
    end
    center_deflect(cnt)=x;

    %Compute element capacitance:
    C(cnt)=trapz(r1,ep0*r1*2*pi./(g0-x*w1));
end
% figure
% plot(V,center_deflect*1e6,'linewidth',2)
% grid

```

```

% set(gca,'Linewidth',2,'fontsize',12,'fontweight','bold')
% ylabel('Centerpoint Deflection (um)')
% title('Static Deflection')
% xlabel('Applied Bias Voltage (V)')

% figure
% plot(V,C*1e12,'linewidth',2)
% grid
% set(gca,'Linewidth',2,'fontsize',12,'fontweight','bold')
% ylabel('Static Capacitance Change (pF)')
% title('Static Deflection')
% xlabel('Applied Bias Voltage (V)')

figure
plot(V,center_deflect*1e6,'linewidth',2)
grid
set(gca,'Linewidth',2,'fontsize',12,'fontweight','bold')
ylabel('Centerpoint Deflection (um)')
title('Static Deflection')
xlabel('Applied Bias Voltage (V)')

figure
plot(V,(C-C(1))*1e12*182,'linewidth',2)
grid
set(gca,'Linewidth',2,'fontsize',12,'fontweight','bold')
ylabel('Static Capacitance Change (pF)')
title('For 182 Elements')
xlabel('Applied Bias Voltage (V)')

```

B.5 Spectrum analysis using velocity data

```

%Spectrogram Test Program
Fs=1e6; %sampling frequency (Hz)
Fmin=179e3; %minimum frequency of interest in spectrogram (Hz)
Fmax=181e3; %maximum frequency of interest in spectrogram (Hz)
Nwin=2^14; %Number of samples in each time window
%Note will use 50% overlap in time windows

%Threshold on laser data:
thresh=-0.35;

%Read in data:
fname='acoustics_withlaser_0p1mps_14cm';

ann='0.3 m/s nominal';

x0=0.14;

```



```

data=load([fname '.txt']);
t=data(:,1);
x=data(:,3);
data2=load([fname '_encoder.txt']);
t2=data2(:,1);
x2=data2(:,2);
v=data2(:,3);
sig=data2(:,4);

%Maximum frequency resolution in the band:
dF=Fs/Nwin;

%Compute spectrogram
%Option 1: Groetzel's method with specified frequency window of interest
%[S,F,T]=spectrogram(y,Nwin,Nwin/2,Fmin:dF:Fmax,Fs);

%Option 2: Full spectrogram
[S,F,T]=spectrogram(x,Nwin,Nwin/2,Nwin,Fs);

PSD=(5.033/dF)*(S.*conj(S))/(Nwin^2); %Note usually there would be a 2 not a
5.033 ... maybe a consequence of the Hamming window normalization?

%Plot
myh=figure;
pcolor(T,F,abs(PSD))
axis([min(t) max(t) Fmin Fmax])
set(gca,'CLim',[0 5e-6])
colorbar
set(gca,'linewidth',2,'fontweight','bold','fontsize',10)
title('Spectrogram (V^2/Hz)')
xlabel('Times (s)')
ylabel('Freq (Hz)')
shading interp
hold on

%disp('Should equal mean square of the signal between Fmin and Fmax:')
%trapz(F,PSD(:,round(size(S,2)/2)))

%Velocity from encoder:

%If using encoder:
%t3=t2;
%v=gradient(x2,mean(diff(t2)));
%v2=movave2(v,500)';

%If using laser:
v2=v;
v2(sig<thresh)=NaN;

figure
plot(t2,v2,'k','linewidth',2)

```

```

axis([min(t) max(t) min(v2(501:(length(v2)-501)))-0.1 max(v2(501:(length(v2)-
501)))+0.1])
set(gca,'linewidth',2,'fontweight','bold','fontsize',10)
title('Laser Velocity')
xlabel('Times (s)')
ylabel('Velocity (m/s)')

text(0.1, (min(v2(501:(length(v2)-501)))-0.1)*0.8,
ann,'fontsize',10,'fontweight','bold','BackgroundColor',[1 1 1])

%saveas(['vel_' num2str(n) '.fig'])
%saveas(['vel_' num2str(n) '.png'])

%The Doppler shift:
%Approximately:
c=343;
f2=180000*(1+2*(v2/c));

%Exactly:
%alpha=atan2(0.0254,x0-x2); %Assuming TX/RX 1 inch from normal to mirror
%From Gjurchinovski, "The Doppler effect from a uniformly moving mirror",
%European Journal of Physics, 26 (4), 2005.
%f2=180000*(1+2.*(v2./c).*cos(alpha)+((v2.^2)./(c^2)))./(1-(v2.^2/c^2));

% figure
% plot(t2,f2,'k','linewidth',2)
% axis([min(t) max(t) Fmin Fmax])
% set(gca,'linewidth',2,'fontweight','bold','fontsize',10)
% title('Expected Frequency')
% xlabel('Times (s)')
% ylabel('Freq (Hz)')
figure(myh)
plot(t2,f2,'w')

text(0.1, 178e3,ann,'fontsize',12,'fontweight','bold','Color',[1 1 1])

%saveas(['spect_' num2str(n) '.fig'])
%saveas(['spect_' num2str(n) '.png'])

```

Appendix C

CAD Drawings

C.1 PolyMUMPs® chip

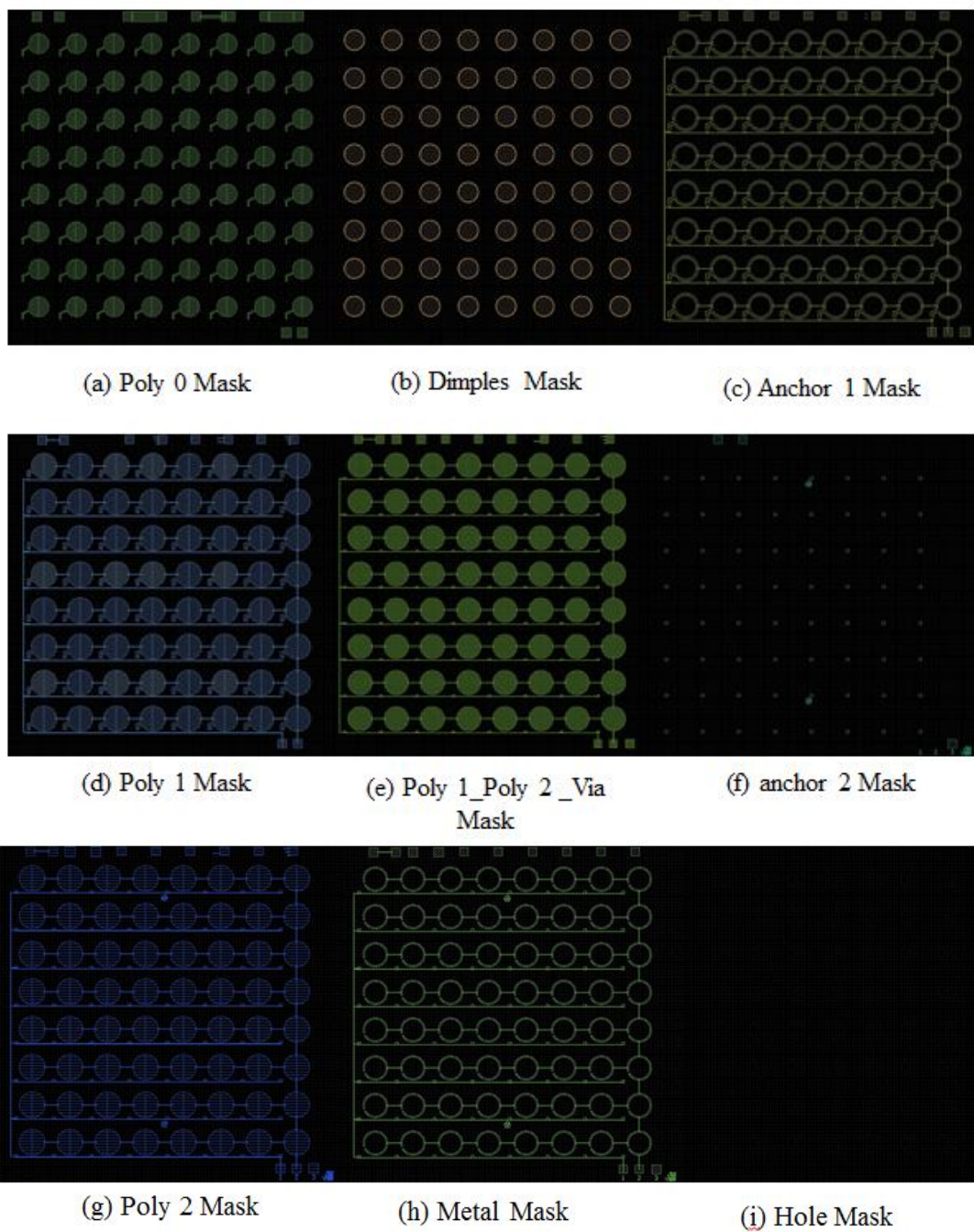


Figure 83: Design masks for the whole array of PolyMUMPs® chip

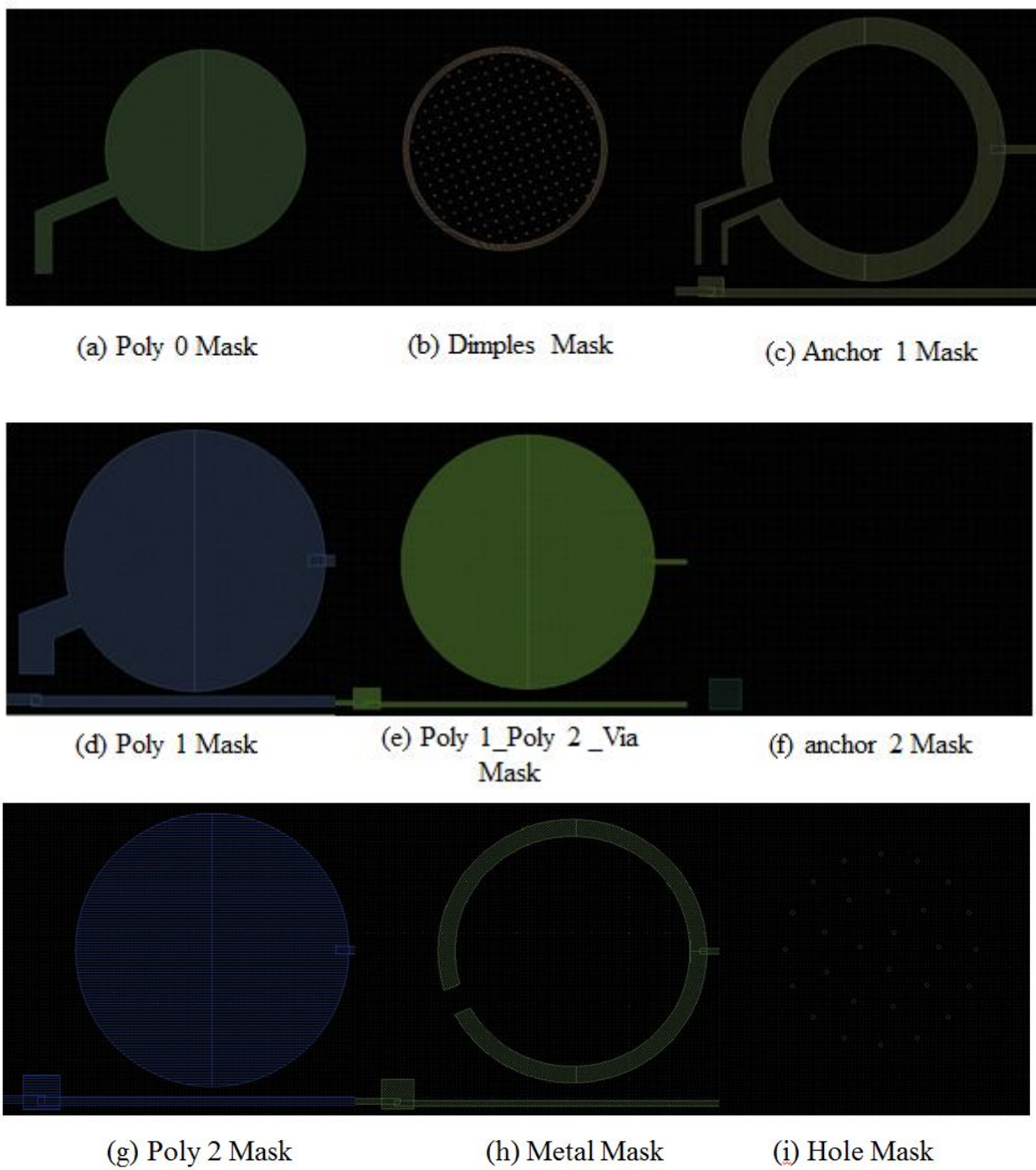


Figure 84: Design masks for a single transducer of PolyMUMPs® chip

C.2 Nickel-on-glass chip

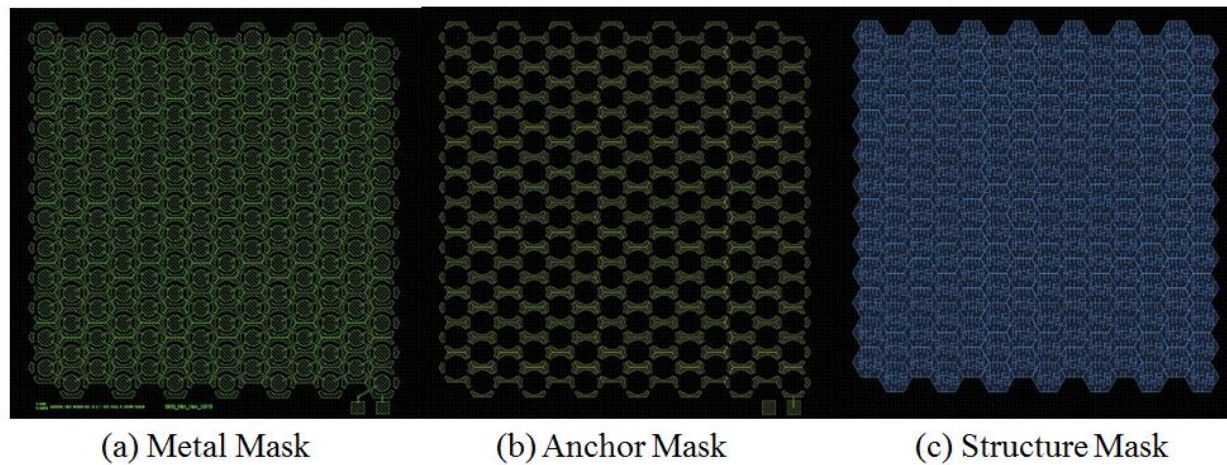


Figure 85: Design masks for the whole array of nickel-on-glass chip.

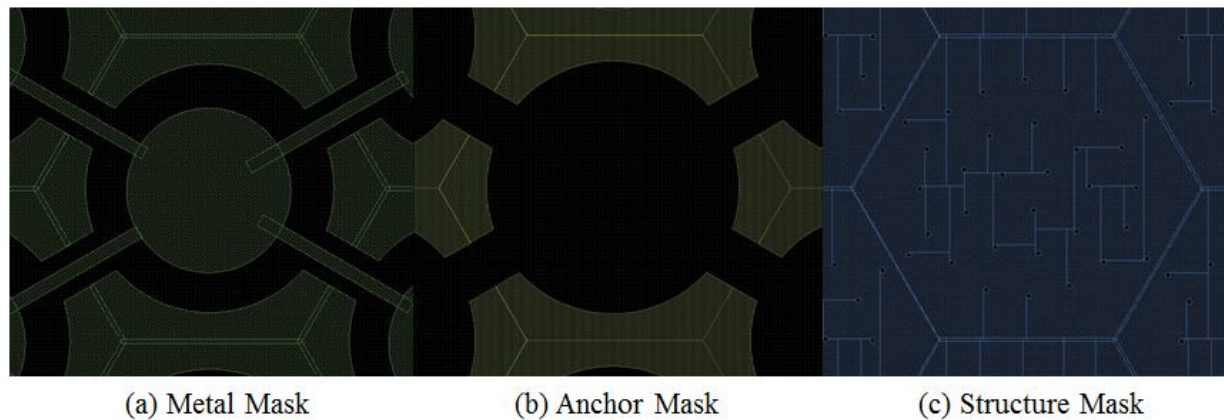


Figure 86: Design masks for a single transducer of nickel-on-glass chip.

C.3 Shadow Mask Design

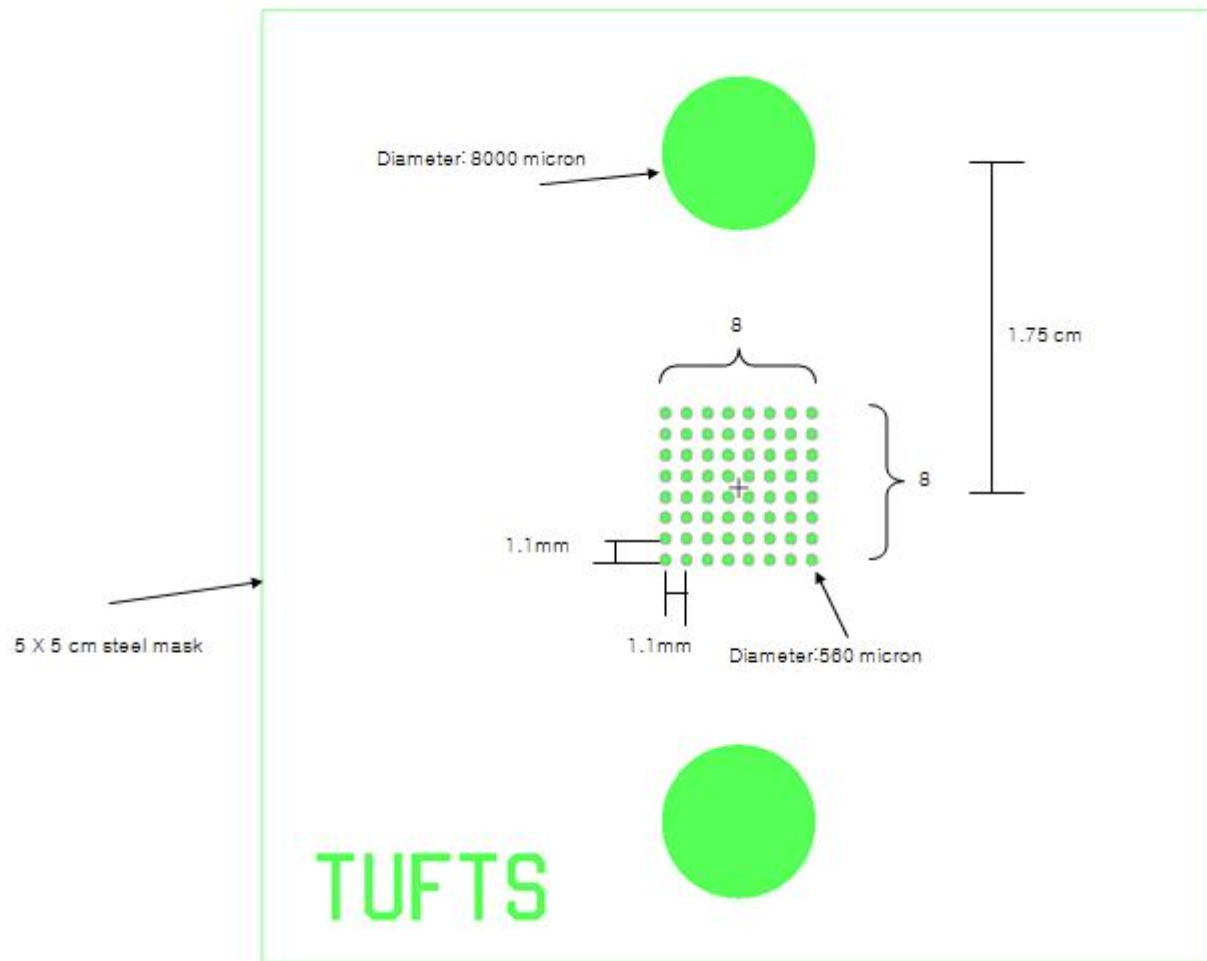


Figure 87: Shadow mask design for PolyMUMPs® chip

Bibliography

- [1] Y. Ando and S. Yuta, "Following a wall by an autonomous mobile robot with a sonar-ring," *Proceedings of 1995 IEEE International Conference on Robotics and Automation, Vols 1-3*, pp. 2599-2606, 1995.
- [2] J. A. Castellanos, J. M. Martinez, J. Neira, and J. D. Tardos, "Simultaneous map building and localization for mobile robots: A multisensor fusion approach," *1998 IEEE International Conference on Robotics and Automation, Vols 1-4*, pp. 1244-1249, 1998.
- [3] G. Hueber, T. Ostermann, T. Bauernfeind, R. Raschhofer, and R. Hagelauer, "New approach of ultrasonic distance measurement technique in robot applications," *2000 5th International Conference on Signal Processing Proceedings, Vols I-Iii*, pp. 2066-2069, 2000.
- [4] C. Y. Lee, H. G. Choi, J. S. Park, K. Y. Park, and S. R. Lee, "Collision avoidance by the fusion of different beam-width ultrasonic sensors," *2007 IEEE Sensors, Vols 1-3*, pp. 985-988, 2007.
- [5] O. Manolov, S. Noikov, P. Bison, and G. Trainito, "Indoor mobile robot control for environment information gleaning," *Proceedings of the IEEE Intelligent Vehicles Symposium 2000*, pp. 602-607, 2000.
- [6] G. C. Anousaki and K. J. Kyriakopoulos, "Simultaneous localization and map building for mobile robot navigation," *Robotics & Automation Magazine, IEEE*, vol. 6, pp. 42-53, 1999.
- [7] J. A. Jimenez, J. Urena, M. Mazo, A. Hernandez, and E. Santiso, "Three-dimensional discrimination between planes, corners and edges using ultrasonic sensors," in *Emerging*

- Technologies and Factory Automation, 2003. Proceedings. ETFA '03. IEEE Conference, 2003*, pp. 692-699 vol.2.
- [8] M. Alwan, M. B. Wagner, G. Wasson, and P. Sheth, "Characterization of Infrared Range-Finder PBS-03JN for 2-D Mapping," in *Robotics and Automation, 2005. ICRA 2005. Proceedings of the 2005 IEEE International Conference on*, 2005, pp. 3936-3941.
 - [9] K. Heon-Hui, H. Yun-Su, and J. Gang-Gyoo, "A study on the environmental map building for a mobile robot using infrared range-finder sensors," in *Intelligent Robots and Systems, 2003. (IROS 2003). Proceedings. 2003 IEEE/RSJ International Conference on*, 2003, pp. 711-716 vol.1.
 - [10] R. Przybyla, S. Shelton, A. Guedes, R. Krigel, D. Horsley, B. Boser, "IN-AIR ULTRASONIC RANGEFINDING AND ANGLE ESTIMATION USING AN ARRAY OF ALN MICROMACHINED TRANSDUCERS," in *Proc. Hilton Head Solid-State Sensors, Actuators and Microsystems Workshop*, pp. 50-53, 3-7 June 2012.
 - [11] R. Przybyla, S. Shelton, A. Guedes, I. Izyumin, M. Kline, D. Horsley, and B. Boser, "In-Air Rangefinding with an AlN Piezoelectric Micromachined Ultrasound Transducer," *Sensors Journal, IEEE*, vol. 11, pp. 2690-2697, 2011.
 - [12] M. I. Haller and B. T. Khuri-Yakub, "1-3 composites for ultrasonic air transducers," in *Ultrasonics Symposium, 1992. Proceedings., IEEE 1992*, 1992, pp. 937-939 vol.2.
 - [13] M. I. Haller and B. T. Khuri-Yakub, "A surface micromachined electrostatic ultrasonic air transducer," in *IEEE Ultrasonics Symposium*, 1994, pp. 1241-1244.
 - [14] M. I. Haller and B. T. Khuri-Yakub, "A surface micromachined electrostatic ultrasonic air transducer," *Ultrasonics, Ferroelectrics and Frequency Control, IEEE Transactions on*, vol. 43, pp. 1-6, 1996.
 - [15] O. Ahrens, A. Buhrdorf, D. Hohlfeld, L. Tebje, and J. Binder, "Fabrication of gap-optimized CMUT," *Ultrasonics, Ferroelectrics and Frequency Control, IEEE Transactions on*, vol. 49, pp. 1321-1329, 2002.

- [16] G. Caliano, R. Carotenuto, A. Caronti, and M. Pappalardo, "cMUT echographic probes: Design and fabrication process," 2002.
- [17] C. B. Doody, C. Xiaoyang, C. A. Rich, D. F. Lemmerhirt, and R. D. White, "Modeling and Characterization of CMOS-Fabricated Capacitive Micromachined Ultrasound Transducers," *Microelectromechanical Systems, Journal of*, vol. 20, pp. 104-118, 2011.
- [18] P. C. Eccardt, K. Niederer, T. Scheiter, and C. Hierold, "Surface micromachined ultrasound transducers in CMOS technology," in *IEEE Ultrasonics Symposium*, 1996.
- [19] X. Zhuang, I. Wygant, D. S. Lin, M. Kupnik, O. Oralkan, and B. Khuri-Yakub, "Wafer-bonded 2-D CMUT arrays incorporating through-wafer trench-isolated interconnects with a supporting frame," *Ultrasonics, Ferroelectrics and Frequency Control, IEEE Transactions on*, vol. 56, pp. 182-192, 2009.
- [20] K. Y. Lee, N. LaBianca, S. A. Rishton, S. Zolgharnain, J. D. Gelorme, J. Shaw, T. H. Chang, x, and P, "Micromachining applications of a high resolution ultrathick photoresist," *Journal of Vacuum Science & Technology B: Microelectronics and Nanometer Structures*, vol. 13, pp. 3012-3016, 1995.
- [21] C.-H. Ho, K.-P. Chin, C.-R. Yang, H.-M. Wu, and S.-L. Chen, "Ultrathick SU-8 mold formation and removal, and its application to the fabrication of LIGA-like micromotors with embedded roots," *Sensors and Actuators A: Physical*, vol. 102, pp. 130-138, 2002.
- [22] V. D. Samper, A. J. Sangster, R. L. Reuben, and U. Wallrabe, "Multistator LIGA-fabricated electrostatic wobble motors with integrated synchronous control," *Microelectromechanical Systems, Journal of*, vol. 7, pp. 214-223, 1998.
- [23] M. Despont, H. Lorenz, N. Fahrni, J. Brugger, P. Renaud, and P. Vettiger, "High-aspect-ratio, ultrathick, negative-tone near-uv photoresist for MEMS applications," in *Micro Electro Mechanical Systems, 1997. MEMS '97, Proceedings, IEEE., Tenth Annual International Workshop on*, 1997, pp. 518-522.

- [24] P. C. Eccardt, K. Niederer, and B. Fischer, "Micromachined transducers for ultrasound applications," in *Ultrasonics Symposium, 1997. Proceedings., 1997 IEEE*, 1997, pp. 1609-1618 vol.2.
- [25] P. C. Eccardt, K. Niederer, T. Scheiter, and C. Hierold, "Surface micromachined ultrasound transducers in CMOS technology," in *Ultrasonics Symposium, 1996. Proceedings., 1996 IEEE*, 1996, pp. 959-962 vol.2.
- [26] A. S. Ergun, C. H. Cheng, U. Demirci, and B. T. Khuri-Yakub, "Fabrication and characterization of 1-dimensional and 2-dimensional Capacitive Micromachined Ultrasonic Transducer (CMUT) arrays for 2-dimensional and volumetric ultrasonic imaging," in *OCEANS '02 MTS/IEEE*, 2002, pp. 2361-2367 vol.4.
- [27] S. T. Hansen, A. Turo, F. L. Degertekin, and B. T. Khuri-Yakub, "Characterization of capacitive micromachined ultrasonic transducers in air using optical measurements," *Ultrasonics Symposium, 2000 IEEE*, vol. 1, 2000.
- [28] I. Ladabaum, J. Xuecheng, H. T. Soh, A. Atalar, and B. t. Khuri-Yakub, "Surface micromachined capacitive ultrasonic transducers," *Ultrasonics, Ferroelectrics and Frequency Control, IEEE Transactions on*, vol. 45, pp. 678-690, 1998.
- [29] D. F. Lemmerhirt, X. Cheng, O. D. Kripfgans, M. Zhang, and J. B. Fowlkes, "A fully-populated 32x32 CMUT-in-CMOS array," in *Ultrasonics Symposium (IUS), 2010 IEEE*, 2010, pp. 559-562.
- [30] C. C. Freudenrich, "How Ultrasound Works," vol. 26, 2006.
- [31] M. Shin, "MRI Evaluation of a Stented Abdominal Aorta of a Rabbit." vol. MS: Univ of Alabama, Birmingham, 2007.
- [32] "Schematic of the therapeutic ultrasound for a deep skin."
- [33] S. E. C. Biber, E. Shenk, and J. Stempeck, "The Polaroid ultrasonic ranging system," in *Engineering Society Convention 67*, 1980.

- [34] "Devantech SRF04 ultrasonic rangefinding system."
- [35] D. Webster, "A pulsed ultrasonic distance measurement system based upon phase digitizing," *Instrumentation and Measurement, IEEE Transactions on*, vol. 43, pp. 578-582, 1994.
- [36] "Wikipedia. Doppler effect."
- [37] W. Kuhl, G.R. Schodder, and F.K. Schroder,, "Condenser transmitters and microphones with solid dielectric for airborne ultrasonics," *Acoustica*, vol. 4(5), pp. 519-532, 1954.
- [38] J. H. Cantrell, J. S. Heyman, W. T. Yost, M. A. Torbett, and M. A. Breazeale, "Broadband electrostatic acoustic transducer for ultrasonic measurements in liquids," *Review of Scientific Instruments*, vol. 50, pp. 31-33, 1979.
- [39] A. Bozkurt, F. L. Degertekin, A. Atalar, and B. T. Khuri-Yakub, "Analytic modeling of loss and cross-coupling in capacitive micromachined ultrasonic transducers," in *Ultrasonics Symposium, 1998. Proceedings., 1998 IEEE*, 1998, pp. 1025-1028 vol.2.
- [40] A. Bozkurt, I. Ladabaum, A. Atalar, and B. T. Khuri-Yakub, "Theory and analysis of electrode size optimization for capacitive microfabricated ultrasonic transducers," *Ultrasonics, Ferroelectrics and Frequency Control, IEEE Transactions on*, vol. 46, pp. 1364-1374, 1999.
- [41] B. Bayram, G. G. Yaralioglu, A. S. Ergun, and B. T. Khuri-Yakub, "Influence of the electrode size and location on the performance of a CMUT [US transducer]," in *Ultrasonics Symposium, 2001 IEEE*, 2001, pp. 949-952 vol.2.
- [42] B. Bayram, G. G. Yaralioglu, M. Kupnik, A. S. Ergun, O. Oralkan, A. Nikoozadeh, and B. T. Khuri-Yakub, "Dynamic analysis of capacitive micromachined ultrasonic transducers," *IEEE Transactions on Ultrasonics, Ferroelectrics and Frequency Control*, vol. 52, pp. 2270-2275, 2005.
- [43] A. Caronti, G. Caliano, A. Iula, and M. Pappalardo, "An accurate model for capacitive micromachined ultrasonic transducers," *Ultrasonics, Ferroelectrics and Frequency Control, IEEE Transactions on*, vol. 49, pp. 159-168, 2002.

- [44] O. Ahrens, A. Buhrdorf, D. Hohlfeld, L. Tebje, and J. Binder, "Fabrication of gap-optimized CMUT," *IEEE Transactions on Ultrasonics, Ferroelectrics and Frequency Control*, vol. 49, pp. 1321-1329, 2002.
- [45] X. Jin, O. Oralkan, F. L. Degertekin, and B. T. Khuri-Yakub, "Characterization of one-dimensional capacitive micromachined ultrasonic immersion transducer arrays," *IEEE Transactions on Ultrasonics, Ferroelectrics, and Frequency Control*, vol. 48, pp. 750-760, 2001.
- [46] R. A. Noble, R. R. Davies, D. O. King, M. M. Day, A. R. D. Jones, J. S. McIntosh, D. A. Hutchins, and P. Saul, "Low-temperature micromachined cMUTs with fully-integrated analogue front-end electronics," in *Ultrasonics Symposium, 2002. Proceedings. 2002 IEEE*, 2002, pp. 1045-1050 vol.2.
- [47] D. M. Mills and L. S. Smith, "Real-time in-vivo imaging with capacitive micromachined ultrasound transducer (cMUT) linear arrays," in *Ultrasonics, 2003 IEEE Symposium on*, 2003, pp. 568-571 Vol.1.
- [48] I. O. Wygant, N. Jamal, H. J. Lee, A. Nikoozadeh, Z. Xuefeng, O. Oralkan, A. S. Ergun, M. Karaman, and B. T. Khuri-Yakub, "2C-3 An Integrated Circuit with Transmit Beamforming and Parallel Receive Channels for 3D Ultrasound Imaging: Testing and Characterization," in *Ultrasonics Symposium, 2007. IEEE*, 2007, pp. 25-28.
- [49] S. Vaithilingam, T. J. Ma, Y. Furukawa, I. O. Wygant, Z. Xuefeng, A. De La Zerda, O. Oralkan, A. Kamaya, S. s. Gambhir, R. B. Jeffrey, and B. T. Khuri-Yakub, "Three-dimensional photoacoustic imaging using a two-dimensional CMUT array," *Ultrasonics, Ferroelectrics and Frequency Control, IEEE Transactions on*, vol. 56, pp. 2411-2419, 2009.
- [50] C. Kuratli and H. Qiuting, "A CMOS ultrasound range finder microsystem," in *Solid-State Circuits Conference, 2000. Digest of Technical Papers. ISSCC. 2000 IEEE International*, 2000, pp. 180-181, 455.

- [51] R. Przybyla, A. Flynn, V. Jain, S. Shelton, A. Guedes, I. Izyumin, D. Horsley, and B. Boser, "A micromechanical ultrasonic distance sensor with >1 meter range," in *Solid-State Sensors, Actuators and Microsystems Conference (TRANSDUCERS), 2011 16th International*, 2011, pp. 2070-2073.
- [52] K. Yamashita, K. Iwahashi, Y. Ohmura, and M. Okuyama, "Ultrasonic Position Measurement using Phased Array Microsensors with Resonant Frequency Variation," in *Solid-State Sensors, Actuators and Microsystems Conference, 2007. TRANSDUCERS 2007. International*, 2007, pp. 1271-1274.
- [53] S. Timoshenko and S. Woinowsky-Krieger, *Theory of plates and shells*: McGraw-Hill College, 1959.
- [54] M. J. Madou, *Fundamentals of microfabrication: the science of miniaturization*: CRC, 2002.
- [55] M. Bauccio and American Society for Metals., *ASM metals reference book*, 3rd ed. Materials Park, Ohio: ASM International, 1993.
- [56] J. F. Shackelford and W. Alexander, *CRC materials science and engineering handbook*, 3rd ed. Boca Raton, Fla.: CRC Press, 2001.
- [57] M. G. El-Hak, *The MEMS handbook*. Boca Raton, FL: CRC Press, 2002.
- [58] A. C. Jim Carter, Busbee Hardy, Ramaswamy Mahadevan, Mark Stonefield, and Steve Wilcenski, "PolyMUMPs design handbook: A MUMPs process," 2005.
- [59] J.K. Luo, S.M. Spearing, N.A. Fleck, W.I. Milne, "Young's modulus of electroplated Ni thin film for MEMS applications," *Materials Letters*, vol. 58, 2004.
- [60] L. L. Beranek and Acoustical Society of America., *Acoustics*, 1986 ed. New York, N.Y.: Published by the American Institute of Physics for the Acoustical Society of America, 1986.
- [61] Z. Skvor, "On acoustical resistance due to viscous losses in the air gap of electrostatic transducers," *Acustica*, vol. 19, pp. 295-297, 1967.
- [62] T. Instrument, "High Voltage FET-Input OPERATIONAL AMPLIFIER OPA445 Manual."

- [63] C. Leavens, R. Willams, P. Burns, and M. Sherar, "The use of phase codes in ultrasound imaging: SNR gain and bandwidth requirements," *Applied Acoustics*, vol. 70, pp. 1340-1351, 2009.
- [64] R. Vinokur, "Vibroacoustic effects in MEMS," *Sound and Vibration*, vol. 37, pp. 22-26, Sep 2003.